Development of a Composite Iron-Matrix Electrode for Nickel-Iron Battery Energy Storage Systems

By

Tendai Tawonezvi

Thesis submitted in fulfilment of the requirements for the degree

Master of Engineering in Chemical Engineering

Faculty of Engineering

At the Cape Peninsula University of Technology

Supervisors

Mr Joe John

Prof Bernard Bladergroen (SAIAMC)

December 2019

CPUT Copyright Information

The thesis may not be published either in part (in scholarly, scientific or technical journals) or as a whole (as a monograph) unless permission has been obtained from the university.

Declaration

I, Tendai Tawonezvi, declare that the contents of this thesis represent my own unaided work and that the thesis has not previously been submitted for academic examination towards any qualification. Furthermore, it represents my own opinions and not necessarily those of either Cape Peninsula University of Technology or South African Institute of Advanced Materials Chemistry.

09/12/2019

Signed **Date**

Abstract

Fe-based alkaline batteries have attracted immense interest as a potential grid stabilizing renewable energy storage technology due to their robustness, long life, non-toxicity, and eco-friendliness. However, a few drawbacks need to be addressed for it to be a commercially viable solution to curtail the intermittency obstacle of renewable energy sources availability. These drawbacks include low coulombic efficiency, low specific energy and cyclic instability. One of the key driving factors for the electrode's restrained performance is the anodic side reactions, i.e. passivation and hydrogen evolution, transpiring during discharging and charging of the Fe-based electrode respectively. In an attempt to enhance the electrochemical performance of the electrode, iron core-copper shell (Fe-Cu) nano-structuring technique and ferrous sulphur (FeS), and graphite (C) additives were utilised. Distinctly electro-conductive nickel mesh (Ni-mesh) current collector was employed coupled with a less sophisticated and low-cost hot-pressing technique.

In this study, FeS and C integrated Fe-Cu core-shell composite electrode was investigated for applications in Fe-based alkaline batteries energy storage. The $FeCu_{0.25}$/FeS/C composite electrode delivered 420 mAh g^{-1} at ≈71% coulombic efficiency, successfully cycling for over 40 cycles. The electrode kinetics and performance were assessed by rate capability, galvanostatic, cyclic voltammetry measurements in 6 M potassium hydroxide (KOH)/1M lithium hydroxide (LiOH) electrolyte at ambient temperature. Ex-situ X-ray diffraction (XRD) characterizations and scanning electrode microscopy (SEM) imaging of both the fresh and cycled electrode surfaces revealed that electrode material particles were still intact marked with negligible particle agglomeration in comparison with pure Fe electrode. Energy filtered transmission electrode microscopy (EFTEM) images confirmed the Fe core copper shell particle arrangement. The $FeCu_{0.25}$/FeS electrode exhibited stable performances marked by high specific capacity coupled with negligible capacity decay and high efficiency. This FeS/C integrated Fe core Cu shell electrode is consequently a conducive negative electrode candidate in alkaline Fe-air and Ni-Fe battery technologies.

Keywords: *Energy Storage, Iron-based Alkaline Battery, Iron Core Copper Shell, Composite Iron-Copper/Sulphide Electrode*

Acknowledgements

I wish to express my gratitude to:

- My loving mother, **Placsedes Ranga**, her never-ending prayers and enormous support from the very beginning has been the reason I have reached this far. Her love and constant wise words of encouragement have impacted this journey positively throughout. I am forever grateful and indebted to her.

- My supervisor, **Prof B.J. Bladergroen**, for believing in me from the very beginning. His constant guidance and encouragement throughout this journey ensured that this project was a success. It was an honour to be a student of such a prominent Professor. He has assisted not only as my supervisor for this project but also granted me adequate opportunities to extend my knowledge related to this project.

- My supervisor, **Mr J. John**, for his exceptional supervision and the insightful contribution throughout the research. He has been my role model for building my personality as a researcher. I am greatly indebted to him.

- **Energy Storage Innovation Lab (ESIL)** for the financial support provided throughout the course of the study. For their love, encouragement, support and all the interaction that made my master's journey exciting.

- **Mrs Denise Davids** for going above and beyond to ensure my administrative documentation were addressed timeously. Her efforts could not go unmentioned.

- **Dr Cecil Felix** for his constructive remarks, suggestions and comments. His contribution to my research work ensured that it reached its full potential.

- My mentor, **Ms Innocentia Erdogan "Zulu Princess"** for her support, care, guidance and insightful remarks and suggestions. Her contributions could not go unmentioned.

- My siblings, **Tracy, Takudzwa and Tatenda**, for their support, love and motivation throughout this journey, it meant a lot.

- My companions, **Tendai Pfavai and Natali Nyabanga**, for their constant wise words of encouragement and relentless support. I am forever grateful for their unwavering support and love.

- My **friends and family** for their love and support.

Dedication

This research work is dedicated to:

My lovely mother, Placsedes Ranga

I wouldn't have made it this far without your buoyant support, unequivocal love and endless sacrifices that you made to ensure I have a better and brighter future.

I love you, Mom.

Table of Contents

Declaration i

Abstract ii

Acknowledgements iii

List of Figures viii

List of Tables xii

List of Symbols-Scientific xiii

List of Symbols-Chemical Species xiv

List of Abbreviations xv

Chapter 1: Introduction 1

1.1 Background 1

1.2 Research Problem Statement 5

1.3 Research Aim and Objectives 6

1.4 Research Questions 7

1.5 Delineation 7

1.6 Significance of Research 7

1.7 Thesis Layout 8

Chapter 2: Literature Review 10

2.1 Overview 10

2.2 Energy Storage Technologies 10

2.2.1 Overview 10

2.2.2 Mechanical Storage 11

2.2.3 Thermal Storage 16

2.2.4 Electrical Storage 17

2.2.5 Chemical Storage 19

2.2.6 Electrochemical Storage 20

2.3 Nickel-Iron Battery Background 29

2.3.1 Discovery of Alkaline Nickel-Iron Battery 29

2.3.2 Basic Operational Principal of a Battery 30

2.3.3 Nickel-Iron Battery Components 32

2.3.4 Nickel-Iron Battery Characteristics 35

2.4 Positive Electrode Material Development 43

2.4.1 Electrochemistry 43
2.4.2 Composite Structure 44
2.4.3 Nanostructure and Morphology 45
2.4.4 Electrode Production Techniques 48
2.5 Electrolyte Optimisation 50
2.6 Negative Electrode Material Development 51
2.6.1 Electrochemistry 51
2.6.2 Composite Structure 54
2.6.3 Nanostructure and Morphology 57
2.6.4 Electrode Production Techniques 63
2.7 Battery/Cell Design 69
2.7.1 Cylindrical Batteries/Cells 69
2.7.2 Prismatic Batteries/Cells 69
2.7.3 Bipolar Batteries/Cells 70
2.8 Deductions from the Literature Review 71
Chapter 3: Experimental Methodology 74
3.1 Overview 74
3.2 Electrode Modification 74
3.2.1 Material and Chemicals 74
3.2.2 Equipment 75
3.2.3 Electrode Production 79
3.2.4 Test Cell Construction 82
3.2.5 Bipolar Ni-Fe Battery Construction 83
3.3 Material Characterization 84
3.3.1 X-Ray Diffraction 84
3.3.1 Scanning Electron Microscopy 85
3.3.1 Transmission Electron Microscopy 86
3.3.2 Porosimetry 87
3.4 Electrochemical Characterization 88
3.4.1 Cycling Voltammetry 88
3.4.2 Galvanostatic Charge/Discharge 92
Chapter 4: Results and Discussion 99
4.1 Overview 99

4.2 $FeCu_x$ Electrode Materials: The Effects of Cu 99
4.2.1 Materials Characterisation 99
4.2.2 Electrochemical Characterisation 103
4.3 $FeCu_x$/FeS Electrode Materials: The Effects of FeS 110
4.3.1 Materials Characterisation 110
4.3.2 Electrochemical Characterisation 112
4.4 $FeCu_x$/FeS/AC Electrode Materials: The Effects of Ammonium Carbonate 118
4.4.1 Electrochemical Characterisation 118
4.5 Bipolar Ni-Fe Prototype 120
4.6 Material and Energy Balance 122
4.6.1 Material Balance 122
4.6.2 Energy Balance 125
4.7 Cost Evaluation 129
4.7.1 Overview 129
4.7.2 Energy Production Cost of a Plant Capacity of 2600 Batteries/Year 129
4.7.3 Cash Flow of a Plant Capacity of 2600 Batteries/Year 134
Chapter 5: Conclusion and Recommendations 136
5.1 Conclusion 136
5.2 The Novelty of the Study 137
5.3 Recommendations 137
References 139
Appendix A-Cycling Data 153
Appendix B-Cash Flow Statement 157

List of Figures

Figure 2-1: Comparison of energy storage technologies based on storage capacity and the duration of storage (data from WEC, 2019) 11

Figure 1-2: Mechanical energy storage systems comparison (based on power rating and energy capacity) (Fournier, 2016) 12

Figure 1-3: A pumped hydroelectric storage plant layout (Luo et al., 2014) 13

Figure 1-4: Schematic diagram of CAES ((Energy Storage Power Corporation (ESPC, 2019) ... 14

Figure 1-5: The main components of a typical flywheel (Luo et al., 2014) 15

Figure 1-6: Electrochemical storage technologies comparison (based on energy capacity and power rating) (Fournier, 2016) 20

Figure 1-7: Schematic diagram of a vanadium redox flow battery system (Luo et al., 2014) ... 22

Figure 1-8: Schematic diagram of a typical electrochemical capacitor using high surface area carbon (Whittingham, 2008) 23

Figure 1-9: Ultra-battery technology schematic diagram (Ultrabattery.org, 2018) 25

Figure 1-10: Comparison of various battery technologies in terms of energy density (data from Muñoz-Torrero et al. (2019) and Tarascon & Armand (2010)) 26

Figure 1-11: Advertisement and cross-section of the first Ni-Fe battery (Used from Edison et al., 1924) 30

Figure 1-12: Illustration of a galvanic cell (Ni-Fe cell) 31

Figure 1-13: Components of a nickel-iron battery cell (Vmack Co, 2018) 32

Figure 1-14: Correlations between capacity and discharge rates at 25°C; end voltage 0.8 V per cell (Reddy & Linden, 2010) 36

Figure 1-15: Time-voltage discharge curves of the nickel-iron battery (Reddy & Linden, 2010) 38

Figure 1-16: The typical voltage characteristics during constant-rate discharge and (Reddy & Linden, 2010) 38

Figure 2-17: Typical charging voltage for a nickel-iron battery at various rates (Reddy & Linden, 2010) 39

Figure 1-18: Cycle life as a function of depth-of-discharge for a typical Ni-Fe cell (Reddy & Linden, 2010) 42

Figure 1-19: The $Ni(OH)_2$ layered crystal structure (Bernard & Lippert, 2009) 46

Figure 1-20: Bode diagram showing transformations among various phases of the nickel hydroxide (Bernard & Lippert, 2009) 47

Figure 1-21: Pocket plate construction (Bernard & Lippert, 2015) 49

Figure 1-22: Voltammogram curve with the redox peaks assigned to corresponding reactions (Lee et al., 2018).....52

Figure 1-23: Illustration of (a) passivating FeOx layer and (b) a possible effect of FeS for the FeOx layer.....56

Figure 1-24: Comparison of structures of discharge products of alkaline iron electrode: (a) $Fe(OH)_2$; (b) δ-FeOOH (Wells, 1970) 59

Figure 1-25: The homogeneous structure of α –Fe.....60

Figure 1-26: Structures of various iron oxide species (Cornell & Schwertmann, 2003) 61

Figure 1-27: Morphological and structural changes in Fe electrode over the deep charge−discharge cycling (Lee *et al*., 2018) 63

Figure 1-28: Pocket plate design (Bernard & Lippet, 2015).....64

Figure 1-29: Simplified construction 3D depiction of a prismatic nickel-iron cell (Linden & Reddy, 2002).....70

Figure 1-30: Schematic structure of a bipolar nickel-iron battery (Fraunhofer UMSICHT, 2019) 71

Figure 3-1: a) Hydraulic press and b) thermal controller box 76

Figure 3-2: The vacuum oven employed during Fe-Cu material synthesis 76

Figure 3-3: Schematic diagram for a press mould 77

Figure 3-4: Different sizes of electrode molds (a)-for cell electrode production (90 x 60 mm), b) for cell electrode production (30 x 60 mm)and c) for CV electrode production (10 x 60 mm)) 77

Figure 3-5: Overhead mixer 78

Figure 3-6: Schematic representation of the experimental methodology adopted for this study 79

Figure 3-7: Schematic illustration of the synthesis process of the $FeCu_x$/FeS/C microparticles 81

Figure 3-8: 3D conception of the cell with two electrodes.....82

Figure 3-9: 3D conception of the cell with three electrodes.....82

Figure 3-10: Process flow diagram of the Ni-Fe test cell production.....83

Figure 3-11: Process flow diagram for the production of 25Wh bipolar Ni-Fe battery 84

Figure 3-12: Schematic diagram of a SEM machine (Suryanarayana, 2016).....86

Figure 3-13: Schematic of TEM imaging methodology (Inkson, 2016) 87

Figure 3-14: Potential-time profiles generated during linear sweep and cyclic voltammetry..89

Figure 3-15: Cyclic voltammogram (Davies et al., 2005).....89

Figure 3-16: Experimental testing configuration for cycling voltammetry (Lee at al., 2017) 90

Figure 3-17: Schematic representation of the on-ground test environment 91

Figure 3-18: Schematic representation of the on-ground test environment (Top view) 91

Figure 3-19: Different types of chronopotentiometry experiments: (a) constant current chronopotentiometry, (b) linearly rising current chronopotentiometry with linearly, (c) current reversal chronopotentiometry and (d) cyclic chronopotentiometry (Pyun et al., 2012).....93

Figure 3-20: Front panel of the battery testing station 94

Figure 3-21: Main window of TC54 96

Figure 3-22: Analog battery display of the channel 96

Figure 4-1: $FeCu_{0.25}$ material EFTEM imaging analysis 100

Figure 4-2: XRD patterns for pure Fe electrode 100

Figure 4-3: XRD patterns for $FeCu_{0.25}$ electrode 101

Figure 4-4: SEM images for a) pure Fe electrode before and after 40 cycles and b) $FeCu_{0.25}$ electrode before and after 40 cycles 103

Figure 4-5: Cycling voltammetry of pure Fe electrode and $FeCu_{0.25}$ electrode electrode in 6M KOH /1M LiOH at 2mV/s.....104

Figure 4-6: Discharge curves of pure Fe electrode and $FeCu_{0.25}$ electrode: the cells were charged at 100mA/g to 1.75 V, and then discharged at 100 mA/g C to 0.8 V 106

Figure 4-7: Polarization curves of pure Fe electrode and $FeCu_{0.25}$ electrode: the cells were charged at 1000 mA/g for 90 min, and then discharged at the rate ranging from 200 mA/g C to 2500 mA/g for 5 s.....106

Figure 4-8: Cycling stability curves of pure Fe and various $FeCu_x$ composite electrodes: the cells were charged at 100mA/g to 1.75 V, and then discharged at 100 mA/g C to 0.8 V 107

Figure 4-9: Coulombic efficiency of Fe-based electrodes containing various amounts of Cu: The cells were charged at 100mA/g to 1.75 V, and then discharged at 100 mA/g C to 0.8 V.....109

Figure 4-10: Discharge capability at different current densities for Fe and $FeCu_{0.25}$ electrode materials: The cells were charged at 100mA/g to 1.75 V, and then discharged at rates from 50 to 600 mA/g to 0.8 V 109

Figure 4-11: XRD patterns for pure Fe electrode 110

Figure 4-12: XRD patterns for $FeCu_{0.25}$/15%FeS electrode.....111

Figure 4-13: Cycling voltammetry of pure Fe electrode, $FeCu_{0.25}$ electrode and $FeCu_{0.25}$/15%FeS electrode in 6M KOH /1M LiOH at 2mV/s. 112

Figure 4-14: Discharge curves of pure Fe electrode, $FeCu_{0.25}$ electrode and $FeCu_{0.25}$/15%FeS electrode: The cells were charged at 100mA/g to 1.75 V, and then discharged at 100 mA/g C to 0.8 V.....114

Figure 4-15: Polarization curves of pure Fe, $FeCu_{0.25}$ and $FeCu_{0.25}$/15%FeS electrodes: the cells were charged at 1000 mA/g for 90 min, and then discharged at the rate ranging from 200 mA/g C to 2500 mA/g for 5 s 115

Figure 4-16: Specific capacity versus % FeS Content in $FeCu_{0.25}$ electrode material: The cells were charged at 100mA/g to 1.75 V, and then discharged at 100 mA/g C to 0.8 V 116

Figure 4-17: 10th cycle specific capacity versus % FeS Content in $FeCu_{0.25}$ electrode material : The cells were charged at 100mA/g to 1.75 V, and then discharged at 100 mA/g C to 0.8 V 117

Figure 4-18: Coulombic efficiency versus % FeS content in $FeCu_{0.25}$ electrode material: The cells were charged at 100mA/g to 1.75 V, and then discharged at 100 mA/g C to 0.8 V 118

Figure 4-19: Cycling stability of $FeCu_{0.25}$/15%FeS composite electrodes with different amounts of AC: the cells were charged at 100mA/g to 1.75 V, and then discharged at 100 mA/g C to 0.8 V.....119

Figure 4-20: Influence of $(NH_4)_2CO_3$ on the electrode porosity 120

Figure 4-21: 3D conception of the test cell with two electrodes 120

Figure 4-22: Laboratory prototype of a 25 Wh bipolar Ni-Fe battery in DIN A6 format 121

Figure 4-23: Material flowsheet adopted during bipolar Ni-Fe battery production.....122

Figure 4-24: Overall mass balance around the bipolar Ni-Fe battery production process 123

Figure 4-25: Energy balance around the mixer, hot-press and oven for the bipolar Ni-Fe battery production.....126

Figure 4-26: Cash flow of a plant with capacity 2600 batteries/year 134

List of Tables

Table 1-1: Crystallography data for various iron oxides and hydroxides (Wells, 1970) 58

Table 1-2: Comparative analysis table on the development of the negative electrode over the years.....67

Table 3-1: Materials and chemicals utilised during the course of this research 74

Table 3-2: Small equipment compilation.....78

Table 3-3: Operating parameters of the hot-pressing process.....81

Table 4-1: Mixer specifications 126

Table 4-2: Raw materials cost estimation of a single bipolar Ni-Fe battery 130

Table 4-3: Cost of major equipment utilised in the production of Ni-Fe batteries (2600 batteries/year) 131

Table 4-4: Estimation cost of the plant utilities per year (plant with capacity 2600 batteries/year) 132

Table 4-5: Operating labour cost for 1300 hours per year using a plant capacity for Ni-Fe batteries at a rate of 2600 batteries/year 132

Table 4-6: Manufacturing cost estimation for production of Ni-Fe batteries (2600 batteries/year) 132

Table A-1: Discharge capacity data: the cells were charged at 100mA/g to 1.6 v, and then discharged at 100 mA/g C to 0.8 V 153

Table A-2: Charge capacity at the 10th cycle: the cells were charged at 100mA/g to 1.75 V 155

Table A-3: Electrode composition 156

Table B-1: Cash flow statement (in Rands) 157

List of Symbols-Scientific

Scientific Symbols

Symbol	Description	Units
θ	Angle	o
V_b	Bulk Volume	ml
Q	Capacity	Ah/Wh
X	Conversion	
I	Current	A
E	Energy	J
η	Energy Efficiency	%
V_g	Grain Volume	ml
M	Mass	kg
Mr	Molar Mass	kg/kmol
N	Moles	ml
V_p	Pore volume	ml
Φ	Porosity	%
P	Power	W
R	Resistance	Ω
ν	Stoichiometry Coefficient	
V	Voltage	V
λ	Wavelength	Hz

List of Symbols-Chemical Species

Chemical Specie Symbols

Specie	Description
$(NH_4)_2CO_3$	Ammonium Carbonate
$B(OH)_3$	Boric Acid
Cd	Cadmium
$CuSO_4$	Copper Sulphate
H_2	Hydrogen
Fe	Iron
$Fe(OH)_2$	Iron (II) Hydroxide
Fe_2O_3	Iron (II) Oxide
$FeSO_4$	Iron (II) Sulphate
Fe_2O_3	Iron (III) Oxide
FeS	Iron Sulphide
$LiOH$	Lithium Hydroxide
Hg/HgO	Mercury/Mercury Oxide
Ni	Nickel
$NiOOH$	Nickel Oxy-Hydroxide
Pt	Platinum
KOH	Potassium Hydroxide
$NaBH_4$	Sodium Borohydride
Na_2SO_4	Sodium Sulphate
S	Sulphur
Ti	Titanium
H_2O	Water

List of Abbreviations

AC	Ammonium Carbonate
BMS	Battery Management System
BMS	Battery Management System
BTS	Battery Testing Station
CB	Carbon Black
CA	Coathelyne
CSIRO	Commonwealth Scientific and Industrial Research Organisation
CAES	Compressed Air Energy Storage
CV	Cyclic Voltammetry
DOE	Department of Energy (United States)
DC-AC	Direct Current-Alternating Current
EDLC	Electric Double Layer Capacitors
EPRI	Electric Power Research Institute
ES	Energy Storage
FES	Flywheel Energy Storage
FES	Flywheel Energy Storage
GF/CNT	Graphene Foam-Carbon Nano-Tubes
C	Graphite
IREA	International Renewable Energy Agency (USA)
LDPE	Low-Density PolyEthylene
LDPE	Low-Density Polyethylene
NPV	Net Present Value
OCV	Open Circuit Voltage
OCV	Open-Circuit Voltage

PCM	Phase Change Material
PCM	Phase Change Materials
PTFE	PolyTetraFluoroEthylene
PVDF	PolyVinyliDene Fluoride
PtG	Power to Gas
PEM	Proton Exchange Membrane
PSH	Pumped-Storage Hydroelectricity
RFB	Redox Flow Batteries
RFB	Redox Flow Battery
SEM	Scanning Electron Microscopy
SRAM	Static Random Access Memory
SMES	Superconducting Magnetic Energy Storage
TES	Thermal Energy Storage
TEM	Transmission Electron Microscopy
XRD	X-Ray Diffraction

Chapter 1: Introduction

1.1 Background

The world currently relies eminently on coal, oil, and natural gas for its energy, energy sources which are non-renewable and will eventually dwindle, becoming too expensive and too environmentally destructive to retrieve (REN21, 2018; REN21, 2019). Hasty industrialisation and technology advancements over the years have propelled businesses and homes into becoming extensively dependent on electrical energy (REN21, 2019). To cater for the demand, power stations have traditionally relied on the combustion of high carbon intensity fuels like oil and coal (IREA, 2017).

Fossil fuels are carbon-intense and burning them has accrued negative environmental consequences. Due to the continuous depletion of these natural resources coupled with the rising demand of clean energy owing to rampant economic development, exponential population growth, environmental damage and rapid industrialisation, the development of alternative clean and sustainable energy sources is imperative (IEC, 2010; IREA, 2018). The development of clean and renewable energy sources is thus indispensable to control the manifestation of environmental problems and sustain economic development and industrialisation. Implementation of low to zero carbon content energy sources will avert if not eliminate the catastrophic carbon-induced climate change.

Renewable energy, which has attracted immense interest recently, refers to the energy that is harnessed from a natural resource that replenishes to supress resource exhaustion instigated by consumption (Stead & Stead, 2009). Renewable resources constitute a mega fraction of the earth's natural environment and the chief components of its ecosphere. These energy resources are in abundance and environmentally friendly, in account of this they exhibit the potential to decrease emissions of harmful greenhouse gases while posing a practical approach to lessen the reliance on fossil fuels, it is thus conspicuous why most countries are taking vital measures to implement effective energy policies that will accelerate the utilisation of such key technologies. These new technologies have attracted tectonic interest as evident from the global deployment of a new fiscal policy “Green New Deal” (REN21, 2015). The “Green New Deal” delineate any incentive program that aims to tackle both economical (financial) and environmental issues such as climate change (Barbier, 2010).

Based on REN21's 2017 report, renewables contributed 19.5 % and 23.8 % to the global energy consumption in 2014 and 2015 respectively. Worldwide investments in renewable technologies amounted to more than R 4.72 trillion in 2015, with countries like China, Japan and the United States leading the investment charts (REN21, 2015). The REN21 (2015) report found that the carbon intensity dropped at the global average of 2.8 %, a transition that is largely driven by a rapid fall in coal consumption and accelerated implementation of renewable energy technology. These divulged statistics indicate an amplified interest of transitioning from fossil fuels to renewable energy in an attempt to circumvent the fossil fuel accrued hurdles.

In the discussions presented by World Energy Council (2016) and REN21 (2015), for first world countries, it is commonly found that governments are actively pursuing renewable energy targets through different target policies and incentives with some more ambitious than others. International Renewable Energy Agency (IREA) (2018) extrapolated that renewable energy could contribute 70% of the energy mix by 2050 if countries adopt irreproachable policies without delay. The sources of renewable energy at the hub of the world's interest include wind, sunlight, rain, tides, waves, and geothermal heat.

In recent years, renewable energy sources, such as the wind and solar energy sources have emerged as suitable energy sources to boost energy security and supply, and alleviate ecological and environmental matters (REN21, 2016). Solar and wind energy are clean renewable sources of energy that has received much attention due to the inexpensive nature of energy conversion technology, high energy capacity and non-carbon composition. Moreover, among all the types of renewable power production resources, solar and wind renewable energy is considered as one of the fastest-growing resources (IREA, 2018). It is hardly surprising that in 2014, global solar and wind energy production reached 185 GW and 380 GW respectively, which correlates to an increase of approximately 30% relative to the previous decade (REN21, 2015).

However, energy generation from renewable sources is not always feasible when energy demand peaks (stochastic wind profiles, seasonal resource availability such as water, sunlight, etc.). Storing the energy during low energy demand and then discharging it during the peak energy demand can overcome these sporadic obstacles. The integration of renewable energy and energy storage thus offers the transcendent key to the drift between intermittent energy generation trend and incessant energy demand. Several energy storage techniques are widely

utilized, these include mechanical, thermal, electrical, chemical and electrochemical techniques (REN21, 2019).

Electrochemical energy storage offers an ideal practical solution that would help balance the electrical energy grid by mitigating the sporadic renewable energy generation trend to match energy demand. This solution is viable chiefly due to its high round-trip efficiency, long cycle life, low cost, and scalability (REN21, 2019; IREA, 2017). Several battery technologies have been developed in the last century, but in large-scale applications, only a few have been demonstrated. Among the various developed battery technologies, aqueous batteries have the potential to aid in balancing the future electrical energy grid at a lower cost than any of their non-aqueous counterparts (such as Li-ion, Na-ion, etc.) owing to its globally abundant raw materials and low-cost electrolyte solution (water-based). Ultimately, non-aqueous batteries require integration of costly safety systems to minimise the risk of fire and explosions; such expensive systems are inessential for aqueous batteries (Abdalla *et al*. 2016; Posada & Hall, 2016).

Lead-acid (Pb-acid) batteries are the oldest, most commercially deployed aqueous energy technology however its energy density (~ 35-40 Wh kg^{-1}), the toxicity of raw materials, and short cycle life curb its potential as an ideal renewable energy storage technology candidate (Posada & Hall, 2016; Posada *et al*. 2017). In contrast, invented and commercialised in the early 20th century, nickel-iron (Ni-Fe) cells could potentially deliver 2–3 times the specific energy of Pb-acid batteries, proffer increased ruggedness and elongated cycle life at deep discharge state (>10000 cycles at 80% Depth of Discharge) (Zhao *et al*., 2015). In addition, with Ni-Fe batteries exceeding 15000 cycles of charge and discharge, they vastly surpass most of their competing battery technology counterparts, this is Pb-acid (300-400 cycles), Ni-MH (500–800) and Ni-Cd (1300-1600 cycles) (Posada & Hall, 2016; Wang *et al*. 2012).

Renewed interest in the Fe-based batteries (such as Ni-Fe and Fe-Air) has been chiefly propelled by the incentive to develop cost-effective, highly efficient energy storage technologies. Ni-Fe cells are secondary batteries that are well known for robustness, non-toxicity, and eco-friendliness (Kao *et al*. 2011; Reddy & Linden, 2010). The relative abundance of chemicals and raw materials required to construct these batteries indicate that this battery technology could proffer a cost-effective solution to store energy for electricity grid system applications. However, the successful commercial deployment of these batteries has been

obstructed by their poor coulombic efficiency (40–60%), low discharge rate capability and low specific energy (~50 Wh kg^{-1}) (Huang *et al*., 2018). These drawbacks are a direct consequence of the parasitic evolution of hydrogen during charging of the Fe-based electrode and the passivation of Fe-based electrode attributed to an insulating layer of $Fe(OH)_2$ generated during the discharge process (Huang *et al*. 2018; Manohar *et al*. 2012). This refractory evolution of hydrogen is attributed to the standard reduction potential of the hydrogen reaction (Equation 1-1) being more positive than that of the Fe reduction reaction (Equation 1-2).

$$2H_2O+2e^- \rightarrow H_2+2OH^- \quad \left(E^o = -0.83 \text{ V vs Hg/HgO}\right) \qquad [1\text{-}1]$$

$$Fe+2OH^- \rightarrow Fe(OH)_2+2e^- \quad \left(E^o = -0.88 \text{ V vs Hg/HgO}\right) \qquad [1\text{-}2]$$

The Fe-based electrode exhibits a preeminent influence (compared to other components) on the overall electrochemical performance of the Ni-Fe battery, therefore, by altering the electrode's material composition, design, nanostructure and/or production techniques, the battery's overall performance will subsequently improve (Manohar *et al*., 2012). To overcome the hydrogen evolution reaction and increase specific capacity, various sulphide and carbon additives have been used as electrode or electrolyte additives. Among them, few are considered as effective: Bi_2S_3, Bi_2O_3, FeS, K_2S, Na_2S, organo-sulphurs (Hang *et al*. 2016; Manohar *et al*. 2012; Manohar *et al*. 2016; Zhao *et al*. 2010).

Most of the compounds form different Fe sulphide phases, while elemental bismuth metal is produced during charging consequently increasing the hydrogen evolution overvoltage (Manohar *et al*. 2013: Manohar *et al*., 2016). Nanoparticles have proved beneficial for enhancing the utilization of the active materials (Caldas *et al*. 1998; Raja *et al*. 2014). Caldas *et al*. (1998) optimised porosity of the Fe-based electrode by employing $(NH_4)_2CO_3$ (AC) as a porosity inducing agent. Huang *et al*. (2018) have recently synthesized Fe core-copper shell composite electrode with a high concentration of Cu yielding a high rate discharge capacity of 150 mAh g^{-1} at a current density of 2000 mA g^{-1}.

In this study, a combination of both Cu and FeS additives coupled with porosity inducing agent $(NH_4)_2CO_3$ and electroconductive graphite (C) was employed. FeS/C integrated Fe-Cu core-shell structured composite material was synthesized as anode material to be utilised in Fe-based alkaline batteries. The rationale behind this is that Cu shell should circumvent Fe particle

agglomeration during cycling, $(NH_4)_2CO_3$ should optimise the porosity of the electrode, graphite should formulate a good conductive network subsequently improving the reversibility of the active material and FeS should impede the parasitic hydrogen evolution reaction and the passivation process. The in-house produced electrode was integrated into a bipolar design, a low-cost design saves up to 80% of conventional battery materials such as electrolyte, insulating sheets and cables.

1.2 Research Problem Statement

The implementation of renewable energy systems as a definite aspect of energy supply emanates with some hurdles, which are mainly induced by intermittency trend of renewable energy sources. In this case, storing energy for later use becomes the major impediment. Establishment of a stable, robust, low-cost, environmentally friendly and efficient energy storage system is then necessary and imperative. A rechargeable battery gives the prospect to store electrical energy into chemical energy using different valence states of a material, which can be used reversibly through redox-reactions. Rechargeable batteries in conjunction with a renewable energy generation technology is a major step towards a green future with a low to non-carbon footprint, among other accrued benefits.

The awakened search for a low-cost scalable stationary energy storage system during the last decade has led to a revived attention for the Ni-Fe battery. The Ni-Fe battery is well-known for its robustness, long life. Nevertheless, the Ni-Fe battery suffers from severe drawbacks, mostly induced by the negative electrode, that impels low efficiency and low specific energy. In addition, expensive production methods are currently employed for electrode production. These drawbacks preclude the existing Ni-Fe battery from being a viable energy storage alternative. Developing a FeS doped Fe-Cu composite electrode (with optimised porosity using ammonium carbonate (AC)) for the alkaline Ni-Fe battery storage system for renewable energy might accelerate the curtailing of these drawbacks.

In this project, a composite FeS doped Fe-Cu electrode with optimised porosity using AC was embodied in a bipolar Ni-Fe battery design in order to enhance the performance of the alkaline Ni-Fe battery storage system for renewable energy.

1.3 Research Aim and Objectives

The chief aim of this research is to develop, optimise and test the overall performance of a Ni-Fe battery system for use in energy storage applications.

The developed Ni-Fe battery prototype should match or exceed the below specifications:

- Increased battery's coulombic efficiency (target >70%)
- Increase in discharge capability (90% capacity retainment at >1C discharge rate)
- Reduction in battery cost (target production cost R7500 kWh^{-1})
- Attain cycling stability (negligible capacity decay after 40 cycles)

In order to achieve the aim, the following objectives must be executed;

- Integrate copper into iron-based electrodes in the form of Fe core Cu shell to increase the specific capacity of the electrode
- Integrate iron sulphide into iron-based electrodes to increase coulombic efficiency
- Optimize electrode porosity using a pore-forming agent ($(NH_4)_2CO_3$) to increase capacity
- Produce composite electrodes by using low-cost hot-pressing technique and employing a low-cost current collector/substrate Ni mesh to reduce the battery cost
- Characterize electrode through x-ray diffraction analysis, scanning electrode microscopy, cyclic voltammetry and galvanostatic charge and discharge test
- Determine the optimum composition that yields the best performance and construct a bipolar Ni-Fe battery prototype using the in-house synthesized composite Fe-Matrix electrode as a negative electrode.
- Perform a cost evaluation of the bipolar Ni-Fe battery constructed using an optimized composite electrode

1.4 Research Questions

The above-listed objectives would be met by answering the following research questions:

- What is the effect of Cu composition on the electrochemical performance of the electrode?
- What is the effect of FeS composition on the electrochemical performance of the electrode?
- What is the effect of $(NH_4)_2CO_3$ composition on the electrochemical performance of the electrode?
- What is the optimum composition of Fe-Cu/FeS/$(NH_4)_2CO_3$ composite electrode that yields the best electrochemical performance?
- Based on the optimum composite electrode, does the bipolar Ni-Fe battery have sufficient potential to be an interesting competitor for Renewable Energy Storage Systems (RESS)?

1.5 Delineation

It is thus evident from the previous sections that any improvement to the efficiency of any battery component will have inordinate functional benefits for the overall battery unit. Key areas that can be refined are the composition and production techniques of the electrodes. This work will only focus on the development and characterisation of a Fe-based composite electrode in an attempt to improve the overall electrochemical performance of a Ni-Fe battery. The development or optimisation of other battery components, i.e. Ni-based cathode, electrolyte and separator, will not be covered in this research work.

1.6 Significance of Research

Across the globe, there is an urgent need to find commercially viable and environmentally safe technologies to store the vast amount of renewable energy since these sources are intermittently available.

Development of a high performing Fe-electrode will subsequently improve the overall electrochemical performance of the Ni-Fe battery (for energy storage), a viable solution that will reduce levelized cost of energy storage and lessen, in an attempt to eliminate, the dependence on fossil fuels. Storage technologies particularly Ni-Fe batteries are vital fragments of the energy transition puzzle not only because they can stockpile electrical energy

for later use, but because they aid in stabilizing the flow of electrical energy, especially as intermittent energy sources such as solar and wind enter the energy network.

The ultimate goal will be to provide a foundation to set up Ni-Fe battery-based energy storage which will not only reduce levelized cost of energy storage or supply valuable energy in times of need but will also contribute to the establishment of a new industry for job creation and decarbonised environment. This research will provide a giant step forward in optimizing current energy storage technology that may be able to completely solve the renewable energy storage dilemma and expansively lower the world's fossil fuel demand.

1.7 Thesis Layout

The outline structure of this thesis is briefly described under each of the chapter headings that follow:

Chapter 1 - Introduction:

This introductory chapter provides an insight into the research with background information on energy storage and an overview of the potential functional systems improvements that are currently under investigation. A background into the hub of the research in electrochemical energy storage is provided. The application, justification and value of this research for use of Ni-Fe batteries in grid-scale energy storage applications are discussed. The overall aim and research objectives are also identified and explained in this chapter.

Chapter 2 - Literature Review:

The literature review shelters all the theoretical background required to gain an in-depth understanding of the fundamental engineering principles that are applied in this research. The review is extensive and covers most of the theory, directly and indirectly, related to the research to ensure that the review is sufficiently holistic for a range of engineers, regardless of discipline, to comprehend the theories and implicated practical work presented here. Fe electrode development is the primary focus of the literature review; however, other sections related to Ni-Fe battery construction have also been featured briefly to allow for connections to the blanket concept to be made easily. Fundamental understandings of Ni-Fe battery design, deliberations and theories have also been included as foundation of the research topic. The testing standards required to validate this study have also been covered and presented.

Chapter 3 – Experimental Methods:

This chapter describes the materials and experimental methods used in this research. All the techniques, programs and equipment are well detailed and presented to clearly elucidate how the literature information was employed in practice to solve the research problem.

Chapter 4 – Results and Discussion:

While the contents of this chapter are self-explanatory, the primary purpose of this chapter is to examine and discuss the collated data. The examinations and discussions also cover the comparisons of the various numerical and empirical data-sets. Based on these discussions and examinations, concluding statements are connected to the primary objectives of the research set out in Chapter 1.

Chapter 5 – Conclusion and Recommendations:

Following Chapter 4, Chapter 5 summates all the key points in relation to the research problem and objectives. Key points are meticulously investigated and evaluated. Furthermore, the consequences and implications of the study are discussed. Following the conclusion, a summary of various changes and alterations that could be implemented should a research budget or any other limitations allow for it is presented. Over and above research limitations, various recommendations for concerns discovered during the research, are deliberated in terms of future research work in this area of energy storage systems development. This proposes new insights and creative approaches for framing and contextualizing the research problem based on the results garnered in this study.

Chapter 2: Literature Review

2.1 Overview

The literature review section shelters all the relevant theoretical background for energy storage with specific interest focused on Ni-Fe batteries. It is worth noting that the Ni-Fe battery technology development was abandoned (few developments reported) between 1995-2010, therefore, literature content reviewed will cover the period before 1995 and recent developments from 2010. After a comprehensive review on the various energy storage technologies available (Section 2.2), a short general background follows on the Ni-Fe battery technology (Section 2.3) which includes a brief history, the basic operational principle, the characteristics of commercial Ni-Fe batteries, a short description of the battery components, this literature review provides some essential details on the Ni-based electrode (Section 2.4) and electrolyte optimisation (Section 2.5) followed by an extensive review of research literature related to the development of the Fe-based electrode (Section 2.6). The different battery designs utilised in Ni-Fe battery constructions are briefly discussed in Section 2.7. The findings with regards to the development of the latter electrode are summarized in Section 2.8.

2.2 Energy Storage Technologies

2.2.1 Overview

Energy storage technologies offer a wide array of technological solutions to balance energy resource availability and energy demand (Ibrahim *et al.*, 2008). In order to construct a more robust energy infrastructure and forge low-cost utility schemes for consumers, diverse approaches and solutions are currently being deployed around the world which includes mechanical, thermal, chemical, electrical and electrochemical energy storage techniques, all of which will be discussed in below sections. Figure 2-1 graphically contrasts various energy storage technologies based on power rating, response time and energy capacity. The following sections embody a comprehensive analysis of the different energy storage technologies available.

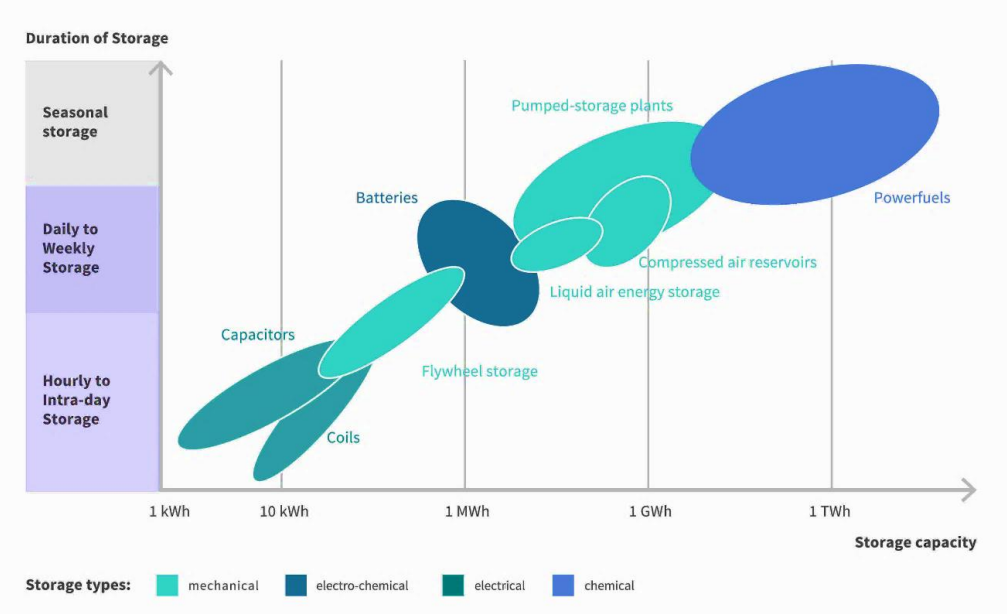

Figure 2-1: Comparison of energy storage technologies based on storage capacity and the duration of storage (data from WEC, 2019)

2.2.2 Mechanical Storage

2.2.2.1 Overview

Energy can be stored in liquids (usually water) pumped to higher elevations (as potential energy) using pumped-storage systems or in solid matter (gravity batteries) conveyed to higher sites (Amiryar & Pullen, 2017). Other commercially established mechanical energy storage technologies comprise of compressed air energy storage systems (CAES) and flywheel systems that transform electrical energy into kinetic energy and then convert back to electrical energy when electrical energy demand peaks (Ibrahim *et al.*, 2008). The accompanying Figure 2-2 graphically compare various mechanical energy storage technologies based on power rating, response time and energy capacity. From the graph, large CAES and pumped-hydro systems exhibit higher energy capacity and power rating compared to flywheel and small CAES systems. However, the response time of the latter technologies edges out the former, making both technologies feasible and favourable depending on the requisites of the application. The detailed insights and illustrations on each technology are discussed in sections below.

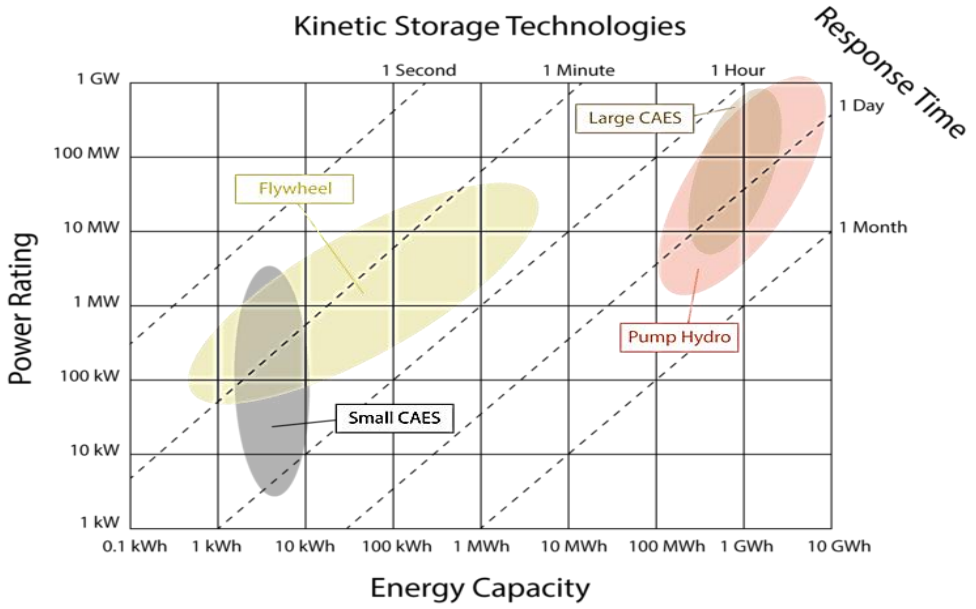

Figure 2-2: Mechanical energy storage systems comparison (based on power rating and energy capacity) (Fournier, 2016)

2.2.2.2 Hydroelectricity

Hydroelectric dams equipped with water impoundment systems (reservoirs) are able to generate energy during periods of peak energy demand. During periods of low energy demand, water is retained in the reservoir and when energy demand peaks, water is discharged back to the dam. The net effect modelled is analogous to a pumped storage system but without the pumping energy loss.

Although the hydroelectric dam does not store energy directly from other energy generation systems, it operates analogously by reducing output from other energy sources during periods of surplus electrical energy supply. In this mode, hydroelectric dams are one of the most efficient (> 85%) energy storage systems, because only their generation timing differs (Huggins, 2010). Huggins (2010) also noted that hydroelectric turbines start-up on the order of a few seconds (60-90 seconds). This low-cost, scalable energy storage system is environmentally friendly (slashed carbon dioxide emissions) and ideal for industrial applications (Bermann, 2007). However, the construction and application of this system result in the ecosystem and environmental damage, loss of land, water loss (through mass evaporation), toxic methane gas emissions and is marked with associated failure risks and geographic and meteorological limitations (Eyer & Corey, 2010). Burdened by the above-mentioned drawbacks, the system is not entirely conducive for diversified applications.

2.2.2.3 Pumped-Storage

Worldwide, pumped-storage hydroelectricity (PSH) is the largest energy capacity form of active grid energy storage technology available, and, as of April 2012, the Electric Power Research Institute (EPRI) (2012) reported that PSH accounted for more than 98% of bulk energy storage capacity worldwide, representing approximately 128 GW, with storage capacity at 750 TWh.

Surplus energy is utilised to pump liquid (usually water) from the source to an elevated reservoir during periods of low electrical energy demand. When energy demand peaks, water is pumped through a generator back into a lower reservoir (waterway or water body), generating electrical energy. Assemblies of reversible turbine generators function as both a pump and a turbine (conventionally a Francis turbine design) (Eyer & Corey, 2010). Eyer & Corey (2010) indicated that virtually all hydroelectric systems utilise the height difference between the two water reservoirs (bodies). Pumped-storage plants rely solely on transporting the water between reservoirs, while the "pump-back" approach is a combination of conventional and pumped-storage hydroelectric power plants that utilise natural streamflow.

In practice, PSH reported round trip energy efficiency ranges between 75% and 85%, with some surging up to 88% (Huggins, 2010; Levine, 2003). PSH energy storage technology is flexible, relatively low costly, suitable for industrial applications and prompt reduced carbon dioxide emissions (Bermann, 2007). However, this system results in the ecosystem and environmental damage, loss of land, water loss (through mass evaporation) and toxic methane gas emissions (IEC, 2010). In light of the above-mentioned impediments, the applicability of this energy storage system is limited to specific locations. The accompanying Figure 2-3 depicts a typical pumped hydroelectric plant layout.

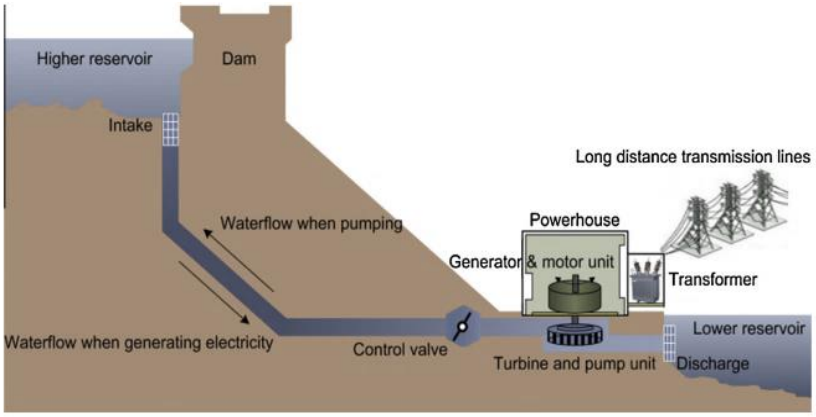

Figure 2-3: A pumped hydroelectric storage plant layout (Luo *et al.*, 2014)

2.2.2.4 Compressed Air

Compressed air energy storage system (CAES) employs excess energy to compress air for subsequent electrical energy generation (Luo *et al.*, 2015). A typical CAES system schematic layout is depicted in Figure 2-4.

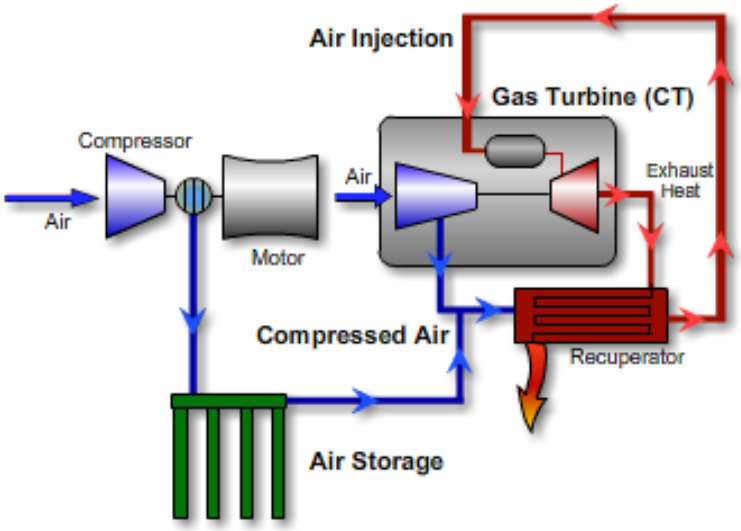

Figure 2-4: Schematic diagram of CAES ((Energy Storage Power Corporation (ESPC, 2019)

Air is compressed by surplus electrical energy and stored in either in underground vaults or a network of vessels or pipes above ground. In a modified gas turbine system, the compressed air is blended with natural gas when needed (Nakhamkin, 2007). (Nakhamkin, 2007). Aquifers, abandoned mines, or caverns are the conventional underground gas storage options (IEC, 2010). IEC (2010) highlighted that if the heat energy generated during gas compression is dissipated through cooling and not retained, it is essential for the compressed air to be reheated prior to gas expansion. This process, termed diabatic CAES, yields low energy round-trip efficiencies (typically less than 55%). Huggins (2010) elucidated that diabatic technology has technically matured; the CAES plants are highly reliable and are able to start up without extraneous power.

The use of natural gas is primarily problematic when it is utilised for heat energy addition. Considering natural gas prices are poised to dramatically increase, the financial economics of CAES systems, peripheral at present, could catastrophically fail (Zohuri, 2017). Once again, utilising the example of wind energy, a wind energy farm employing a CAES system could be viewed as a combustion turbine with a 3-fold energy yield increase in comparison with a conventional gas turbine generator (Gardner & Haynes, 2003; Zohuri, 2017). While this is an

incredible upgrade, it takes some of the 'renewable energy' lustre off the wind energy farm. The main advantage of the CAES system is its enormous energy capacity. However, the system is marred by low round-trip efficiency and meteorological and geographic limitations (Huggins, 2010: Gardner & Haynes, 2003). Due to the abovementioned shortfalls, the applicability of this technique to solve future storage demand is limited.

2.2.2.5 Flywheel Energy Storage

Flywheel energy storage systems (FES) operates by accelerating a flywheel (rotor) to an extremely high speed, storing energy as rotational energy (Amiryar & Pullen, 2017). Amiryar and Pullen (2017) cited that when the rotational energy is depleted, the flywheel's rotational speed decreases as a direct consequence of low rotational energy; adding energy results in a corresponding increase in the rotational speed of the flywheel. A typical flywheel schematic design is depicted in Figure 2-5.

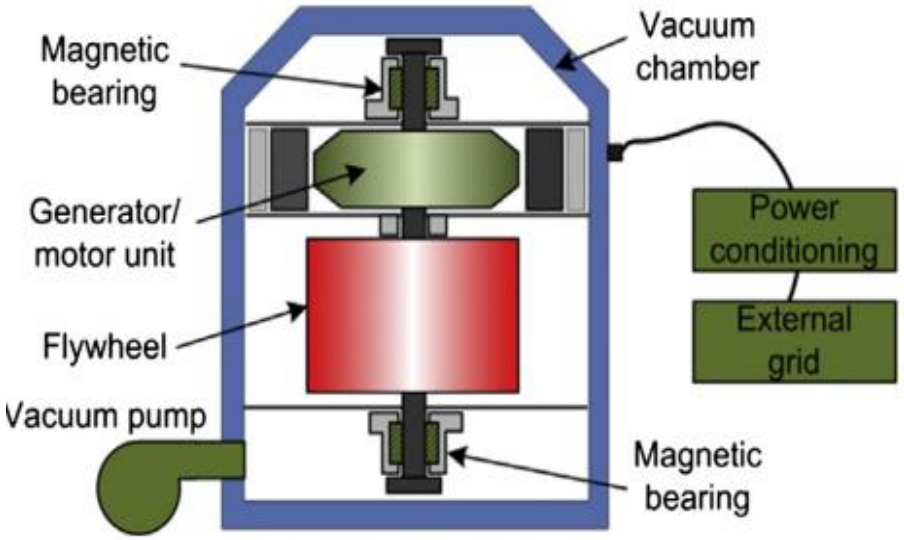

Figure 2-5: The main components of a typical flywheel (Luo *et al.*, 2014)

Most FES systems utilise electrical energy to accelerate and decelerate the flywheel (rotor), but systems that directly operate solely on mechanical energy are under development (EPRI-DOE, 2003). EPRI- DOE (2003) stipulated that FES systems are fitted with rotors constituting high strength carbon-fibre composite materials, suspended by magnetic bearings and rotating at speeds ranging from 25,000 to over 60,000 rpm in a vacuum compartment. Such flywheels can reach maximum rotational speed (full state of charge") in a matter of few minutes. The rotor is driven by a combination electric motor and generator. FES systems can operate for decades with little or no maintenance; full-cycle lifetimes quoted for flywheel systems range from in

excess of 10^5, up to 10^8, cycles), yield high specific energy and power density (Amiryar & Pullen, 2017).

Temperature fluctuations do not impact the flywheel system operation as do the electrochemical rechargeable batteries, nor do they suffer from the memory effect according to Amiryar & Pullen (2017). They are also less potentially harmful; to the environment, constituting largely inert or benign materials. Another additional advantage of flywheel systems is that it is possible to quantify the exact amount of energy stored by simply measuring the rotational speed (Ibrahim *et al*., 2007). Nevertheless, the implementation of flywheel systems is currently impeded by the unstable round-trip efficiency (drops to 40% after one day of continuous operation) and the possibility of the massive wheel being explosively shattered due to overload (Ibrahim *et al*., 2007; IES, 2010).

2.2.3 Thermal Storage

Thermal energy storage system (TES) is the short-term storage or discharge of heat energy by utilising materials with high specific heat capacity. Thermal energy storage systems can be classified into divergent technologies: sensible heat energy storage, latent heat energy storage, and thermo-chemical sorption (adsorption, absorption) energy storage (Schossig, 2008). Hasnain (1998) highlighted that sensible heat energy storage is one of the most prevalent technologies, with the hot water thermal storage unit as the most common sensible heat energy storage system. The energy storage medium can be either a liquid such as water or thermo-oil, or a solid mass such as sand or concrete. Heat energy is stored solely through a shift of storage material temperature. The energy storage capacity of the material is determined by the combination of specific heat capacity and mass of energy storage material.

Latent heat energy storage is attained by employing phase change materials (PCMs) as energy storage mediums (Shah, 2018). Zalba *et al.* (2003) highlighted that this TES technology is feasible due to the elevated heat of fusion of PCMs for example: approximately 335 MJ of heat energy can be absorbed to completely melt of one metric ton (1000 kg) of an ice slab. A variety of inorganic PCMs (salt hydrates) and organic (paraffins) are also eligible as storage mediums for thermal energy storage systems. This energy storage mechanism is also titled “hidden” heat because of the absence of temperature shifts during energy transitions.

Shah (2016) reported that sorption storage systems constitute a complex design and operate as thermo-chemical heat pumps in vacuum atmospheres. The heat energy from a high-temperature source is absorbed by an adsorbent (e.g. zeolite or silica gel). The operating fluid (e.g. water vapour) is desorbed from this adsorbent and condensed in a condenser at low temperatures. The latent heat of condensation is extracted from the process. The operating fluid and dry adsorbent can be separately stored as long as desired. The operating fluid absorbs low-temperature heat in the evaporator during the discharging process. Subsequently, the operating fluid vapour adsorbs on the adsorbent and heat of adsorption is emitted at high temperatures (Jähnig *et al*., 2006).

Nowadays, energy security is often attained with the implementation of additional equipment. The application of (PCMs) could either eliminate or reduce the utilisation of additional equipment. Thermal inertia and thermal protection, as reported by Zalba *et al*. (2003), is the area where the PCMs have attained higher market penetration. The round-trip efficiency of TES techniques is expected to be over 55% (Jähnig *et al*., 2006). Organic materials utilised for heat energy storage constitute no corrosives, exhibit low undercooling and chemical and thermal stability however they effuse a lower phase change enthalpy, low thermal conductivity and high flammability (Shah, 2016; Zalba *et al*., 2003). In-organic material for heat storage exhibit greater phase-change enthalpy, however, they possess undercooling characteristics, corrosive, phase separation, phase segregation and thermal instability (IES, 2010). In general, this energy storage system is relatively costly (R3750-R10500/kWh) and low efficient (50%-65%), factors which inhibit its wide implementation in the near future (Bai *et al*., 2015; International Renewable Energy Agency, 2017; Shah, 2018).

2.2.4 Electrical Storage

2.2.4.1 Capacitor

A capacitor (formerly known as a 'condenser') is a passive electrical component that can electrostatically store energy in an electrical field (Simon & Gogotsi, 2009). Kötz & Carlen (2000) stressed that the configuration of capacitors varies widely, but all constitute at least two electro-conductive plates separated by a dielectric sheet (i.e., insulator). A capacitor can retain electrical energy when disconnected from its charging device, so it can temporarily act as a battery or any other energy storage technology. Capacitors are widely applied in electronic

devices to sustain constant power supply whereas charge fluctuates in electrochemical batteries, this avoids information loss in volatile memory (Whittingham, 2008; Simon & Gogotsi, 2009). Conventional capacitors provide less than 350 J kg^{-1}, while a conventional alkaline battery effuses an energy density of approximately 550 kJ kg^{-1} (Whittingham, 2008).

Capacitors have extremely fast response time, high round trip energy efficiency (>70%) and essentially unlimited cycle lifetimes, however, the energy capacity is limited, typically can store less than 0.1 Wh kg^{-1} (Whittingham, 2008; Kötz & Carlen, 2000; Simon & Gogotsi, 2009). In light of this, they consequently pose a limited role in applications where significant energy amounts need to be stored.

Researchers are currently investigating the quantum effects of nanoscale dielectric capacitors in digital quantum batteries (Whittingham, 2008; Bak *et al*., 2016).

2.2.4.2 Superconducting Magnetic Energy Storage

Superconducting magnetic energy storage systems (SMES) store energy in a magnetic field generated by the unidirectional flow of an electric charge in a coil composed of a superconducting wire that has been cryocooled to a temperature level below its critical superconducting temperature (Amaro *et al*., 2012). Buckles and Hassenzahl (2000) stated that a standard SMES system is comprised of a superconducting wire, power conditioning system and refrigeration unit. The electric charge does not decay when the superconducting coil is fully charged, implying that the magnetic energy can be stored indefinitely. The capacity (maximum storable energy) is determined by the dimensions and geometry of the superconducting coil, these parameters also determine the inductance of the coil.

The magnetic energy stored is discharged by the superconducting coil via a direct current (DC) to alternating current (AC) conversion process enacted by a power inverter. The integrated power rectifier/inverter accounts for approximately 1–3% energy loss during either the charge or discharge process (Buckles & Hassenzahl, 2000). SMES systems lose the least amount of energy during the discharge process compared to other energy storage technologies thereby actuating a round-trip efficiency greater than 95% (Fuchs & Leuthold, 2012). However, SMES systems have a very high-power density (10 -10^4 W/Kg) but discharge that energy in a very short period of time, prompting a device with low energy density (1-2 Wh/Kg) (Amaro *et al*., 2012).

Attributable to the refrigeration energy requirements and the cost of superconducting wire, SMES systems' applications are limited to only high-power short-duration applications such as power quality control for production plants (e.g. microchip fabrication plants) (Buckles & Hassenzahl, 2000). Buckles and Hassenzahl (2000) and Amaro *et al*. (2012) also noted that the technology is also applicable in power grid stabilizing.

2.2.5 Chemical Storage

2.2.5.1 Power to Gas

Götz *et al*. (2016) defined power to gas (PtG) as a process which converts electrical power into gaseous energy-rich fuels such as carbon-neutral methane through methanation process or hydrogen through electrolysis. Three water electrolysis technologies are widely utilised to produce hydrogen namely alkaline electrolysis, proton exchange membrane (PEM) electrolysis and solid oxide electrolysis. Alkaline electrolysis is at present the most economical process; in the future, however, PEM electrolysis could be a better fit for the gas process chain. Solid oxide electrolysis could also be a suitable option in the future, especially if there are vast heat sources available (Götz *et al*., 2016; Komarnicki *et al*., 2017).

Three PtG technologies are widely utilised. The first PtG method involves the injection of hydrogen into the natural gas grid to utilise it in transportation or industry. The second PtG method comprises the reaction of hydrogen with carbon dioxide to yield methane via a methanation reaction (such as the Sabatier reaction), or biological methanation, which results in an extra energy conversion loss of approximately 10% (Jentsch *et al*., 2014; Götz *et al*., 2016). The methane may then be fed into the natural gas grid. The third PtG method utilises the output mixed gas (primarily methane and carbon dioxide) of a wood gasification unit (wood gas generator) or a biogas plant after biogas is mixed with the hydrogen (from the electrolyser) in the biogas upgrader to upgrade the quality of the biogas. However, the technology has negative environmental implications (CO_2 emissions), low round-trip efficient (<55%) and entails high economic costs (capital cost: R17500-R21500/kWh) (Götz *et al*., 2016; Jentsch *et al*., 2014; Komarnicki *et al*., 2017). These factors serve as a hindrance to its wide implementation in the near future.

2.2.5.2 Biochemicals

The organic compound norbornadiene, upon exposure to light, is converted to quadricyclane, storing solar energy as chemical bond energy (Durgun & Grossman, 2013; Lennartson *et al*., 2015). Lennartson *et al*. (2015) iterated that an operational molecular solar thermal energy storage system was developed in Sweden. However, the system is deemed unpractical due to its blistering degradation, instability, low energy density, low round-trip efficiency and high associated costs.

2.2.6 Electrochemical Storage

One alternative energy storage technology that is receiving amplified attention is electrochemical energy storage. With respect to the context of multidimensional challenges, electrochemical energy storage (EES) technology is a feasible solution. Figure 2-6 graphically compares various electrochemical energy storage technologies based on power rating, response time and energy capacity. However, redox flow and hybrid batteries are not included in the graphical comparison but will be discussed in the latter sections. Detailed insight and illustrative review of the technologies is discussed in the following sections.

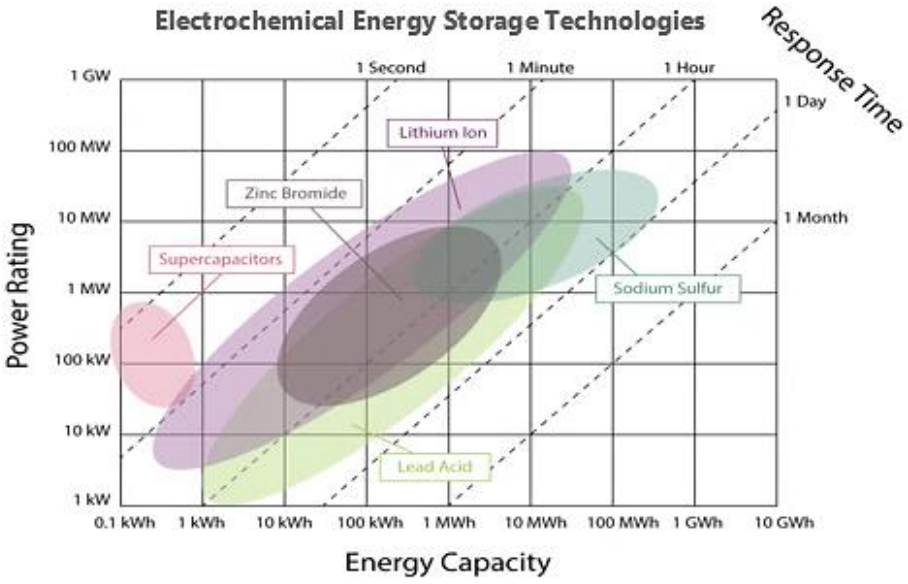

Figure 2-6: Electrochemical storage technologies comparison (based on energy capacity and power rating) (Fournier, 2016)

2.2.6.1 Redox Flow Battery

A redox flow battery (RFB) operates by streaming an electrolyte solution over an ion-selective membrane where ions are exchanged to discharge or charge the battery (EPRI-DOE, 2003). For practical applications, cell voltage, which and varies from 1.1 to 2.5, is electrochemically determined by the Nernst equation. The energy storage capacity of a typical RFB is regulated by the volume of the tanks housing the electrolyte solution (EPRI-DOE, 2003; Weber *et al*., 2011). EPRI-DOE (2003) highlighted that the term "redox" refers to the electrochemical reduction and oxidation reactions which transpire in the RFB in order to store energy in the liquid electrolyte solution. During the discharge process, an electron is released to the external circuit via an oxidation reaction from a high chemical potential state on the negative electrode or anode lateral of the battery. The electron travels through an external circuit simultaneously discharging energy through executing work. Ultimately, the electron is accepted on the positive electrode or cathode lateral of the battery via a reduction reaction at a lower chemical potential state. The trajectory of the current and the chemical reactions is reversed during charging.

RFB is technically akin to both an electrochemical battery and fuel cell. Commercial RFB technologies are designed for long half-cycle energy storage such as power source for backup grids. Today numerous redox couple options have been analysed and tested in redox flow systems, such as a Fe-Cr RFB system, a Fe-air RFB system, Fe-Ti RFB systems and a polyS-Br RFB system (15 MW and 120 MWh Regenesys installation in the UK, but never commissioned) (Hagihara *et al*., 2016). The vanadium redox flow battery (VRFB) is the most technologically advanced system; it has been piloted since the 1990s by corporations such as Cellstrom (Australia) and Prudent Energy (Canada) (IEC, 2010). Alotto *et al*. (2014) emphasized that diffusion of metal ions through the ion-selective membrane cannot be totally halted (as is the case for most RFB), only resulting in loss of energy. In other RFB systems, which utilise different metals ions for anolyte and catholyte, the crossover fosters irreversible electrolyte degradation and capacity loss. Figure 2-7 depicts a schematic design of a typical vanadium redox flow battery system.

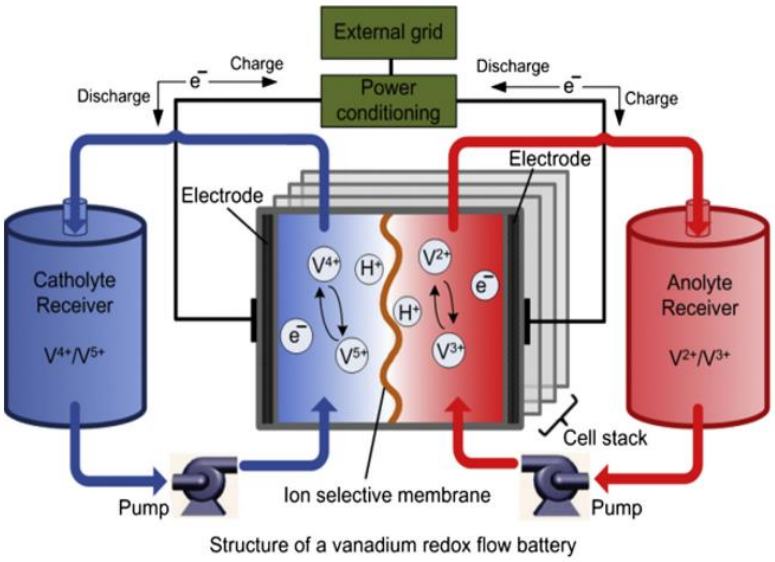

Figure 2-7: Schematic diagram of a vanadium redox flow battery system (Luo *et al.*, 2014)

Redox flow batteries especially vanadium redox flow batteries, and hybrid flow batteries to a lesser extent, offer a versatile layout advantage (attributed to detachment of the power and energy elements), long cycle life (due to absence of solid-to-solid phase transitions), fast response times, no need for "charge equalisation" of the battery (overcharging of a battery to ensure that all cells contain equal charge) and no hazardous gas emissions (Pan & Wang, 2015). Various battery technologies also offer a simplified determination of state-of-charge (via voltage dependence on charge), require sparse maintenance and tolerant to electrochemical abuse (overcharge/over-discharge). In comparison with rechargeable solid-state batteries (such as Li-ion), RFBs, and aqueous RFBs, in particular, can operate effectively at higher power and current densities (IEC, 2010). These technical merits propel redox flow batteries to qualify as a pertinent option for large-scale energy storage.

On the negative side, the energy densities differ considerably but are, in general, lower in comparison with portable solid-state batteries, such as the Li-Poly and Li-ion (Alotto *et al.*, 2014; Pan & Wang, 2015). Flow batteries also operate at considerably lower efficiency (60-80%) relative to non-reversible fuel cells or electrolysers utilizing identical electrolytic chemistries (Wang *et al.*, 2012). Wang *et al.* (2012) also indicated that the development and economics involved in upscaling from pilot scale to industry scale is an ongoing process. The high cost of stack components such as end plates, bipolar plates, seals and membranes are the most prominent impediments faced by this technology.

2.2.6.2 Electrochemical Supercapacitor

Supercapacitors, also known as electric double-layer capacitors (EDLC) or ultracapacitors, are universal terms for a group of electrochemical capacitors that do not possess conventional solid dielectrics (Conway, 2009). Capacitance is regulated by two storage concepts, double-layer and pseudocapacitance. Figure 2-8 below exhibits a schematic diagram of a typical electrochemical capacitor using high surface carbon.

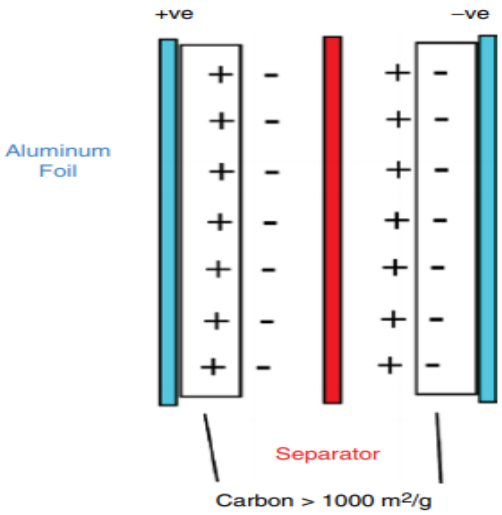

Figure 2-8: Schematic diagram of a typical electrochemical capacitor using high surface area carbon (Whittingham, 2008)

Whittingham (2008) depicted a schematic diagram of an electrochemical capacitor utilising activated carbon (high surface area carbon) that highlight the important components and basic chemistry employed by a typical system. The existing gap between rechargeable batteries and conventional capacitors is abridged by supercapacitors. Electrochemical capacitors have the highest specific energy or energy density (can store the highest energy per unit of mass or volume) among capacitors. They are able to deliver up to 11,500 farads/1.2 volts, up to 11,500 times more than that of electrolytic capacitors, but deliver or accept less than half as much energy per unit time (low power density) (Whittingham, 2008; Conway, 2009). The technology has high round energy efficiency (>90%) (Conway, 2009).

Although supercapacitors offer energy densities of approximately 10% of standard conventional batteries, their power density is typically 20 to 200 times greater (Whittingham, 2008). This results in much shortened charge and discharge periods. Additionally, electrochemical supercapacitors tolerate many more electrochemical cycles than standard conventional batteries (Whittingham, 2008).

Supercapacitors are applicable in a wide range of applications (Conway, 2009), including:

- Low constant current supply for memory backup in static random-access memory (SRAM)
- Power for automobiles (cars, buses, trains, cranes and elevators), short-term energy storage and burst-mode power supply

Supercapacitors exhibit extremely fast responses (very short response timeframes) and essentially unlimited electrochemical cycle lifetimes but store very little energy per unit of mass, typically less than 0.1Wh/kg and (Whittingham, 2008; Winter & Brodd, 2004). They thus have limited applications where significant amounts of energy need to be stored.

2.2.6.3 Hybrid-Battery

The hybrid battery, also known as ultra-battery, is a hybrid carbon-based ultracapacitor (or supercapacitor) and Pb-acid cell technology invented by the Commonwealth of Scientific and Industrial Research Organisation (CSIRO) (Nakajima *et al*., 2013). Nakajima *et al*. (2013) elucidated that both the Pb-acid cell and carbon-based ultracapacitor are packaged into the same casing consequently they are both submerged in the sulphuric acid electrolyte solution. The ultra-battery can be developed with similar electrochemical, electrical and physical characteristics to traditional Pb-acid batteries thereby providing a cost-effective alternative for Pb-acid in multiple Pb-acid based applications.

Physically, a hybrid-battery constitutes a twin negative electrode (one carbon electrode, one Pb electrode) and a single positive electrode submerged in a shared sulphuric acid electrolyte solution. Together, the carbon and Pb components, constitute the twin negative electrode of the hybrid-battery module, but precisely, the carbon electrode is for the capacitor and Pb electrode is for the Pb-acid cell. The singular positive electrode (PbO) is typical of all Pb-acid batteries and widely utilised in Pb-acid-ultracapacitor ultra-batteries. A schematic design of a hybrid battery is depicted in Figure 2-9.

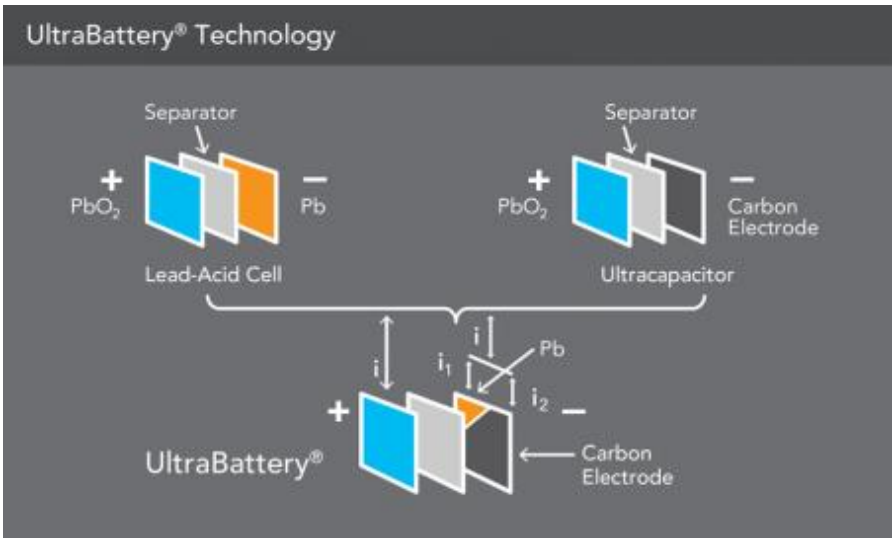

Figure 2-9: Ultra-battery technology schematic diagram (Ultrabattery.org, 2018)

The ultra-battery endures operations at high charge and discharge rates coupled with the ability to deliver manifold cycles (> 15000 cycles), outperforming traditional Pb-acid batteries by more than an order of magnitude (Lam & Louey, 2006). Lam & Louey (2006) stipulated that thousands of cycles have been attained in hybrid-electric automobile tests. The ultra-battery is also highly tolerant of the sulphation effects in comparison with conventional Pb-acid batteries. This means the hybrid-battery can operate continuously in a partial state of charge whereas conventional Pb-acid batteries are generally held at a full charge between discharge states. It is generally energy inefficient to fully charge a Pb-acid battery so by decreasing time spent in the top region of charge phase, the hybrid-battery attain high energy efficiencies, typically between 90 and 98% (Copping & Wood, 2011).

The hybrid-battery is applicable across a wide range of applications. The constant electrochemical cycling and fast charging and discharging properties are essential for applications such as grid control and levelling and electric automobiles as they can damage electrochemical batteries but are tolerated by the ultra-capacitive qualities of ultra-battery technology (Lam & Louey, 2006). The hybrid-battery technology has been installed in Australia and the US on the megawatt scale, primarily for performing frequency regulation and undertaking grid stabilizing applications (Nakajima *et al.*, 2013). This is a promising technology; however, it has been reported that its materials and construction are costly (Copping & Wood, 2011; Lam & Louey, 2006; Nakajima *et al.*, 2013).

2.2.6.4 Traditional Rechargeable Batteries

A rechargeable battery constitutes one or more electrochemically reversible cells. It is termed secondary cell due to electrochemically reversible nature of its electrochemical reactions. Rechargeable batteries are designed in various sizes and shapes from pin-type to megawatt grid systems.

Total operating costs and environmental impact of rechargeable batteries are lower than those of non-rechargeable (disposable) batteries. Various rechargeable battery technologies are available in the same form as their non-rechargeable counterparts. Rechargeable batteries entail a higher capital cost, but they can be recharged at a very low cost and reused multiple times bringing about a low levelized cost of energy. In addition, Rechargeable batteries yield high round-trip efficiency (65%), another attractive factor (Eyer & Corey,2010). Figure 2-10 graphically compare various traditional rechargeable battery technologies based on energy density, cycle life, power, battery cost and safety level. A detailed and comprehensive comparison is outlined in the following section.

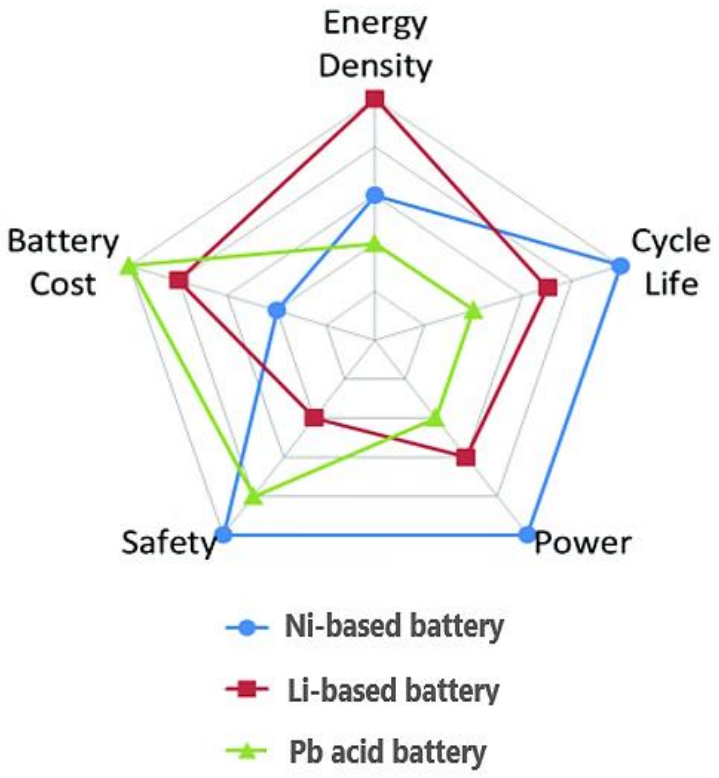

Figure 2-10: Comparison of various battery technologies in terms of energy density (data from Muñoz-Torrero *et al.* (2019) and Tarascon & Armand (2010))

Common rechargeable battery chemistries include:

- **Lead–Acid Battery (Pb-Acid)**: Pb-acid batteries hold the largest market share in the electrical energy storage products market. A single Pb-cell generates a nominal voltage of approximately 2.1 V when fully charged. In the charged state the metallic Pb negative electrode and the lead sulphate positive electrode are immersed in a dilute sulfuric acid (H_2SO_4) electrolyte (Reddy & Linden, 2010). Reddy & Linden (2010) stipulated that during the discharge phase, electrons are ejected out of the cell as lead sulphate is formed at the negative electrode while the electrolyte is gradually diluted. Pb-acid batteries are able to supply high surge currents, maintain a high-power density, allied with low cost and require minimum maintenance (Liu *et al*., 2018; Reddy & Linden, 2010). However, they have a low energy density, limited depth-discharge level and battery materials are environmentally unfriendly (Liu *et al*., 2018).
- **Nickel–Cadmium Battery (Ni-Cd**): Ni-Cd batteries utilises NiOOH and metallic Cd plates as electrodes. However, Cd metal was banned for most applications by the European Union in 2004 because of its highly toxic nature (European Parliament, 2018; Reddy & Linden, 2010). Ni-Cd batteries have been nearly substituted exclusively by NiMH batteries (Lewis *et al*., 2004).
- **Nickel–Metal Hydride Battery (NiMH)**: First commercial Ni-MH batteries were made available in 1989. They are now an established consumer and industrial product. The battery houses a hydrogen-absorbing alloy (metal hydride) for the negative electrode instead of cadmium. The battery is less prone to cyclic memory effect than Ni-Cd, environmentally friendly, contains only mild toxic contaminants, utilise Ni material which makes recycling profitable, exhibit 35–45% higher capacity than a standard Ni-Cd, subject to simple storage and transportation and are not subject to regulatory control (Lewis *et al*., 2004; Reddy & Linden, 2010). However, they are susceptible to limited cycle life (deep discharge reduces cycle life), requires complex charge algorithms, doesn't absorb overcharge readily, trickle charge must be kept low, generates heat during fast-charge and high-load discharge and akin to high self-discharge when not in use (Ada, 2018; Lewis *et al*., 2004).
- **Lithium-Ion Battery (Li-ion)**: Li-ion is the sole choice in many consumer electronics and possesses one of the best energy density and efficiency levels, however, it suffers from a slow self-discharge when not in use (Lewis *et al*., 2004). Although Li-ion batteries have a market share of over 55% in the small portable electronic devices market, there are still some challenges hindering the development of large-scale Li-ion batteries (Reddy & Linden, 2010).

The main obstacles include the entailed high capital costs of more than R18000/kWh (due to special packaging), internal overcharge protection circuits and very short cycle life (Ada, 2018; Lewis *et al*., 2004; Liu *et al*., 2018). However, intense research is underway in an attempt to slash the cost and increase the life of the battery (Nitta *et al*., 2015; Liu *et al*., 2018).

- **Lithium-Ion Polymer Battery (Li-Poly)**: Li-Poly batteries are light in weight and can be moulded into any shape desired. Apart from being ultra-light, the battery has high power density, high capability and high cell voltage, however, they are costly, delicate and can explode if misused (Ada, 2018).
- **Nickel–Iron Battery (Ni-Fe)**: Ni-Fe batteries utilise NiOOH and metallic Fe as electrode materials. Ni–Fe cells provide 1.5–2 times the energy density of Pb-acid batteries, with their increased ruggedness and longer cycle life at deep discharge state (2000 cycles at 80% Depth of Discharge) (Abdalla *et al*., 2016). In addition, Ni-Fe batteries are well known for their low cost (<R12000/kWh), long cycle life, typically exceeding 4000 cycles of charge and discharge vastly exceeding most of their competing technologies, which include Pb-acid (400 cycles), Ni-Cd (1600 cycles), and Ni-MH (600–900) (Helwig & Ahfock, 2013; Ibrahim *et al*., 2008; Iron Edison Co., 2019; Poullikkas, 2013; Liu *et al*., 2018).

Among various energy storage technologies, Ni-Fe battery-based electrochemical energy storage offers an ideal practical solution that would help balance the electrical energy grid by mitigating the asynchronous impediment between energy generation and demand (Abdalla *et al*., 2016). Ni-Fe batteries serve as an ideal energy storage system because of its abundant availability of raw materials, environmental friendliness, electrical and mechanical abuse tolerance, long operational cycle life and compatibility with photovoltaics (PVs) (Abdalla *et al*., 2016; Helwig & Ahfock, 2013; Zhao *et al*., 2015).

In addition to the above, this technology is ideal for stationary applications with low gravimetric energy attributable to the nature of the heavy metals utilised in its construction (Posada & Hall, 2016). Consequently, there is a superfluity of reasons to forecast a large-scale utilization of this battery technology. Attributable to their outstanding safety properties (zero flammability, fail-safe, electrochemical abuse tolerance), low cost and long cycle lifespan (Abdalla *et al*., 2016; Zhao *et al*., 2015), the anticipation that Ni-Fe will commercially bloom and edge out other competing technologies for customer-connected energy storage is inevitable. However, although appealing, there are a plethora of hurdles to overcome first, such as increasing the

coulombic efficiency, averting electrolyte decomposition, inhibiting the evolution of hydrogen, and increasing energy and power densities (Kao *et al*., 2011).

2.3 Nickel-Iron Battery Background

2.3.1 Discovery of Alkaline Nickel-Iron Battery

In 1899 Waldemar Jungner from Sweden discovered the first rechargeable battery in which an alkaline electrolyte is used, such as an aqueous solution of KOH or NaOH (Linden & Reddy, 2002; Bernard & Lippert, 2015). Linden & Reddy (2002) and Bernard & Lippert (2015) added that Jungner focused on Ni-Cd and Ni-Fe as the active materials of the system. The American Thomas Edison claimed to invent and subsequently patented the Ni-Fe battery in 1901. Patent litigation led to the collapse of Jungner's company and Jungner then focused on the Ni-Cd system, using a pocket plate electrode design. Edison developed the Ni-Fe system based on a tubular electrode design, which was primarily envisioned for electric vehicles.

By 1903 the Edison Storage Battery Company introduced the Ni-Fe battery to the market (Edison *et al*., 1924). From the start, the Ni-Fe battery already showed an impressive lifetime of >3000 cycles with energy efficiency (coulombic efficiency) of 55-75% resulting in a cycle life ranging from 20-50 years (Linden & Reddy, 2002). This is considered to be due to its well-devised robust cell design, shown in Figure 2-11.

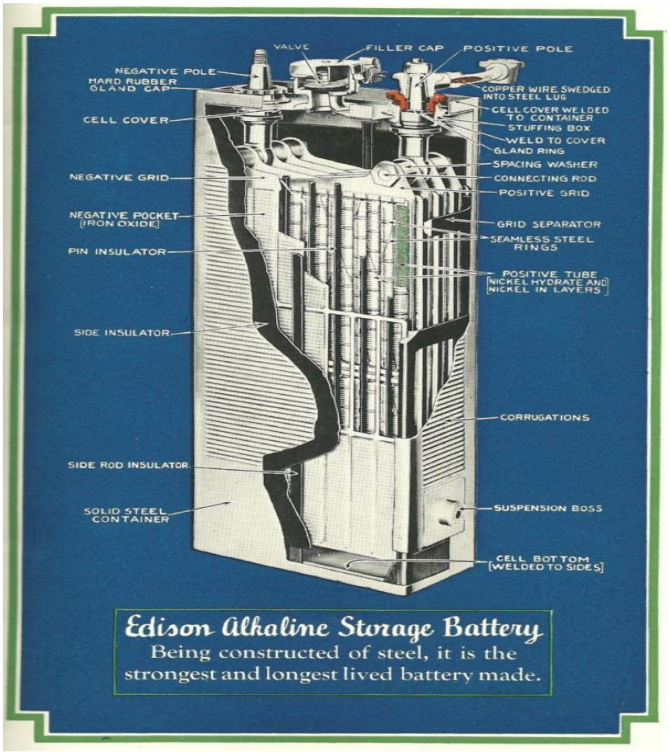

Figure 2-11: Advertisement and cross-section of the first Ni-Fe battery (Used from Edison *et al.*, 1924)

2.3.2 Basic Operational Principal of a Battery

A battery is a device constituting one or more electrochemically reversible cells that reversibly convert stored chemical energy into electrical energy. Primary (non-rechargeable) batteries are discharged once and discarded thereafter because the electrode active materials are irreversibly converted during discharge. Secondary (rechargeable) batteries are able to be discharged and recharged multiple times by applying electrical current; reversing the current will reinstitute the original composition of the electrodes. When a battery is discharging (supplying energy or doing work), its negative terminal is the anode and its positive terminal is the cathode and when a battery is charging (accepting electrical charge), its negative terminal is the cathode and its positive terminal is the anode (Reddy & Linden, 2010).

Each electrochemical cell in a battery comprised of half-cells coupled in an ion-conductive electrolyte solution constituting cations and anions (Reddy & Linden, 2010). Reddy & Linden (2010) stated that one half-cell constitutes and the negative electrode and electrolyte solution, the negative electrode is where anions (negatively charged ions) migrate to during discharge; the other half-cell constitutes the positive electrode and the electrolyte, the negative electrode is where cations (positively charged ions) migrate to during discharge. Redox reactions,

transpiring between two electrodes immersed in the electrolyte, are responsible for power generation from the battery. Cations are reduced (electrons are accepted) at the cathode during charging, while anions are oxidized (electrons are emitted) at the anode during charging (Abadalla *et al*., 2016). Abadalla *et al*. (2016) added that during discharge, the electrons transport processes are reversed. The electrode plates do not physically contact each other but are linked electrically via the electrolyte solution. Some cells utilise different electrolyte solutions for each half-cell compartment. A separator, inserted in-between electrodes, prevents mixing of the electrolytes and electrical short-circuits while allowing ionic charge carriers to shuttle between half-cells.

Each half-cell generates a force defined by its ability to drive electrical current from the electrode to the exterior circuit of the cell, this force is termed electromotive force (emf). The net emf of the cell is the difference between the emfs of its respective half-cells. (Reddy & linden, 2018). Thus, if the electrodes have emfs $\mathcal{E}_1$ and $\mathcal{E}_2$, then the net emf $\mathcal{E}_1$-$\mathcal{E}_2$ is in other words, the difference between the reduction potentials of the half-cell reactions. The basic illustration of a galvanic cell (Ni-Fe) is depicted below in Figure 2-12.

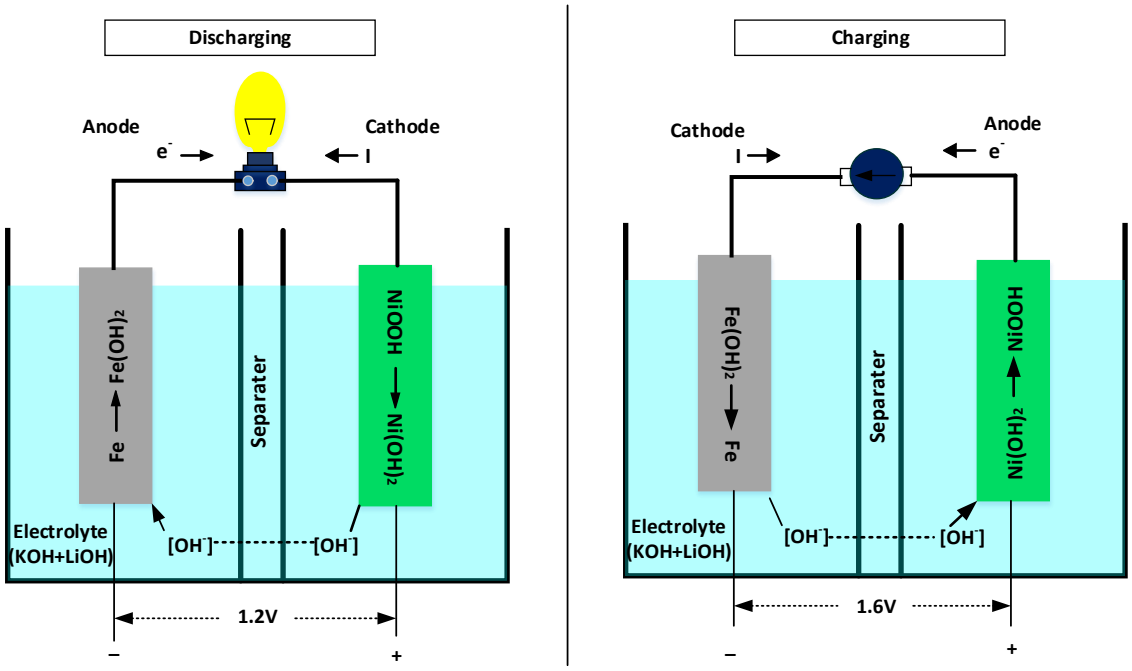

Figure 2-12: Illustration of a galvanic cell (Ni-Fe cell)

2.3.3 Nickel-Iron Battery Components

Ni-Fe battery technology is a rechargeable battery that generates electricity from a redox reaction. The basic configuration of a conventional Ni-Fe battery consists of four chief components (as illustrated in Figure 2-12) (Brown *et al*., 1974; Narayan *et al*., 2015):

1) The positive electrode, predominantly composed of NiOOH material

2) The negative electrode, a composite with predominately Fe/FeS material

3) An ionically conducting electrolyte usually an aqueous alkaline solution

4) An insulating separator usually a polymeric membrane

The prismatic configuration of Ni-Fe batteries is the most utilised design that can be easily found in the current market. A typical Ni-Fe prismatic configuration is depicted in Figure 2-13 below.

The overall reaction between cathode and anode is presented below:

$$2NiOOH+Fe+H_2O \leftrightarrow 2Ni(OH)_2 + Fe(OH)_2 \quad [2\text{-}1]$$

The battery has an open-circuit voltage (OCV) of approximately 1.30 V (Vijayamohanan *et al*., 1990). The components' prerequisite properties and functionality are discussed below.

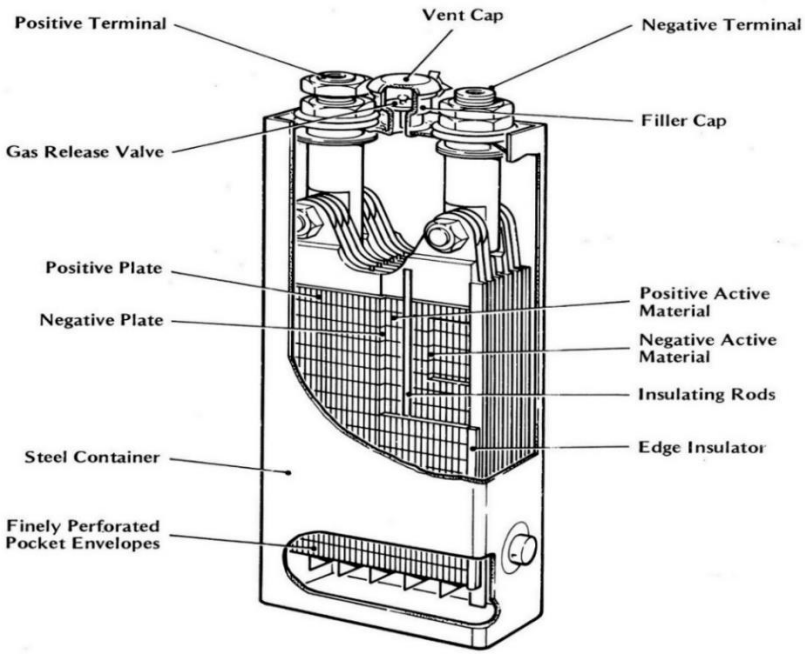

Figure 2-13: Components of a nickel-iron battery cell (Vmack Co, 2018)

2.3.3.1 Positive Electrode

The positive electrode in Ni-Fe cells is based on the NiOH/NiOOH material (Reddy & Linden, 2010). An electroconductive substrate is coated or impregnated with NiOH/NiOOH active material to construct the positive electrode (Linden & Reddy, 2010; Chakkaravarthy *et al*., 1991). Two polymorphs of $Ni(OH)_2$ exist, they are α-$Ni(OH)_2$ and β-$Ni(OH)_2$; they can be transformed into γ-NiOOH and β-NiOOH, respectively (Chakkaravarthy *et al*., 1991). However, the β- $Ni(OH)_2$ is typically utilised as precursor electrode material in alkaline Ni-based batteries due to the poor stability of α-$Ni(OH)_2$ in alkaline mediums (Reddy & Linden, 2010; Medway *et al*., 2006). In recent years, in order to amplify the electrochemical performance of the battery, several additives and nanostructured materials have been integrated into the electrode. These modifications will be further discussed in Section 2.4.

The positive electrode (composed of NiOOH) accepts electrons from the external circuit during the discharge phase of the battery. During this process, the positive active electrode material is reduced, and consequently termed as the cathode. The half-reaction for the oxidation of the active positive electrode material is pronounced by the Equation 2-2:

$$2NiOOH+2H_2O+2e^- \underset{Charge}{\overset{Discharge}{\rightleftharpoons}} 2Ni(OH)_2+2OH^- \quad [2\text{-}2]$$

During the charge phase, the positive electrode emits electrons to the external circuit. In practice, the positive electrode exhibit high efficiency as a reducing agent, stability in the presence of an electrolyte, useful working voltage, ease of modification and low cost (Narayan *et al*., 2015).

2.3.3.2 Electrolyte

Manohar *et al*. (2012) stated that the electrolyte solution is an ionic conducting medium with negligibly small electro-conductance. The solution acts as a medium for unrestricted migration of ions (at optimal levels) between the negative and positive electrodes and prevents short circuits. The electrolyte provides an ion transfer channel linking the negative and positive plates to generate an electrical pressure (voltage). Ni-Fe cells utilise strongly alkaline solutions of KOH/LiOH with nominated additives (such as sulphide salts) utilised to avert electrolyte decomposition (Manohar *et al*., 2012).

In recent years, in order to modify the electrochemical performance of the Ni-Fe battery, several additives have been added to the electrolyte solution. This modification will be further discussed in Section 2.5.

Ideally, electrolytes should exhibit high ionic conductivity, low to zero electric conductivity, non-reactivity with electrode active materials, safeness in handling and low cost and properties resistant to temperature fluctuations (Kao *et al*., 2016).

2.3.3.3 Negative Electrode

The negative electrode is an electrode, where the oxidation reaction transpires during the charging process. An electroconductive substrate is coated or impregnated with Fe active material to construct the negative electrode (Linden & Reddy, 2010). Linden & Reddy (2010) annotated that the Fe active electrode material facilitates the flow of electric current through the external circuit while actuating reversible absorption/emission of electrons emitted/absorbed by the negative electrode. It releases electrons to the external circuit and oxidises elemental iron (Fe) to ferrous iron (Fe^{2+}) during the electrochemical reaction. Similarly, the reduction of ferrous ion (Fe^{2+}) to elemental iron (Fe) occurs during charging of the same electrode. In recent years, in order to modify the electrochemical performance of the battery, several additives and nanostructured materials have been integrated into the electrode. These modifications will be further discussed in Section 2.6.

Equation 2-3 illustrates the charge and discharge (backward and forward reactions respectively) reactions transpiring at the Fe-based electrode in a strongly alkaline medium:

$$Fe + 2OH^- \underset{\text{Charge}}{\overset{\text{Discharge}}{\rightleftharpoons}} Fe(OH)_2 + 2e^- \qquad [2\text{-}3]$$

In practice, negative electrode exhibits high efficiency as an oxidising agent, high charge output, moderate to high electro-conductivity, ease of modification, low capital cost and physical stability (Posada *et al*., 2017).

2.3.3.4 Minor Components

Minor components complete the design of a Ni-Fe battery; these components exhibit little to no influence on the overall electrochemical performance of the battery. The components involved in the battery construction include;

- **Case**: a closed vessel which houses all the battery components and electrolyte solution.
- **Cover**: permanent or removable seal (for ease of battery maintenance) at the top of the battery case. Its design constitutes outlets for battery terminals and gas vents.
- **Plates**: composed of positive and negative plates. It contains the active materials for both anode and cathode, batteries constituting more plates produces more energy.
- **Separators**: thin, porous ion-permeable membranes are positioned in-between negative and positive plates to avoid short-circuiting (resulting from direct contact of polarised plates) the battery. The membranes, typically microporous layers composed of polyethylene and polypropylene, are designed to allow the passage of the ions (Brown *et al*., 1974; Narayan *et al*., 2015). Separators ensure that electrons can only shuttle from the anode to the cathode via the external circuit.
- **Vent Caps**: they allow regulated expulsion of hydrogen gas produced during charging and the level of the electrolyte during battery maintenance.
- **Terminals**: Positive and negative electrical contacts on the case top, they have thick and heavy metal connectors allowing it to collect the current generated by the battery or to charge it.

2.3.4 Nickel-Iron Battery Characteristics

Typically, the electrochemical performance of a Ni-Fe battery relies primarily on the properties of the positive electrode, negative electrode and the electrolyte solution. The electrochemical performance is assessed and measured through a number of variables which include capacity, efficiency, discharge and charge characteristics, charge retention, cyclability and safety and environmental friendliness (Abdalla *et al*., 2016; Chakkaravarthy *et al*.,1991; Comisso, & Mengoli, 2007).

2.3.4.1 Capacity and Rate Capability

The energy capacity of the Ni-Fe battery is electrochemically limited by the energy capacity of the positive Ni-based electrode and, hence, is a function of the active material quantity deposited on the positive plate (Reddy & Linden, 2010). The 5-h discharge rate (0.2C or 5C) is the frequently utilised reference for rating its energy capacity (Sichuan Changhong Battery Co., Ltd, 2008).

The conventional Ni-Fe battery effuses moderate energy and power and density and is designed primarily for applications demanding low to moderate discharge rates (<C10) (Hariprakash *et al*. 2005). The battery is not ideal for high discharge rate applications such as starting an automobile engine (Eyer, 2018). The build-up of internal resistance in the battery lowers the terminal voltage significantly when high discharge rates are employed (Chakkaravarthy *et al*. 1991; Reddy & Linden, 2010). The correlation between capacity and hourly rate of discharge is depicted in Figure 2-14. As depicted by Figure 2-14, the maximum capacity of the Ni-Fe is attained when the discharge current is optimum at 5-h discharge rate (C5 or 0.2C).

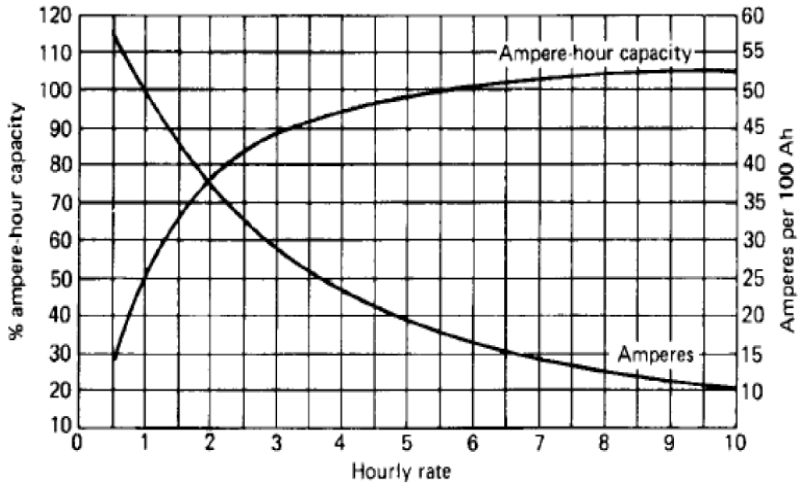

Figure 2-14: Correlations between capacity and discharge rates at 25°C; end voltage 0.8 V per cell (Reddy & Linden, 2010)

If a Ni-Fe battery is discharged at a high rate in one cycle and then discharged at a lower rate in the subsequent cycle, the sum of the capacities delivered at the high and low rates approximately equals the capacity that will be attained at the single optimal discharge rate (Chakkaravarthy *et al*. 1991; Reddy & Linden, 2010).

2.3.4.2 Efficiency

The energy efficiency of Ni-Fe (including Ni-base batteries) batteries can vary, depending primarily on the design and application of the battery, composition of electrodes (positive and negative electrodes) and operating conditions. Round-trip energy efficiencies of Ni-Fe batteries range from 65% to 80%, not including energy losses owing to power conditioning and ancillary equipment such as cooling system (EPRI-DOE, 2003).

The following factors possess the highest impact in determining the efficiency of a Ni-Fe battery (Sichuan Changhong Battery Co., Ltd, 2008; EPRI-DOE, 2003; Ibrahim *et al*., 2008):

- Electrolyte concentration: Electrolyte solution concentration can be modified to optimize voltaic and energy efficiency.
- Charging program: Charging at high charge rates to high-end voltages yields lower voltaic and energy efficiency. Prolonged overcharging will lower energy efficiency, as the majority of overcharge input is channelled to hydrogen evolution through electrolysis. Some studies have specified that pulse charging can boost both the voltaic and energy efficiency of a battery.
- Stand-time: If a battery is kept charged in an open-circuit state, it will lose energy through self-discharge (15% of its nominal capacity in the first 10 days), reducing the overall energy efficiency when it is discharged.
- Operating temperature: Operation at higher temperatures effectuates poorer charging efficiencies.

2.3.4.3 Discharge and Charge Characteristics

The Ni-Fe battery delivers partial to full nominal capacity at any discharge rate, but the discharge should be aborted beyond the point where the discharge capacity nears exhaustion. The battery functions optimally when adapted to low or moderate discharge rates (0.15C-1C) (Exide Industrial Marketing Divisions of ESB, Inc, 1966). EPRI-DOE (2003) reported that the cut-off voltage during discharge depends on the battery's application and the desired cycle life but is conventionally between 0.6 and 1 V_{dc}/cell. In addition to the above, the nominal voltage for most Ni-Fe batteries is about 1.2 V_{dc}/cell. The charge cut off voltage widely enrolled to limit hydrogen gas evolution is approximately 1.6 V_{dc}/cell. Figure 2-15 and Figure 2-16 illustrate the charge and discharge characteristics of a typical Ni-Fe battery.

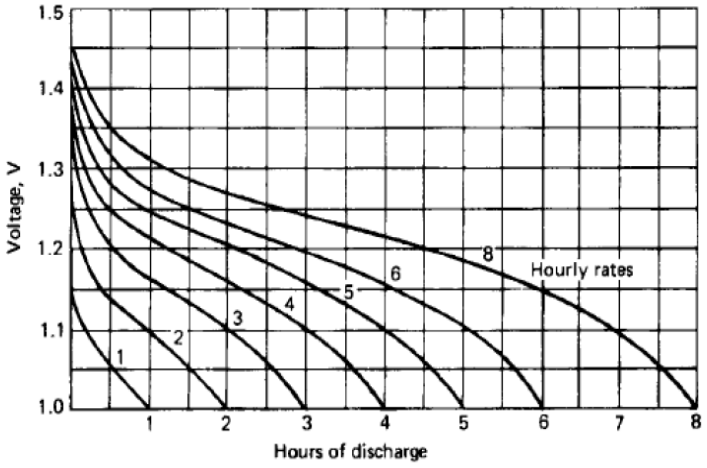

Figure 2-15: Time-voltage discharge curves of the nickel-iron battery (Reddy & Linden, 2010)

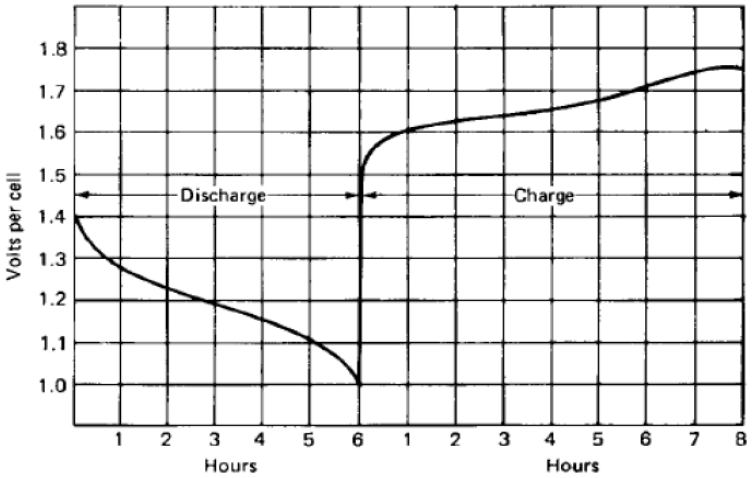

Figure 2-16: The typical voltage characteristics during constant-rate discharge and (Reddy & Linden, 2010)

Full charged state of the batteries can be attained by deploying a variety of configurations and schemes. As long as the charging current does not generate excessive hydrogen gassing (spray out of the vent cap) or temperature rise (above 40°C), any current or charge rate can be utilised (Exide Industrial Marketing Divisions of ESB, Inc, 1966).

Excessive hydrogen gassing will be temporarily combated by the frequent addition of water. If the cell voltage is limited to 1.6 V, excessive gassing scenario should be avoided (EPRI-DOE, 2003). Typical charging curves are given in Figure 2-17 below. The ampere-hour energy input (charge capacity) should constitute 10 to 40% in excess of the previous amp-hour energy output (discharge capacity) in order to ensure attainment of full charge (Reddy & Linden, 2010). Reddy & Linden (2010) added that the suggested charge rate is normally between 0.125C and

0.2C. These rates deliver the approximate nominal capacity in the 5-8 hr time frame. This is illustrated in Figure 2-17 below.

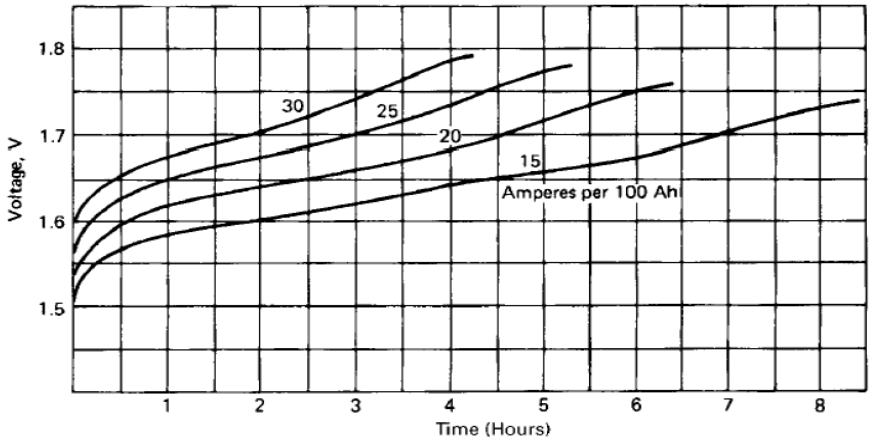

Figure 2-17: Typical charging voltage for a nickel-iron battery at various rates (Reddy & Linden, 2010)

2.3.4.4 Charge Retention

Ni-Fe batteries lose charge slightly more quickly than Ni-MH, Li-ion, Pb-acid batteries and various other energy storage technologies. Linden & Reddy (2010) reported that at room temperature, fully-charged Ni-Fe batteries lose 2% to 10% of their amp-hour energy input (charge capacity) per month. By comparison, Pb-acid batteries lose about 1% of their amp-hour energy input per month. The rate of charge loss trails a decaying exponential curve thus the majority of amp-hour energy input is lost immediately after charging.

Self-discharge, in Ni-Fe batteries, emerge from multiple sources (Comisso & Mengoli, 2007). The dominant source is the slow conversion of NiOOH to $Ni(OH)_2$, along with corresponding reactions on the counter electrode (EPRI-DOE, 2003). There is an additional mechanism of hydrogen diffusing to the positive electrode and reacting directly with the Ni-based active material (Chakkaravarthy, 1991). In addition, there is also the possibility of a leakage of current contributing to the loss of charge (EPRI-DOE, 2003). EPRI-DOE (2003) attributed the charge loss to resistive external current paths, electrode damage or separator decay. The rate of self-discharge or charge loss increases rapidly with an increase in temperature. This correlation generates several critical issues in system design.

Shukla *et al.* (1994) indicated that Ni-Fe batteries possess extreme sensitivity to temperature gradients. If two cells in the same battery are operating at different temperatures, their self-discharge rates will be different, leading to a specific capacity variance over time. This can lead

to overcharging or current reversal, potentially instigating battery damage. Another important factor of the Ni-Fe battery characteristics is the effect of temperature (includes also potential thermal runaway scenarios), which is discussed below (EPRI-DOE, 2003). Sealed battery designs are generally much more susceptible to thermal runaway incidences than vented battery designs (Hariprakash *et al*., 2005).

2.3.4.5 Effect of Temperature

While Ni-based batteries are generally less temperature sensitive than other competing battery technologies (Li-ion, Pb-acid, Ni-Cd, Ni-MH etc), the temperature can possess hefty negative effects on the inclusive electrochemical performance and life of the battery, the effects are summarized below as stipulated by EPRI-DOE (2003):

- Internal resistance: Internal resistance decreases when the internal temperature rises. The decrease in internal resistance is attributed to the increase in electron mobility.
- Self-discharge: The rate of self-discharge (charge loss) increases when the internal temperature rises, as the electrochemical reactions inducing capacity loss accelerate.
- Open Circuit Voltage (OCV): OCVs increase at higher temperatures due to inflated thermodynamic effects. In addition, since internal resistance is low at higher internal temperatures, over-voltages are lower for a specified current. These effects work collectively during discharge at high temperatures to effectuate higher discharge voltages but work against each other during charge consequently generating little effect.
- Capacity: Charge capacity decreases when the battery is charged in very high ambient temperatures, largely as a consequence of self-discharge.
- Life: Operation and storage at higher temperatures reduce the life of the battery. In general, the rate of ageing amplifies when operated and stored at higher temperatures.

Smart battery design can, to a certain extent, circumvent the apparent trade-offs associated with temperature (Ravikumar *et al*., 1995; Reddy & Linden, 2010; Jensen, 2013). Ravikumar *et al*. (1995) and Reddy & Linden (2010) illustrated with an example that operation of a Ni-Fe battery in cold ambient temperatures will result in higher charge capacity (that is ampere-hour energy input) but lower discharge voltage, while operation in warm ambient temperatures will result in higher discharge voltage but lower charge capacity. This is an apparent trade-off in battery design. It has been demonstrated, however, that if the battery is charged in a cold bath

and then warmed just before discharge, it will yield the high charge capacity of a cold battery at the high discharge voltage of a warm battery, increasing the overall energy density.

Many Ni-Fe batteries, mostly sealed Ni-Fe batteries, experience a condition termed "thermal runaway." This occurs when the internal temperature of the battery surpasses a certain critical temperature, attributable to high ambient temperature, high-rate charge or discharge, or overcharge. The elevated temperatures accelerate the rate of self-discharge rate. The energy lost by the cell through self-discharge is converted to heat, which heats the cell further. This malicious cycle continues until the battery fails, usually through separator decomposition or melting or failure of some other battery component(s). In some designs of Ni-Fe batteries, such as sealed Ni-Fe batteries, thermal runaway can lead to rupture of the casing, potentially creating a hazardous situation.

Thermal runaway scenarios can be avoided by integrating a proper cooling system onto the battery or by avoiding very high charge currents and long periods of overcharge. Thermal runaway in vented batteries is unlikely except in specific circumstances, such as high-rate charging or prolonged exposure of electrode plates in an electrolyte starved medium.

2.3.4.6 Cyclability

The key advantages of employing the prismatic Ni-Fe battery are its extremely long life, rugged and robust construction (Abadalla *et al*., 2016). Chakkaravarthy *et al*. (1991) explained that battery life varies with the nature of application but typically ranges from 10 years for heavy-duty applications to 20 years or more for standby or float service applications. When operated with moderate care, 2000 cycles are feasible; with optimal care, for example, by limiting temperatures to below 35°C, cycle life of 4000 to 5000 cycles has been attained.

The battery is less damaged by electrochemical abuse (repeated deep discharge) than any other battery technology (Ferrando *et al*., 1984). In practice, an operator will drive an electronic vehicle (battery-operated vehicle) until it stalls, at which point the battery voltage is only a minute fraction of the volt per cell (some cells may be in reverse). This kind of abuse has minimal effect on the life of a Ni-Fe battery in comparison to other technologies (Hariprakash, 2005). Cycling stability of a typical Ni-Fe battery is depicted in Figure 2-18 below.

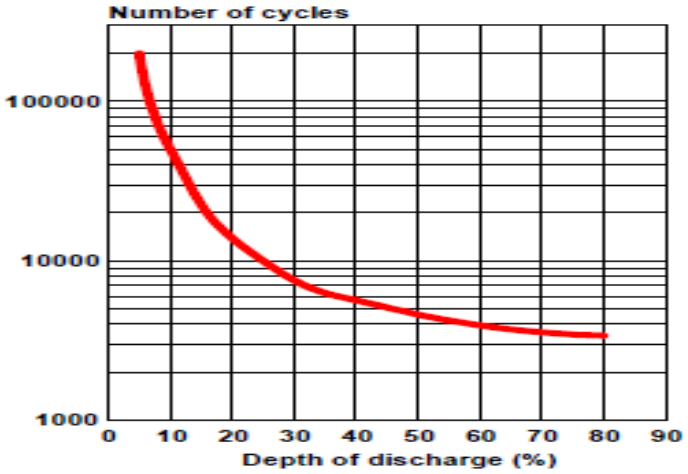

Figure 2-18: Cycle life as a function of depth-of-discharge for a typical Ni-Fe cell (Reddy & Linden, 2010)

2.3.4.7 Safety and Environment

The safety glitches associated with Ni-Fe batteries are similar to those allied with most other battery technologies. Ni-Fe batteries contain caustic materials (KOH/LiOH as electrolyte) which, if chemically spilt, can pose a stern health hazard to operating personnel. Other materials contained in the batteries, like $Ni(OH)_2$, also poses a serious health hazard if ingested or contacted with human skin.

All Ni-Fe batteries generate a certain amount of hydrogen and oxygen during charging due to electrolysis of water in the aqueous electrolyte. In sealed battery systems integrated with a recombination catalyst (like palladium), the hydrogen and oxygen routinely recombine inside the battery/cell and do not pose a health and safety hazard to operating personnel (Shukla *et al.*, 1994; Reddy & Linden, 2010). Reddy & Linden (2010) elucidated that if sealed cells are charged at a very high charge rate, the hydrogen evolution rate may outpace the rate of gas recombination. This scenario will lead to pressure build-up within the battery/cell. In most batteries/cells, a safety valve is designed and installed into the battery system to relieve pressure before the casing ruptures. In such cases, the battery/cell may be ruined but hazardous conditions are generally averted.

In vented systems, the hydrogen and oxygen gases generated during charge are vented to the atmosphere. Vented battery systems must be situated in a well-ventilated location where

hydrogen gas will be purged to the atmosphere rather than accumulate. Ni-Fe batteries constitute transition metals, as electrodes, which can contaminate earth (soil) and groundwater. This consequence is inevitable for Fe as well as for Ni.

In general, Ni-Fe batteries/cells are highly recyclable, and organisations operate in most countries to gather and recycle waste resulting from the disposal of these batteries in a safe, secure and effective manner (EPRI-DOE, 2003).

2.4 Positive Electrode Material Development

2.4.1 Electrochemistry

Ni-based material is employed as the positive electrode in Ni-Fe batteries. The Ni-based electrodes exhibit ample specific capacity (ranges 0.100-0.260 $Ahg^{-1)}$ (Chakkaravarthy *et al*., 1991; Chen *et al*., 2013). The active material NiOOH is generated from the precursor material, $Ni(OH)_2$ (Medway *et al*., 2005; Narayan *et al*., 2015; Shukla *et al*., 1994). The reversible charge/discharge reaction is denoted as:

$$NiOOH + H_2O + e^- \underset{\text{Charge}}{\overset{\text{Discharge}}{\rightleftharpoons}} Ni(OH)_2 + OH^- \qquad E^O = -0.490\ \text{V} \qquad [2\text{-}4]$$

The electrochemical reaction mechanism comprises hydrogen ions diffusion through the $Ni(OH)_2$ and NiOOH solid-state lattices to effectuate a continuous change in the composition of the electroactive material (Constantin *et al*., 1998). The actual path of the electrochemical reaction may be denoted as:

$$NiOOH + H^+ + e^- \underset{\text{Charge}}{\overset{\text{Discharge}}{\rightleftharpoons}} Ni(OH)_2 \qquad [2\text{-}5]$$

As stipulated by Chakkaravarthy *et al*. (1991), there are numerous crystallographic polymorphs of $Ni(OH)_2$ and NiOOH i.e. α and β. Chakkaravarthy *et al*. (1991) and Bernard & Lippert (2015) indicated that $Ni(OH)_2$ can exist as α-$Ni(OH)_2$ and β-$Ni(OH)_2$ polymorphs in Ni-based positive electrodes. α-Ni(OH) encompasses a sandwich-model structure with intercalated water molecules while β-$Ni(OH)_2$ houses a layered brucite structure with minute amounts of loosely bound water molecules produced by electrochemical precipitation from a concentrated $Ni(NO_3)_2$ solution.

$[Ni(NO_3)_2.6H_2O]$ on oxidation in an alkaline medium, yields hydrated γ-NiOOH and β-$Ni(OH)_2$ is produced by chemical precipitation with concentrated alkaline solution. On oxidation, it

yields β-NiOOH (Chakkaravarthy *et al*., 1991). Overcharging of Ni-based electrodes converts β-NiOOH to γ-NiOOH and on discharge, the α-$Ni(OH)_2$ produced from γ-NiOOH can be dehydrated to form β-$Ni(OH)_2$ (Medway *et al*., 2005). Thus, the electrochemical process of charging and discharging can be represented as illustrated in Equation 2-6.

Electrochemical Reactions

$$\begin{array}{ccc} \alpha\text{-Ni(OH)}_2 & \underset{\text{Charge}}{\overset{\text{Discharge}}{\rightleftharpoons}} & \gamma - \text{NiOOH} + \text{H}^+ + e^- \\ \uparrow\downarrow & & \uparrow\downarrow \\ \beta - \text{Ni(OH)}_2 & \underset{\text{Discharge}}{\overset{\text{Charge}}{\rightleftharpoons}} & \beta - \text{NiOOH} + \text{H}^+ + e^- \end{array} \qquad [2\text{-}6]$$

The electrode composite structure, morphology and manufacturing techniques exhibit a prominent influence on the electrochemical performance of the negative electrode (Chakkaravarthy *et al*., 1991; Medway *et al*., 2005).

2.4.2 Composite Structure

Composite electrode structure modification is a process that produces electrodes with comparatively high electroactive material content and optimal electrochemical performance (Ferrando *et al*., 1984). Composite electrodes possess good electrical conductivity and offer high energy and power density (Constatin *et al*.,1998). The Ni composite electrodes exhibit excellent electrochemical characteristics marked with energy densities between 120 and 180 $Ahkg^{-1}$ (Chakkaravarthy *et al*., 1991). Ferrando *et al*. (1984) stipulated that Ni-coated fibre, chopped graphite fibre or Ni fibre is subjected to compact sintering to produce a highly porous fibre mat. The latter is loaded with $Ni(OH)_2$, coupled with a small percentage of $Co(OH)_2$, through electrochemical precipitation to produce a composite electrode with high specific capacity and efficiency.

Certain metal complexes within the active mass create stacking faults and thwart the formation of aggregates. In catalysis literature, the stacking faults are believed to increase reactivity coupled with the preservation of the solid mass homogeneity added that $Co(OH)_2$, which is isostructural with β-NiOOH and β-$Ni(OH)_2$ is often used as a spacing agent additive. A spacing agent creates a disordered structure by occupying layers between layers of the β-$Ni(OH)_2$, consequently yielding stacking faults that curtail the formation of aggregates.

Shukla *et al*., (1994) and Bernard & Lippert (2015) elucidated that cobalt as an additive reduces both the oxidising and the reducing potentials of $Ni(OH)_2$ and increases the overpotential of oxygen gas evolution. Constatin *et al*. (1998) noted that a composite mixture of $Co(OH)_2$ and $Cd(OH)_2$ increases the discharge capacity and coulombic efficiency of Ni electrode by enhancing the reversibility of the electrode's electrochemical reactions and curtailing of the parasitic oxygen evolution. Thus, by surging further the utilization coefficient of the NiOH/NiOOH active material, $Co(OH)_2$ stabilizes the cycling capacity of Ni-based electrodes. Barium (as $Ba(OH)_2$) exhibit similar beneficial effects in the presence of lithium ions which are drawn from LiOH which is comprised in the KOH electrolyte (Chakkaravarthy *et al*., 1991).

Cadmium, magnesium and zinc-containing compounds also slightly avert the OER as $Co(OH)_2$ do (Mao *et al*., 1992). Mao *et al.* (1992) expounded that alkaline electrolyte-based systems need to deal with oxidized metal species that are less electronically conductive than pure metals. Hence, conductive additives, such as amorphous carbon and graphite can be necessary to induce and sustain conductivity, which also depends on the electrode production technology employed.

2.4.3 Nanostructure and Morphology

As mentioned in electrochemistry section, the active material of the negative electrode in alkaline aqueous batteries is $Ni(OH)_2$ in the beta morphology (β-$Ni(OH)_2$) (Shukla & Hariprakash. 2009). Bernard & Lippert (2009) expounded that both Ni hydride and Ni oxides are employed as precursor material. Both materials are readily converted to β -$Ni(OH)_2$ as it is the most feasible thermodynamically stable composition of Ni in an alkaline medium and preserves superlative stability due to its low solubility ($K_{sp}=10^{-35}M$). The reaction between β -$Ni(OH)_2$ and β -NiOOH is believed to be of a reversible solid state-nature at which a proton is inserted into the host structure (intercalation) (Shukla & Hariprakash. 2009; Bernard & Lippert, 2009; Shukla, 2001). Figure 2-19 depicts an illustration of the β -$Ni(OH)_2$ intercalated structure.

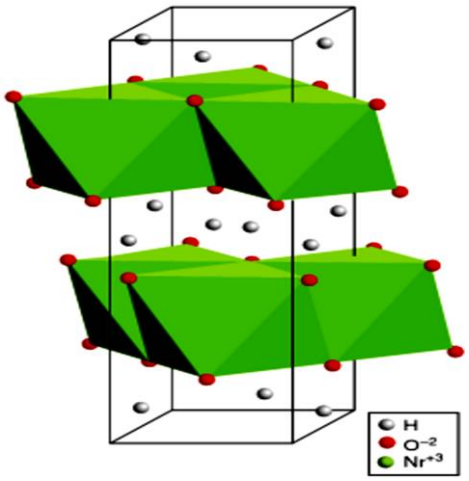

Figure 2-19: The $Ni(OH)_2$ layered crystal structure (Bernard & Lippert, 2009)

The slabs are layered as NiO_6 octahedra having hydrogen atoms located in between bound to the oxygen. The NiO_6 can be seen as the solid host structure with removable H atoms that occupy interstitial sites within the slabs. β-NiOOH is an electric semiconductor (10^4-10^5 Ω/cm at 25^{O}C).

Shukla *et al*. (2001) and Shukla & Hariprakash (2009) highlighted that during discharge the electrode attains $Ni(OH)_2$ species which are known to behave as an insulator (10^{10}-10^{12} Ω /cm at 25^{O}C). The formation of electrically insulating species affects the deep discharge capacity or can even lead to a decrease in reactivity by passivation, which is the formation of an insulating layer of $Ni(OH)^2$ around β-NiOOH particles that lowers the electric conductivity and active surface area.

Van der Ven *et al*. (2006) expounded that while the β-NiOOH/ β-$Ni(OH)_2$ reaction is seen as a solid-state mechanism the species involved are sparingly soluble, leading to dissolved intermediates. The dissolution of the species can act as rate-determining at high discharge rates. If both of the species involved in the Ni(II)/Ni(III) reaction would have poor electric conductance no electric conductance to the current collector could be attained leading to a general overall poor performance. Also, the formation of unfavourable species can trouble the performance.

Transformation pathways of the Ni-based electrode are eloquently illustrated by the Bode diagram, shown in Figure 2-20 (Bernard & Lippert, 2009). Bernard & Lippert (2009) and Van der Ven et al. (2006) elucidated that the two other phases need to be accounted for: γ-$H_xK_yNiO_2.H_2O$ in the charged state, where x and y are often claimed to be 0.33 and 0.66,

respectively, and α-NiOOH in the discharged state. By overcharge, the $H_xK_yNiO_2.H_2O$ can form and has an enlarged interlayer distance. Thereby it can intercalate species of the electrolyte solution in the structure, by which the electrode can dry-out. During discharge, in addition to the β-form also the $H_xK_yNiO_2.H_2O$ can form α-$Ni(OH)_2$, which in turn spontaneously reforms to β-$Ni(OH)_2$ overtime in base conditions. Higher theoretical specific capacity is expected for an electrode comprised of α-$Ni(OH)_2$ instead of β-$Ni(OH)_2$ due to the bigger interslab distance (Shukla, 2001; Van der Ven *et al*., 2006; Bernard & Lippert, 2009).

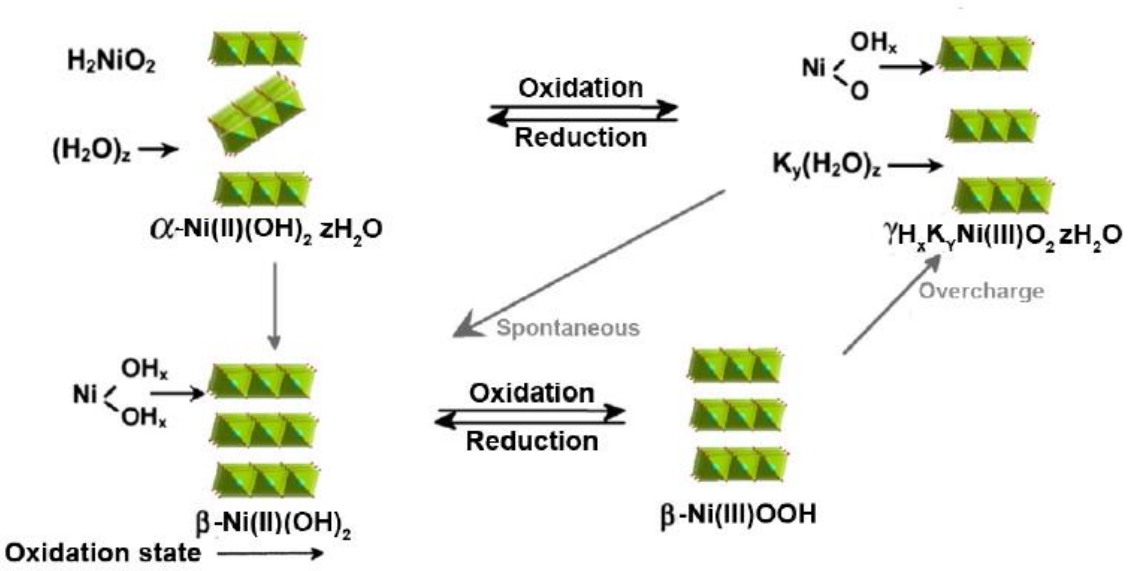

Figure 2-20: Bode diagram showing transformations among various phases of the nickel hydroxide (Bernard & Lippert, 2009)

Nonetheless, by the application of special preparation methods and the use of substances that improve the electrochemical performance of the electrode, so-called additives, the Ni-based electrode is known in literature for its excellent reversibility and cyclic behaviour (Shukla, 2001; Van der Ven et al., 2006; Bernard & Lippert, 2009; Shukla & Hariprakash. 2009). Bernard & Lippert (2009) and Shukla & Hariprakash (2009) added that the material characteristics of the species have been intensively studied in order to further improve the electrochemical performance. This has recently led to the suggestion that stacking faults, the interruption of the normal stacking sequence in the crystal structure, cause strong interactions between the Ni ions and protons. 15-20% stacking faults in the crystal structure are suggested to lead to near theoretical energy densities of 289 Ah kg^{-1} (Bernard & Lippert, 2009).

2.4.4 Electrode Production Techniques

Three different types of Ni positive electrode are widely employed i.e. (i) sintered, (ii) pressed and (iii) tubular or pocket.

2.4.4.1 Sintered Electrodes

Sintering is a thermal deposition process in which loose active particles are transmuted into a thin coherent porous matrix by heating in an inert atmosphere just below the melting point (of Fe). Carbonyl Ni powder is implanted bilaterally on an ideal current collector (substrate) and sintered in an inert atmosphere at approximately 1115 K to formulate a porous matrix (Ferrando *et al.*,1984). Chakkaravarthy *et al.* (1991) stated that the inert atmosphere can be either hydrogen, argon, nitrogen or a mixture of either of the gases. The substrate (current conductor) may be Ni mesh or Ni-plated mild or stainless steel mesh, perforated Ni foil or Ni-plated, perforated mild or stainless steel foil, Ni-fibre mat or Ni-plated steel-fibre mat.

Bilateral implantation of the carbonyl Ni powder on an ideal current collector process is carried out using a graphite mould (under dry conditions) prior to sintering. This process is titled 'loose sintering' or 'dry powder sintering'. 'Wet slurry sintering' is another process wherein a Ni powder slurry of ideal consistency implanted on a suitable substrate prior to sintering. These processes produce physically stable electrode plates of definite thickness and 70-90% porosity (Shukla *et al.*, 1994). $Ni(OH)_2$ and $Co(OH)_2$ can be deposited into the void spaces of the Ni substrates through vacuum impregnation or electrochemical deposition (Chakkaravarthy *et al.*, 1991; Shukla *et al.*, 1994).

The high electrical conductivity is due to the crystal binding between the active material in combination with high mechanical strength. However, sintered electrodes possess a relatively high inactive/active weight ratio and incur high production costs (Bernard & Lippert, 2015; Chakkaravarthy *et al.* 1991). Subsequent to the pocket plate technology, sintered electrodes have been the dominant technology as they allow higher charge/discharge rates than the pocket plate technology (Bernard & Lippert, 2015).

2.4.4.2 Tubular or Pocket Plate Electrodes

Back in 1897-1903, the first electrode design for Ni-Fe batteries was centred on the pocket-plate design. The typical pocket-plate technology design is depicted in Figure 2-21. (Chakkaravarthy *et al*., 1991). Pre-perforated Ni-plated steel sheets or thin Ni sheets are filled with palletized active material powder, which is blended with conductive additive, mostly graphite together with other suitable additives. The particles are then pressed and hold together as pockets with folded strips along the edges. The Ni pockets both acts as the holder of the small particles and current collector (Bernard & Lippert, 2015). Chakkaravarthy *et al*. (1991) highlighted that the existence of the current collector at the electrode/ electrolyte interface will effectuate an increase in the overpotential of the hydrogen evolution reaction. On the other hand, the Ni-based pockets also effectuate an increase in overpotential due to inevitable diffusion through the perforated steel and pressed palletized active material. Therefore, this design is chiefly suitable for low-current density applications. The pocket plate technology is still widely applied, presumably due to its robust design.

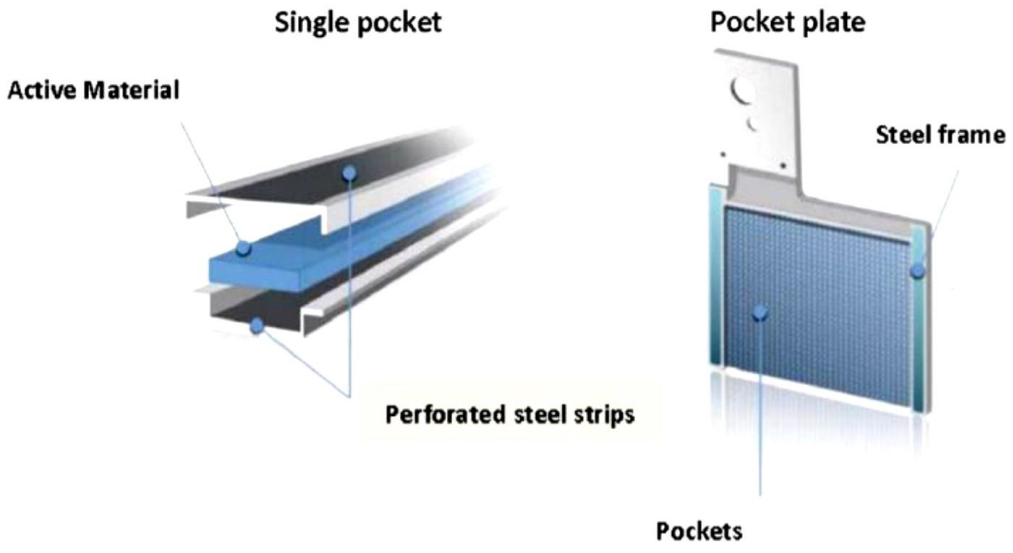

Figure 2-21: Pocket plate construction (Bernard & Lippert, 2015)

2.4.4.3 Paste Type Electrodes

The active material with sufficient additives is blended with an aqueous polymeric binder such as poly(tetrafluoroethylene) (PTFE) or poly(ethylene) (PE). The resulting mixture (paste) is pasted on a porous Ni-foam sheet to produce a plate of the desired thickness. The wet electrode is dried for 24-48 hours in a vacuum oven (Huang & Chou, 2007; Kao *et al*., 2011).

This design of flat paste type negative electrodes exhibits better performance than its counterparts (pocket type and sintered type electrodes) in terms of specific energy, volumetric capacity, ampere-hour capacity and Fe active material (Caldas *et al*., 1998). In addition, "paste plate" type electrodes production entails much lower costs, therefore, are more attractive than sintered electrodes counterparts (Manohar *et al*., 2012; Kao & Chou, 2010).

2.4.4.4 Pressed or Roll Compacted Electrodes

Ni-based active material composite mixture coupled with graphite powder and other additives in appropriate proportions is incorporated with a binder to formulate an electrode composite mix (PTFE, CA or PVDF) (Chakkaravarthy *et al*., 1991). The electrode composite material is hot pressed on an ideal electro-conducting mesh (usually Ni-mesh) or fed into a rolling machine along with the mesh (Caldas *et al*., 1998; Mrha *et al*., 1979). The thickness of the electrode plate is typically regulated by the applied pressure and the gap between the press plates (Chakkaravarthy *et al*., 1991). Chakkaravarthy *et al*. (1991) and Caldas *et al*. (1998) stressed that sometimes, a pore-formers such as minute NaCl or $(NH_4)_2CO_2$ particles are utilised to induce sufficient porosity. Pressed electrodes incur low-cost production and exhibit good charge characteristics and durability under optimal current drains (C/5-10).

2.5 Electrolyte Optimisation

The electrolyte solution utilised by Ni-Fe cells constitutes strongly alkaline solutions of KOH and LiOH and selected sulphide salts (such as K_2S) additives to avert electrolyte decomposition (Manohar *et al*., 2012). Traditionally, the mitigation of hydrogen evolution during charging has been attained by either modification of the composite Fe-based electrode or by the addition of additives that increase the hydrogen overvoltage to the electrolyte solution (Posada *et al*., 2017). Various electrolyte additives such as wetting agents, long-chain thiols and organic acids amongst others, have been investigated but yielded non-significant outcomes (MacKenzie & Salkind, 1968; Manohar *et al*., 2013; Malkhandi *et al*., 2012; Shruthi *et al*., 2015).

The electrolyte used in Ni-Fe batteries is approximately 25-30 wt.% KOH solution and typically contains approximately 50 g dm^{-3} LiOH (Reddy & Linden, 2010; Posada *et al*., 2017). The LiOH has been reported to improve the cycle life and capacity of the positive electrode (Abadalla *et*

al., 2016; Chakkaravarthy *et al*., 1991; Posada *et al*., 2017). Other electrolyte additives that have been examined include Na_2S, K_2S, NaK tartrate, Na salt of EDTA, polyoxyethylene dodecyl ether, cyclohexylamine, and hydrazine sulphate (MacKenzie & Salkind, 1968; Malkhandi *et al*., 2012). At compositions in the range 1-5 wt. %, these additives reduce the rate of self-discharge and improve the utilization coefficient of the Fe active material (Chakkaravarthy *et al*., 1991).

Posada & Hall (2015) reported that electrolyte solutions constituting Na_2S and LiOH additives would significantly increase the specific capacity of the Fe-based electrode. Hang *et al*. (2014) reported that sulphide salts (such as K_2S), when utilised as an electrolyte additive, will significantly increment the specific capacity and suppress the hydrogen evolution at the Fe-based electrode. It has been evidently demonstrated that, by inhibiting hydrogen evolution, sulphide ions can suppress the electrolyte decomposition (Burke & Nugent, 1998; Hampson *et al*., 1974; Öjefors, 1976; Vijayamohanan *et al*., 1991).

2.6 Negative Electrode Material Development

2.6.1 Electrochemistry

The negative electrode in Ni-Fe batteries constitutes the Fe-based material blended with various additives. The Fe-based electrode has superlative theoretical specific ampere-hour capacity (~0.97 Ah g^{-1}) (Reddy & Linden, 2010). Chakkaravarthy *et al*. (1991) revealed that the Fe electrode is inexpensive and tolerant of physical and electrochemical abuse. In addition, Fe material is non-toxic and globally abundant. The electroactive material in the Fe electrode is a mixture of minute Fe and $Fe(OH)_2$. The charge/discharge reactions (Equations 2-7 & 2-8) occur at two distinct potentials (voltage levels) (Shukla *et al*., 1994). The second step is principally of no significance for battery operation (due to Reaction 2-11 & 2-12) and rarely occurs since Ni-Fe cells are designed with an excess of Fe-active material.

$$Fe + 2OH^- \underset{\text{Charge}}{\overset{\text{Discharge}}{\rightleftharpoons}} Fe(OH)_2 + 2e^- \qquad E^O = -0.877\ \text{V} \qquad [2\text{-}7]$$

$$Fe(OH)_2 + OH^- \underset{\text{Charge}}{\overset{\text{Discharge}}{\rightleftharpoons}} FeOOH + H_2O + e^- \qquad E^O = -0.560\ \text{V} \qquad [2\text{-}8]$$

Reaction Equation 2-7 is kinetically highly reversible as directed by the high electrode potential of -0.87 V, while the latter reaction Equation 2-8 has a lower potential (-0.56 V) consequently it does not accept charge readily (Chakkaravarthy *et al*., 1991). Studies on the electrochemical

kinetics behaviour of the Fe electrode material present supporting evidence in favour of a dissolution-precipitation mechanism (Armstrong & Baurhoo, 1972; Macdonald & Owen, 1973). The mechanism of the electrochemical reaction Equation 2-7 is generally considered to be multiphase or heterogeneous (involves both liquid and solid phases) (Lee *et al.*, 2018).

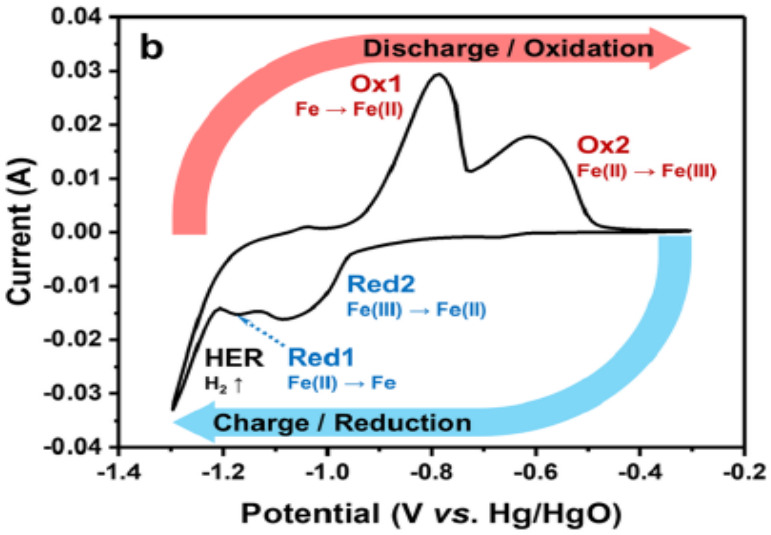

Figure 2-22: Voltammogram curve with the redox peaks assigned to corresponding reactions (Lee *et al.*, 2018)

X-ray Diffraction analysis of the different discharge stages and products of a pure Fe electrode unit and cyclic voltammetry studies on pure Fe electrodes in alkaline medium revealed that the oxidation of Fe proceeds in two main multiphase steps. The two multiphase steps comprise the formation of soluble ferrite ($HFeO_2^-$ and ferrate (FeO_2^-) intermediates (Hang *et al.*, 2006), i.e.

$$Fe+3OH^- \rightleftharpoons HFeO_2^- + H_2O + 2e^- \quad [2\text{-}9]$$

$$HFeO_2^- + H_2O \rightleftharpoons Fe(OH)_2 + (OH^-) \quad [2\text{-}10]$$

$$HFeO_2^- \rightleftharpoons FeO_2 + H^+ + e^- \quad [2\text{-}11]$$

$$2FeO_2^- + HFeO_2^- + H_2O \rightleftharpoons Fe_3O_4 + 3(OH^-) \quad [2\text{-}12]$$

The first oxidation step of Fe to metastable Fe(II), as a result of reaction 2-9 and 2-10, is of more practical significance for battery operation than the second step of Fe(I) to Fe(II) owing to reactions (2-11) and (2-12) (Lee *at al.*, 2018).

In-depth, the pure Fe electrode discharge reaction results first in the formation of a soluble ferrite ion which dissolves in the electrolyte solution. The ferrate ion anion then hydrolyzes (equation 2-10) to precipitate as $Fe(OH)_2$. Pourbaix *et al.* (1966) stated that the solubility of the ferrite ion is very low, and the resultant precipitated layer of ferrous hydroxide blocks the electroactive area and result in a low Fe utilisation coefficient of the electrode material. Furthermore, the low solubility of ferrite ion is temperature-dependent, and this correlation prompts the poor electrochemical performance of the electrode at sub-zero temperatures.

Although the solubility of ferrite ion anion in alkaline mediums is very low (only of the order of 10^{-1} M), this concentration is sufficient to sustain operational electrochemical conditions at the Fe electrode due to the minute state of the electroactive material (Latimer & Latimer, 1938:209). Similar to the Ni-positive electrode, the mechanism of the Fe electrode electrochemical reaction constitutes diffusion of protons through the $Fe(OH)_2$ and δ-FeOOH solid-state lattices, therefore there is a continuous disparity in the composition of the active material between δ-FeOOH and $Fe(OH)_2$. Since the conversion of $Fe(OH)_2$ to δ-FeOOH is a bulk process, the mechanism of the second discharge episode is essentially homogeneous in nature (Balasubramanian *et al.*, 1993).

The open-circuit potential of a typical charged pure Fe electrode is relatively always more negative than that of hydrogen electrode in the same alkaline medium (Chakkaravarthy *et al.*, 1991). Consequently, Fe is thermodynamically unstable and inevitably suffers passivation via local cells with hydrogen evolution as the conjugate reaction. The charge/discharge and hydrogen evolution reactions are outlined below.

$$Fe + 2OH^- \rightleftharpoons Fe(OH)_2 + 2e^- \qquad E_o = -0.88\ V \qquad [2\text{-}13]$$

and

$$2H_2O + 2e^- \rightleftharpoons H_2 + 2OH^- \qquad E_o = -0.83\ V \qquad [2\text{-}14]$$

Furthermore, the dissolved oxygen in the alkaline solution can be a conjugate reaction, i.e.:

$$O_2 + 2H_2O + 4e^- \rightarrow 4OH^- \qquad E_o = 0.4\ V \qquad [2\text{-}15]$$

Oxygen dissolution reaction (Equation 2-15) facilitates the passivation of Fe material. Attributable to the passivation reactions, Shukla *et al.* (1994) elaborated that the Fe electrodes in alkali mediums undergo a self-discharge (loss of charge) of about 1 to 3% of their nominal

capacity per day at room temperature. Hydrogen evolution (Equation 2-14) also occurs concurrently with the oxygen dissolution while charging the Fe electrodes in an alkaline solution (Reddy & Linden, 2010; Shukla *et al*., 2014). Reddy & Linden (2010) reported that the parasitic side reaction prompts a decrease in the charge acceptance of the electrode. The degree of utilization (or the coulombic efficiency) of Fe electrode, based on the 2-electron reaction Equation 2-13, varies from about 35% for commercially pure Fe electrodes to 65% for electrodes that comprise high-purity Fe (carbonyl Fe).

The potential of the $Fe/Fe(OH)_2$ couple (Equation 2-13) is slightly more negative than that of the hydrogen evolution potential in an alkaline medium. The hydrogen overpotential (overvoltage) is very low, as a result, there is a rapid evolution of hydrogen (Equation 2-14) during charging and slow hydrogen evolution on open circuit (Chakkaravarthy *et al*., 1991). Shukla *et al*. (1994) and Chakkaravarthy *et al*. (1991) attributed the low coulombic efficiency and the high self-discharge rate of the Ni-Fe battery to the parasitic hydrogen evolution side reaction.

The Fe-based electrode exhibits more influence on the overall electrochemical performance of the Ni-Fe battery (Manohar *et al*., 2012), therefore by altering the material composition, active particles structure and electrode production techniques, the overall electrochemical performance will subsequently improve (Huang *et al*., 2018; Reddy, 2010). The composite structure, morphology and production methods exhibit prominent influence on the electrochemical performance of the electrode (Chakkaravarthy *et al*., 1991; Huang *et al*. 2018; Reddy, 2010).

2.6.2 Composite Structure

In order to overcome the limitations faced by the Fe electrode, several additives are integrated into the negative Fe electrode during the modification process to formulate a composite structure. However, the additives composition must remain controlled (<60%) to impel Fe as prepotent active material since it possesses the desired superior electrochemical properties (principally its reversibility) (Comiso & Mengoli, 2007). Various additives have been integrated to decrease the rate of self-discharge, improve charge-retention and discharge rate capability, increase specific capacity, elongate cycle life and instil cycling stability. Additives are nominated on the basis of the modifications they effect on electrode material utilisation, electronic and

ionic conductivity, and hydrogen-evolution reaction overpotential (Vijayamohanan *et al*., 1990). These additives alter the structure and composition of the passivation film (generated during discharging) and thereby facilitate (or retard) the diffusion of OH^-, H^+ and Fe^{2+} ions. The anomaly present (instilled by additives) in the electrode material lattice structures regulates the mobility of these ions.

Linden (1984) reported that Cu and Hg can avert the evolution of hydrogen by increasing the hydrogen evolution reaction overpotential (Kao *et al*. (2011) synthesized Fe-Cu composite particles through electroless deposition method and then utilised the nanoparticles as anode material in an alkaline Ni-Fe battery. The research outcomes disclosed that the Fe-Cu composite material synthesized through electroless deposition is nanosized and Cu additive improves the rate of electron transfer between Fe particles by constructing an electro-conducting network. The nanosized Fe-Cu composite particles not only yield a high specific capacity of more than 600 mAh g^{-1}(Fe) but also exhibits an outstanding high discharge-rate capability at a current density of 3 A g^{-1}. Kao *et al*. (2011) also compared Fe-Cu composite nanoparticles with the Fe nanoparticles without copper and concluded that the Fe-Cu composite electrode maintains the initial nano-particle size during electrochemical cycling and therefore improves the cycling stability of the Fe electrode. Paulraj *et al*. (2017) elucidated that Fe core Fe_3C/Cu shell composite nanoparticles sample maintains a uniform smaller particle size (negligible particle agglomeration) during electrochemical cycling consequently delivering consistent higher specific capacities over time.

Carl-Hordman (1972) identified ferrous sulphide, sulphur, tellurium and selenium as singular additives (5-20 wt. %) that can be utilized to reduce the ionization potential, consequently reducing the electrode self-discharge. The composite material (Fe/Fe_2O_3/ & Sulphur) can be synthesized by reacting iron/iron oxide particles with sulphur of about 99% purity, in the form of elementary flowers of sulphur, colloidal sulphur, or as pure sulphur particles obtained by evaporation of a solution containing molecular sulphur. The fusion process does not involve a chemical reaction between the additive and Fe/Fe_2O_3 but a simpler physical process whereby the irregular surface of the Fe/Fe_2O_3 particles is fuse coated with the elemental sulphur, selenium or tellurium additive. The addition of minute $(NH_4)_2CO_2$ (1-3%) as a pore-forming agent in the Fe based composite electrode effectuate an increase the specific capacity (Caldas *et al*., 1998). Wan *et al*. (2012) stipulated that FeOx/Graphene hybrid materials as electrode

material successfully increase the traditionally nominal charge and discharging rates by approximately 1,000-fold while maintaining a high specific capacity of 120 $mAhg^{-1}$.

The effectiveness of the sulphide containing additives (e.g. FeS) additive has been attributed to multiple factors and mechanisms such as sulphide ion adsorption at the electrode-electrolyte interface with subsequent integration into the oxide lattice structure (as illustrated in Figure 2-23), modification of electrochemical reaction kinetics of the electrode, modification of the electrode texture and morphology, increase in the anodic current density, increase in the bulk electronic and ionic conductivity of the electrode, improving the rate of the $Fe/Fe(OH)_2$ reaction, increase in the solubility of Fe-based compounds and inhibition of the self-discharge process in the Fe electrode (Caldas *et al*., 1991; Hampson *et al*., 1974; Lee *et al*., 2018; Posada *et al*., 2016; Vijayamohanan *et al*., 1990; Vijayamohanan *et al*., 1991).

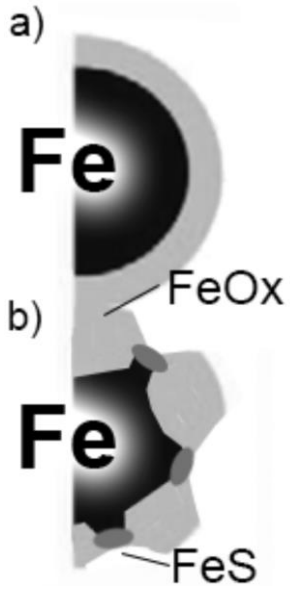

Figure 2-23: Illustration of (a) passivating FeOx layer and (b) a possible effect of FeS for the FeOx layer

$Ni(OH)_2$ and $Co(OH)_2$, which are isomorphic with $Fe(OH)_2$, serve to effect significant improvement in the electrochemical performance of the Fe electrode by reducing the Fe(I)/Fe(II) overpotential during both charge and discharge (Kononeuko, 1977). Kononeuko (1977) also noted that the use of aqueous solutions of polyvinyl alcohol with a dehydrating admixture as a binder ensures a reliable adhesion between the particles of the active mass and additives and the mesh/foam. Kao *et al*. (2011) synthesized Fe/C composite nanoparticles by reducing Fe^{2+}(in Fe salts) to elemental Fe on the surface of carbon-black particles and concluded that carbon-black particles, with a mean particle size of approximately 35-45 nm, act as the nucleation cores for Fe deposition and formulate a good electrical conductive

network, subsequently preventing the Fe particles from aggregating and instilling the ability to perform optimally at a high rate discharge (< C-2). Fe particle agglomeration is inhibited by the ability of electro-conductive Cu network to continuously reduce the Fe particles surface charge during electrochemical cycling.

Carbonyl Fe powder, microparticles consisting of spherical α-Fe particles (3–5 μm diameter), produced by the decomposition of Fe pentacarbonyl is a vital component of composite electrode formulation for inhibiting the hydrogen evolution reaction and achieving high charging efficiency (Manohar *et al*., 2012). The high electrochemical performance induction by carbonyl Fe is attributed to high surface area for electrochemical reactions (due to micro-sized particles) and deficiency of impurities, such as manganese, magnesium, calcium and phosphorous, that facilitate hydrogen evolution (Manohar *et al*., 2012; Sundar Rajan *et al*., 2015). Manohar *et al*. (2012) expounded that to further improve the charging efficiency and attain near-absolute suppression of hydrogen evolution, minute amounts of elemental bismuth (1-2%) are incorporated onto the surface of carbonyl Fe particles to inhibit the reaction kinetics of the parasitic hydrogen evolution reaction. The incorporation of bismuth, through in-situ electro-reduction of bismuth sulphide or oxide in the presence of carbonyl Fe, effectively suppresses hydrogen evolution and improves the discharge rate capability and utilization of the Fe active material. Elemental bismuth is ideally suited for this application as it is non-toxic and does not compromise the eco-friendliness of the Fe electrode material.

Detailed electrode composite structure development to date is presented in Table 2-2.

2.6.3 Nanostructure and Morphology

Electrode nanostructure modelling fosters ideal design criteria that boost the electrochemical performance of Fe-based electrodes. The developed design model should be based on fundamental processes that transpire in the Fe-based electrode, i.e., interphase and bulk mass-transfer, charge-transfer properties, and associated morphological changes (Vijayamohananet *et al*., 1990). Vijayamohananet *et al*. (1990) cited that it is vital to note that even macro-homogeneous design models, which are often applied satisfactorily, do not fully represent the complex dynamic behaviour of battery electrodes since several unrealistic assumptions, e.g., isotropic conductivity and one-dimensional electrical representation with uniform current distribution, are compiled and implemented (Vijayamohananet *et al*., 1990; Reddy & Linden,

2010). Nevertheless, such models have clarified various processes occuring in battery electrodes (Euler, 1973; Tiedemann & Newman, 1975).

The phase composition, crystallinity and morphology significantly influence the operational and electrochemical behaviour of Fe-based electrodes (Lee *et al*., 2018; Vijayamohananet *et al*., 1990). Alterations of active mass particle arrangement, structure and volume can influence the electrical and ionic conductivity, porosity of the electrode and mechanical stability of the electrode-substrate and electrode-electrolyte interfaces (Novakovskii *et al*., 1973). Vijayamohananet *et al*. (1990) clarified that the changes in lattice parameters should not be substantial to not alter the basic structure of electroactive phases. Furthermore, a change in the orientation of the various crystallites can also influence the electrochemical performance of the electrode. Therefore, it is vital to understand the interplay and interaction of various parameters of the solid-state. Uniformly dispersed particles of active mass are preferable as compared to agglomerated lumps. Impurities such as manganese, magnesium, calcium and phosphorous are believed to facilitate the hydrogen evolution, hence it is suggested to use high purity Fe as the active material (Manohar *et al*., 2012; Manohar *et al*., 2013; Sundar Rajan *et al*., 2015). A form of such a high purity Fe is carbonyl Fe, which is synthesized from iron pentacarbonyl ($Fe(CO)_5$).

Wells (1970) tabulated the crystal chemistry data for Fe, Fe_3O_4, $Fe(OH)_2$, and FeOOH (Table 2-1) which is useful to account for structural changes occurring during the electrochemical operation of Fe electrodes.

Table 2-1: Crystallography data for various iron oxides and hydroxides (Wells, 1970)

Crystal chemistry data for various oxides and hydroxides of iron[a]

Species	Descriptions
α-Fe	Body centered cubic structure
Fe_3O_4 (magnetite)	Inverse spinel structure: $(Fe_8^{2+})_t(Fe_8^{2+}Fe_8^{3+})_oO_{32}^{2-}$.
α-FeOOH (goethite)	Hexagonal close packing with OH^- hydrogen bonded to O^{2-} ions; Fe^{3+} in o-sites.
β-FeOOH	Body centered cubic structure akin to α-MnO_2; Fe^{3+} in o-sites; stable only in the presence of certain interstitial impurities.
γ-FeOOH (lepidocrocite)	Cubic close packed structure with Fe^{3+} in o-sites; hydrogen bonding between OH^- ions.
δ-FeOOH	Hexagonal close packed structure with random distribution of Fe^{3+} on o-sites as in $Fe(OH)_2$; 20% of Fe^{3+} in t-sites.
$Fe(OH)_2$	Hexagonal close packed structure with Fe^{2+} in o-sites as in $Mg(OH)_2$ lattice.

[a]o and t represent octahedral and tetrahedral sites, respectively.

During the discharge process of the Fe electrode, the b.c.c. Fe lattice transforms to $Fe(OH)_2$; the latter constitutes a hexagonal close-packed layered structure. The subsequent conversion of $Fe(OH)_2$ to FeOOH on further discharge is structurally feasible, as shown in Figure 2-24.

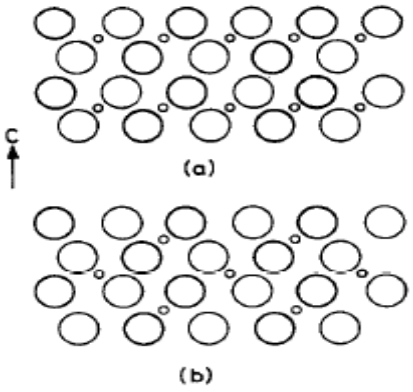

Figure 2-24: Comparison of structures of discharge products of alkaline iron electrode: (a) $Fe(OH)_2$; (b) δ-FeOOH (Wells, 1970)

The involved species during charge and discharge in strongly alkaline solution are consistently reported to be metallic Fe in alpha morphology (α-Fe) and Fe(II) hydroxide, respectively, which correspond to the Fe(0)/Fe(II) redox reaction described by equation Fe(II,III) oxide (Fe_3O_4) forms at an electrode potential of -0.912 V (reaction potential close to the electrode potential of the $Fe/Fe(OH)_2$ reaction at -0.880 V) (Lee *et al.*, 2018).

The formation of metastable $Fe(OH)_2$ is believed to be favoured over Fe_3O_4 due to the high kinetic reversibility of reaction Equation 2-13 (Geronov *et al.*, 1975). Fe_3O_4 formation is expected to occur only at high overpotentials or deep discharge states (Manohar *et al.*, 2013).

Figure 2-25 illustrates the unoxidized α -Fe homogeneous body centred cubic structure.

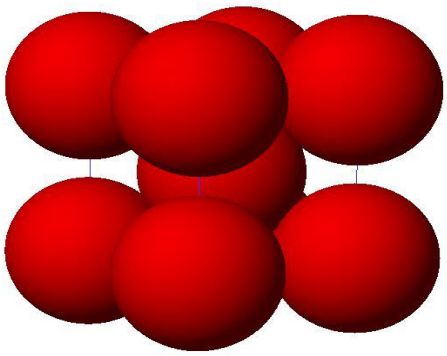

Figure 2-25: The homogeneous structure of α –Fe

$Fe(OH)_2$ does not exist in nature as a mineral due to its intrinsically unstable nature and no different polymorphs have yet been found (Cornell & Schwertmann, 2003). Cornell & Schwertmann (2003) elucidated that it has a similar crystal structure as β-$Ni(OH)_2$ but then the slabs are layered FeO_6 octahedra. Fe_3O_4 contains both Fe(II) and Fe(III) ions, exhibit an inverse spinel structure as shown in Figure 2-26b and has a thermodynamically more stable structure than $Fe(OH)_2$ due to its closer packing. Therefore, the hydrogen evolution can give rise to the dehydration of $Fe(OH)_2$ and formation of Fe_3O_4 under anaerobic conditions over time and can be described by the Schikkor reaction (Dibrov *et al.*, 1980):

$$3Fe(OH)_2 \rightarrow Fe_3O_4 + H_2 + 2H_2O \qquad [2\text{-}16]$$

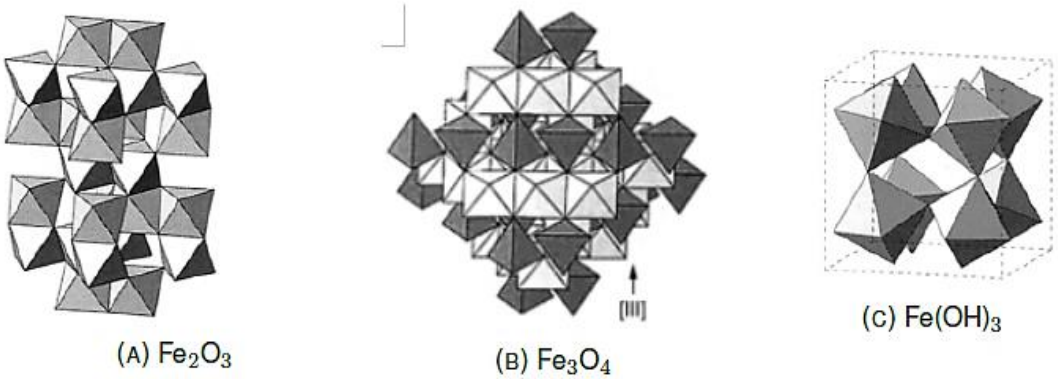

Figure 2-26: Structures of various iron oxide species (Cornell & Schwertmann, 2003)

An excess of hydroxide ions in the electrolyte remarkably inhibit the formation of Fe_3O_4 from $Fe(OH)_2$ (Zhang, 1994). Salkind *et al.* (1964) and Zhang (1994) implied that dissolved oxygen in the electrolyte also facilitates the formation of Fe_3O_4 from $Fe(OH)_2$. Zhang (1994) expounded that the hydrogen evolution effectuates an increased overpotential for the reaction of Fe_3O_4 to metallic Fe during charging leading to higher irreversibility of Fe_3O_4 to metallic Fe in the Fe(0)/Fe(II) potential window. Hence, the slow continuous formation of Fe_3O_4 by the occurrence of the Schikorr reaction and the parasitic side-reaction Equation 2-17 is believed to induce a long-term decay in discharge capacities of Fe-based electrodes (Manohar *et al.*, 2015).

In contrast to the predominant solid-state reaction of the oxidized species $Ni(OH)_2$ and NiOOH, the oxidation of metallic Fe is multiphase process constituting multiple soluble intermediates in an alkaline medium. Hang *et al.* (2006) revealed that the oxidation of Fe proceeds in two main stages, i.e. the formation of soluble ferrite ($HFeO_2^-$and ferrate (FeO_2^-) intermediates (Equation 2-9 to 2-12).

The accumulation of hydrogen at the electrode surface might also contribute to the overpotential increase during electrochemical cycling of the pure Fe electrode (Xie *et al.*, 2011). XRD analysis of a composite Fe electrode metraial in a charged state revealed that pure Fe metallic phase (α-Fe) remains dominant during stage I of electrochemical cycling (1^{st} -5^{th} cycle), signalling that the whole electrode active mass could be effectively reduced (i.e., high reversibility) after the oxidation in each cycle (Lee *et al.*, 2018). Lee *et al.* (2018) also noted that after the 50th cycle, nearly all Fe particles lose their initial spherical shape. Attributable to the insignificant further modification of electrode surface area expected during stage II of electrochemical cycling (5^{th} -50^{th} cycle), the maxima in specific capacity and coulombic efficiency remains stagnant until the 80th cycle while the electrode maintains the initial electrochemical behaviour.

However, SEM observations disclosed the formation of octahedra crystallic Fe particles during stage II, which can be regarded as monocrystalline morphology of the crystals with the $Fd\bar{3}m$ space group (Domingo, 1993). At the same time, XRD detected an initially weak but intensifying peak of either maghemite (γ-Fe_2O_3) or magnetite (Fe_3O_4) crystalline phase (Stagi *et al.*, 2014). Stagi *et al.* (2014) noted that γ-Fe_2O_3 crystals, a cation-deficient form of Fe_3O_4 crystals, constitute the same crystalline structure and analogous space group as those of Fe_3O_4 when

the cation vacant sites are randomly distributed over the octahedral interstitial sites (cubic inverse spinel belonging to *Fd3̄m* space group).

As confirmed by XRD analysis, during stage III of electrochemical cycling (50^{th}-80^{th} cycle), the aggregation of γ-Fe_2O_3 octahedra particles is deemed to block the surface of remaining Fe particle fragments while their gradual irreversible oxidation Fe to γ-Fe_2O_3 simultaneously takes place (Stagi *et al*., 2014). The resulting γ-Fe_2O_3 passivation layer insulates the Fe active particles, which can lead to an enormous lowering in reactivity and poor charge/discharge rate capability depending on the accessibility through the γ-Fe_2O_3 passivation layer (Linden & Reddy, 2010; Bernard & Lippert, 2015). Lee *et al*. (2018) deduced that the Fe passivation by less-reactive γ-Fe_2O_3 species impede the further diffusion of hydroxide anions to the remaining Fe particles present in the electrode and suppresses Fe(II)/Fe(III) oxidation reaction as well as the corresponding reduction reaction.

In addition, the passivating layer of $Fe(OH)_2$ is also electrically insulating (highly resistive) (Linen & Reddy, 2010). Linen & Reddy (2010) explained that the passivation increases the overpotential of the Fe/$Fe(OH)_2$ reaction at which the hydrogen evolution is believed to be favoured, leading to a decrease in coulombic efficiency as well. In contrast, hydrogen supersaturation is also suggested to have a beneficial effect. The fast crystallization ensures the reformation of a high active surface area (>100m^2/g), framing the long cycle life capability of Fe-based electrodes. Shukla & Hariprakash (2005) highlighted that the ionic polarization solely cannot fully limit the capacity as the electrolyte is expected to still be able to penetrate the porous matrix.

Scheme 1 (Fig. 2.11) summarizes the structural and morphological changes in a typical Fe electrode over its respective electrochemical cycle life upon deep cycling (Lee *et al.,* 2018). The depiction helps to apprehend the multistage electrochemical activity in terms of the structural and morphological changes as mentioned above. Although multiple episodes simultaneously during each stage of electrochemical cycling, it can be denoted by its main distinctive activity or phenomenon: Fe particle fragmentation (Stage I: 1-5^{th} cycle), initiated γ-Fe_2O_3 formation (stage II: 5-50^{th} cycle), accelerated γ-Fe_2O_3 accumulation (stage III; 50-80^{th} cycles), and passivation by γ-Fe_2O_3 (stage IV: >80 cycles).

A systematic study by Lee *et al*. (2018) aimed at correlating the evolution of the electrochemical behaviour of microscale Fe upon deep cycling in alkaline medium with the changes in its

morphology and crystalline phase and structure pointed out that the Fe electrode undergoes four stages during electrochemical (charge−discharge) cycling marked by the energy capacity and efficiency changes. The four stages include Fe particle development (stage I), retention (stage II), decay (stage III), and failure (stage IV). Through extensive physical analyses using Raman spectroscopy, SEM and XRD, it was noted that each electrochemical cycling stage is associated with very specific changes in the phase composition and structure together with the morphology the Fe electrode. From the initial cycles, it was observed that Fe particle disintegration (fragmentation) was prompted by the surface-limited electrochemical (charge-discharge) reactions.

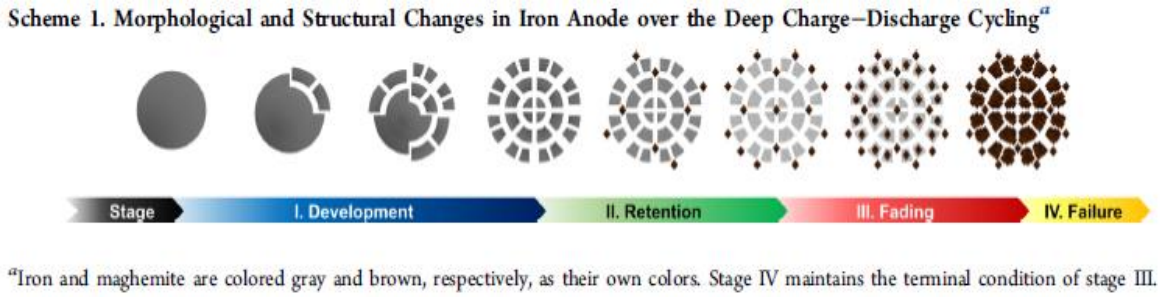

Figure 2-27: Morphological and structural changes in Fe electrode over the deep charge−discharge cycling (Lee *et al*., 2018)

The gradual expansion of the surface electroactive area effectuates capacity increase, which reaches maxima at the end of stage I. The maxima capacity stagnates during stage II while the initiated formation of γ-Fe_2O_3 octahedral monocrystalline particles is observed. The aggregation and accumulation of γ-Fe_2O_3 prompt rapid capacity decay in stage III and eventual failure in stage IV. Electrochemical tests confirmed the low electrochemical activity of γ-Fe_2O_3 in alkaline mediums. In general, the electrochemical reactions on the Fe anode are composed of heterogeneous multistep redox processes, constituting dissolution and precipitation of evolving phases as well as the diffusion of dissolved intermediates. Results presented by Lee *et al*. (2018) suggested that in order to maximize the utilization of Fe active material (maximise capacity) while minimizing capacity decay, there is need to avert the irreversible nucleation and growth of the γ-Fe_2O_3 phase.

2.6.4 Electrode Production Techniques

Three different types of Ni positive electrode are widely employed i.e. (i) sintered, (ii) pressed and (iii) tubular or pocket.

2.6.4.1 Pocket or Tubular Electrodes

The powdery mixture (Fe and Fe_2O_3) is blended with additives (Cu, FeS, HgO, etc) and deposited into tubes or pockets constructed from perforated-steel sheet plated with Ni. The tubes or pockets are mounted over a suitable Ni-plated steel plate to form the negative electrode (Öjefors & Carlsson, 1978). The tubular electrode was first introduced by Edison in 1900 and is still mass-produced in France and West Germany, whereas the pocket plate electrodes are mostly mass-produced in Russia (Chakkaravarthy *et al.*, 1991). The pocket plate design is depicted in Figure 2-28 below.

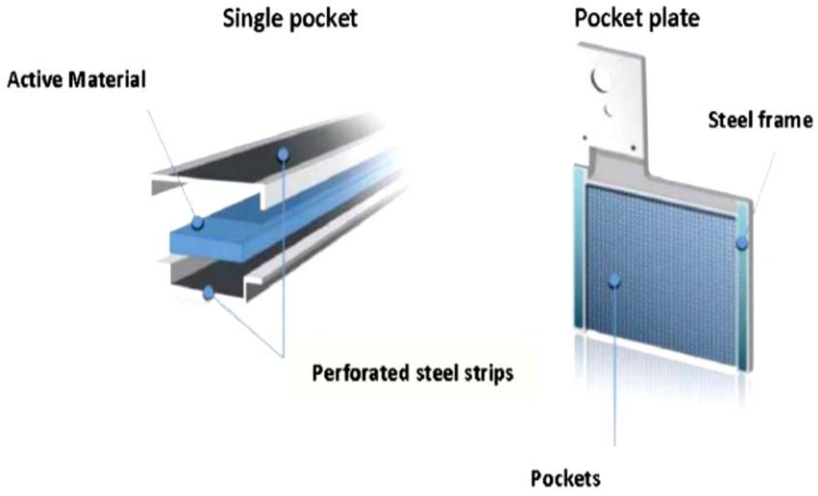

Figure 2-28: Pocket plate design (Bernard & Lippet, 2015)

Linden and Reddy (2010) noted that tubular design electrodes are physically almost indestructible and simple to construct. However, the design is associated with high self-discharge, low power density, lower energy density than the competitive designs such as pocket plate and sintering.

2.6.4.2 Sintered Electrodes

Sintered electrodes are produced by a thermal deposition process in which loose Fe powder particles are transmuted into a thin coherent porous body (60-70% porosity) by heating in an inert atmosphere just below the melting point of pure Fe (970-1070K). (Chakkaravarthy *et al.*, 1991). Chakkaravarthy *et al.* (1991) stated that the inert atmosphere can be either hydrogen, argon, nitrogen or a mixture of either of the gases. In sintered Fe-based composite electrodes,

the matrix serves both as the active material and the current-conducting mesh. However, if additives are integrated to formulate a composite mixture, various substrates (current conductor) may be utilised, these include Ni mesh or Ni-plated mild and stainless steel mesh, perforated Ni foil or Ni-plated, perforated mild and stainless steel foil, Ni-fibre mat or Ni-plated steel-fibre mat (Chakkaravarthy *et al*., 1991).

Loose sintering is also utilised to synthesize the Fe-based composite electrode (Edward, 1977). Edward (1977) expounded that in this process, electrolytic Fe powder or carbonyl Fe powder is uniformly spread over a Ni-plated steel mesh that is placed in a circular or rectangular cavity of a graphite plate. The size and thickness of the Fe electrode plate are determined by dimensions of the cavity. The sintered Fe electrode plate possesses porosity of approximately 55±5%. The electrode plate is further activated by integrating suitable additives. However, this method of electrode production, which utilise high-temperature treatment in an inert gas atmosphere, entails much higher production costs and are therefore a less attractive option (Manohar *et al*., 2012).

2.6.4.3 Paste Type Electrodes

The active material with sufficient additives is blended with an aqueous polymeric binder such as PTFE) or PE. The resulting mixture is pasted on a porous Ni-foam sheet to produce a plate of the desired thickness. The wet electrode is vacuum dried for 24-48 hours (Huang & Chou, 2007; Kao *et al*., 2011). This design of flat paste type negative electrodes exhibits better electrochemical performance than its counterparts (pocket type and sintered type electrodes) in terms of specific energy, volumetric capacity, ampere-hour capacity and Fe active material (Caldas *et al*., 1998). In addition, "paste plate" type electrode production process is a simple technique that entails much lower production costs compared to sintered electrodes and is, therefore, a more attractive option compared to the other competing techniques (Manohar *et al*., 2012; Kao & Chou, 2010).

2.6.4.4 Pressed or Roll Compacted Electrodes

The Fe active material blended with ideal additive(s) and a polymeric binder such as PE or PTFE. The resulting composite mixture is hot pressed on a suitable electro-conducting mesh such as Ni-mesh or Ni-plated steel mesh or rolled through a hot rolling mill together with an electro-

conducting mesh to produce an electrode plate of the desired dimensions. Sometimes, a pore-former such as $NaC_7H_5O_2$, minute NaCl or $(NH_4)_2CO_2$ particles is utilised during the roll compaction process (Huang & Chou, 2007). Boiling water is employed to leach out the pore-forming agent to generate sufficient porosity in the electrode plate. This design of flat negative electrodes exhibits better electrochemical performance than the sintered and pocket type electrodes in terms of specific energy, volumetric capacity, ampere-hour capacity and Fe active material (Caldas *et al*., 1998). In addition, "pressed plate" type electrode fabrication entails much lower production costs and exhibit good charge characteristics and durability under optimal current drains (C/5-10), the design is, therefore, more attractive compared to the other competing designs (Manohar *et al*., 2012).

Comparative analysis table below (Table 2-2) gives an insight into how researchers over the years have developed the Fe-based electrode.

Table 2-2: Comparative analysis table on the development of the negative electrode over the years

Composite Structure (% w/w)	Substrate Type	Manufacturing Technique	Performance Characteristics				Ref
			Ch/DCh Efficiency (%)	Specific Capacity (Ah/kg)	DCh rate	Capacity retention (%/day)	
93% $Fe_{2.8}O_4Cu_{0.2}$, 5% CB, 2% PTFE	Nickel Foam	Pasting	85	250	C/1	NS	Huang *et al.* (2018)
85% NanoFe-Fe_3C-Cu, 5% Bi_2S_3, 10% PTFE	Nickel Mesh	Pressing or RC	80	367	C/4	NS	Poulraj *et al.* (2017)
85% Fe, 10% $(NH_4)_2CO_3$	Nickel Mesh	Sintering	97	200	C/1	98% (After 3500 cycles at C/1)	Yang *et al.* (2017)
72 % Fe, 18% Cu, 10% PTFE	Nickel Foam	Pasting	85	200	C/4	NS	Posada & Hall (2015)
85.5% (3-5µm) Fe, 4.5 % Bi_2S_3, 10% PTFE	Nickel Mesh	Pressing or RC	80	280	C/5	NS	Narayan *et al.* (2015)
76.5 % (3-5µm). 4.5% FeS, 10% PTFE	Nickel Mesh	Pressing or RC	85	250	C/5	NS	Narayan *et al.* (2015)
80 (3-5µm)%. 10% Bi_2O_3. 10% PTFE	Nickel Mesh	Pressing or RC	78	200	C/5	NS	Narayan *et al.* (2015)
100% Fe_30_4	GF/CNT	Pocketing	80	80	C/5	NS	Liu *et al.* (2014)
92% Fe_3O_4, 5% Bi_2O_3, 3% HPMC	Graphene Sheets	Film Growing	NS	552	C/2.8	91% (After 100 cycles at 200mA/g)	Jiang *et al.* (2014)

45% (<4500nm)Fe, 2% FeS, 43% CB, 10% PTFE	T-CNF (50 nm)	Pressing or RC	NS	80	C/5	NS	Hang *et al.* (2014)
85% FeS, 5% Graphite,10% PE	Nickel Mesh	Pressing or RC	77		C/5	NS	Van Dijk (2012)
76 %(3-5µm) Fe, 5% Bi_2S_3, 9% PE, 10% K_2CO_3	Nickel Mesh	Pressing or RC	80	300	C/20	NS	Manohar *et al.* (2012)
67% Fe, 2% Na_2S, 22% CB, 9% PTFE	Nickel Foam	Pasting	80	600	C/5	80% (After 100 cycles at 150 mA/g)	Kao & Chou (2010)
67% Fe, 22% Cu,2% Na_2S, 9% PTFE	Nickel Foam	Pasting	65	800	C/4	94% (After 40 cycles at 200mA/g)	Kao *et al.* (2011)
78% Fe. 2% FeS, 10% $(NH_4)2CO_3$	Nickel Mesh	Pressing or RC	NS	300	C/6	NS	Caldas *et al.* (1998)
88% Fe, 2% FeS, 10% PTFE	Nickel Mesh	Pressing or RC	NS	100	C/5	NS	Caldas *et al.* (1998)
100% Fe	Nickel Mesh	Sintering	75	24	C/5	NS	Periasamy *et al.* (1996)

NS=Not Specified in Article, RC = Roll compacting

2.7 Battery/Cell Design

Aqueous batteries are available in winded cylindrical or rectangular cells. The cells can be stacked in series or parallel (bipolar), depending on the desired energy capacity. To deal with the depletion of the electrolyte, non-sealed valve-regulated cells exist to refill the electrolyte (Bernard & Lippert., 2015). Cells can be sealed when no build-up of gas occurs within the cell (ideal 100% coulombic efficiency) or hydrogen and oxygen adsorbing additives are applied.

2.7.1 Cylindrical Batteries/Cells

Sturkenboom (2016) stated that for the cylindrical battery design, the electrodes are coiled together with a separator in a swiss roll similar format. The roll is then inserted in a cylindrical Ni-plated steel can-shaped case with the top cover welded to the positive electrode and the negative electrode connected to the can. The electrolyte is poured into the can by which the electrolyte level equals that of the electrodes and separator. The top is cramped by which it can be ripped off by internal overpressure due to overcharge/discharge. However, this design is not widely implemented due to its complex design entailed with high costs.

2.7.2 Prismatic Batteries/Cells

Vu *et al*. (2018) stated that for the prismatic batteries/cells design, the electrodes are cut into rectangular, triangular or circular plates of desired dimensions and assembled into cells by interspacing the negative and positive electrode plates. The separator is inserted between the electrodes to facilitate the mobility of ions concurrently avoiding short-circuiting. The battery/cell case may be constructed from Ni-plated steel sheet or alkaline resistant polycarbonate or polycarbonate material. The steel battery/cell cases may be electrically insulated with rubber or plastic coatings. In moulded nylon battery cases the cells can be assembled in batteries or mounted in wooden traps. The electrode production processes are designed to produce high purity materials with special particle characteristics for enhanced electrochemical performance (Linden & Reddy, 2010; Vu *et al*., 2018). Vu *et al*. (2018) iterated that prismatic design is the most common design due to its simple yet rugged design synonymous with outstanding electrochemical performance. The construction of a prismatic Ni-Fe cell is depicted in Figure 2-29.

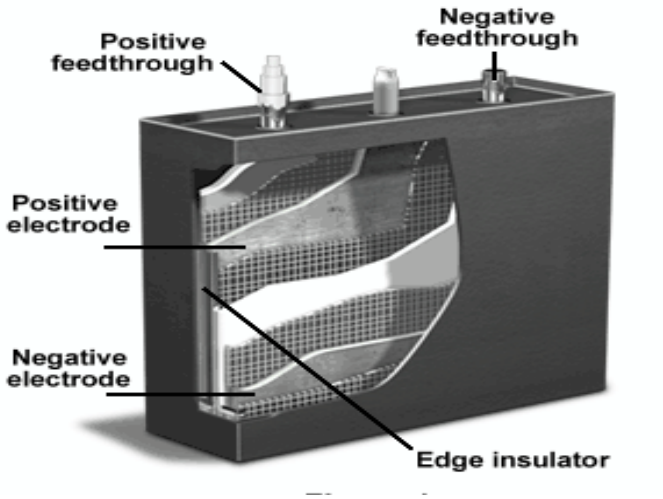

Figure 2-29: Simplified construction 3D depiction of a prismatic nickel-iron cell (Linden & Reddy, 2002)

2.7.3 Bipolar Batteries/Cells

The bipolar Ni-Fe battery technology pursues an innovative combination of optimised battery components and design in conjunction with the application of novel mass-production techniques (Fraunhofer UMSICHT, 2019). Fraunhofer UMSICHT (2019) stipulated that by employing the bipolar battery design, it is possible to save over 75% of conventional battery materials such as electrolyte, insulating material, cables. The replacement of Ni-mesh using corrosion-free electro-conductive polymer film (bipolar plate) bipolar plate offers a more cost-effective alternative solution. However, this technology is still in the development phase therefore the literature on the design is not widely available. One of the first bipolar Ni-Fe prototypes is reported in this work. The schematic structure of a bipolar Ni-Fe battery prototype is depicted in Figure 2-30 below.

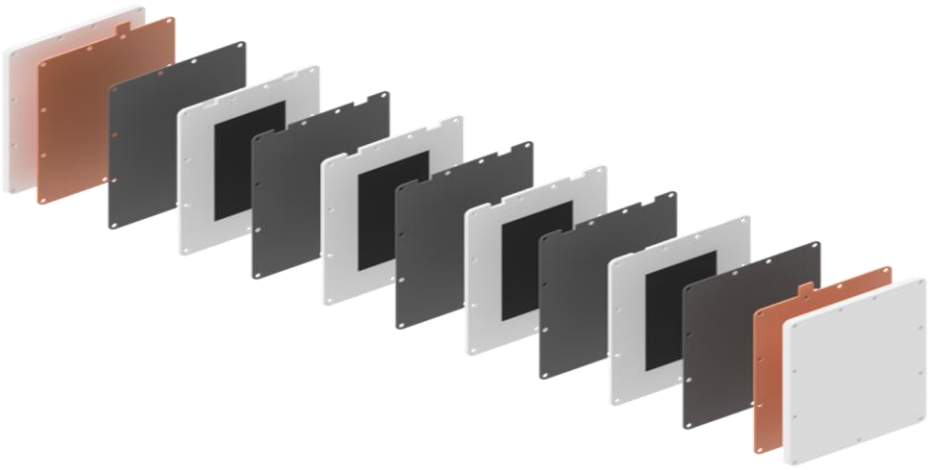

Figure 2-30: Schematic structure of a bipolar nickel-iron battery (Fraunhofer UMSICHT, 2019)

2.8 Deductions from the Literature Review

In summation, the reaction mechanisms transpiring at the Fe-based electrode incur some apparent drawbacks that affect the overall electrochemical performance of the Ni-Fe battery. Weaknesses within existing Ni-Fe system include:

- The inevitability to overcharge due to overpotential of the Fe/FeOx reactions resulting from the hydrogen evolution causes (i) low efficiencies (ii) poor energy densities and (iii) toxic hydrogen gas production (Reddy & Linden, 2010). The evolution of hydrogen gas from the electrolyte leads to the depletion of the electrolyte and as a result, the cell cannot be sealed. Moreover, the occurrence of the hydrogen evolution reaction causes the electrode to be intrinsically unstable leading to self-discharge (EPRI-DOE, 2003; Reddy & Linden, 2010).
- Having a dissolution/precipitation mechanism with soluble intermediates involved results in an (i) increased temperature-dependent performance and (ii) passivation of the electrode by various FeOx species at high charge density capacities (Huang *et al.*, 2018). The passivation ultimately results in even more limited power densities and efficiencies (Huang *et al.*, 2018; Reddy & Linden, 2010).
- Involved species in the charge/discharge process have the tendency to spontaneously transform into more stable but less reversible species over time, which also lead to a decrease in cycle life, efficiencies and energy densities (Huang *et al.*, 2018).

In an attempt to address the abovementioned drawbacks, various solutions are to be implemented for this project.

- **Composite Electrode**

An ideal electrode structure maintains a high reactivity at the electrode/electrolyte interface over a long cycling lifetime, which does not lead to conduction limitations of the electrons to the current collector (Reddy & Linden, 2010). Modifications of the active material should be minimal to preserve mechanical and chemical integrity of the electrode. Composite electrodes constitute additives that enhance the electrochemical performance of the electrode.

It is conventionally preferred to uniformly disperse the micro-particles of Fe active material over the current collector. The micro-particles have a high active surface area, while a uniform dispersion increases the electronic conductivity and averts rapid passivation (Shukla & Hariprakash, 2009). Cu nanoparticles, when incorporated into the electrode, inhibit hydrogen evolution, improve electron transfer between particles, increase specific capacity and invoke cycling stability. FeS additive increase ionic conductivity, inhibit hydrogen gas evolution and to reduce the ionisation potential. The addition of $(NH_4)CO_2$ as a pore-forming agent in the Fe based composite electrode effectuate an increase the capacity (Caldas *et al*., 1998). In conclusion, the integration of Cu, FeS and $(NH_4)_3CO_2$ into Fe-based electrode at optimal concentrations should yield improved electrochemical performance.

- **Conductive Current Collector**

The current collector is usually a metallic Ni mesh or foam. Metallic Ni mesh is preferred over other metals such as Fe or stainless steel because of its higher durability in alkaline solutions (Abdalla *et al*., 2016). Square size 1mm aperture size Ni mesh was employed due to its minimal resistance to electrons mobility. The substrate represents the physical backbone of the electrode and plays a key role in the electro-conductivity and mechanical stability of the electrode. Ni-mesh was employed for electrodes utilised in prismatic test cells. Low-cost bipolar graphite plate exhibit similar electroconductivity properties to Ni-mesh (Fraunhofer, 2019). Bipolar graphite plate was utilised in the construction of a bipolar Ni-Fe battery prototype.

- **Binder**

To adhere to the active material to the current collector a polymer binder can be necessary to be applied, depending on the production technique (Poulraj *et al*., 2017). The polymer binder is selected for its thermochemical resistance and adhesive properties. Most thermochemical resistant polymer binders have the disadvantage to be electronically insulating and hydrophobic. Low-density Coathelyne (CA) binder was employed as the adhesive material as it possesses abovementioned properties and in addition its stability in alkaline systems.

- **Conductive Additive**

The active material can have insulating intermediates involved during the charge/discharge process, such as $Fe(OH)_2$. Due to insulating intermediates and/or the insulating property of the polymer applied it can be necessary to blend the active material with conductive nanoparticles, such as amorphous conductive black carbon or graphite to increase the electronic conductivity (Huang *et al*., 2018; Van Dijk, 2017). For hot pressed -based electrodes, the highest discharge capacities were achieved by using graphite as a conductive additive (Kao & Chou, 2010). For this work, graphite was employed as a conductive additive.

- **Electrode Production Method**

The low-cost hot-pressing technique was employed for electrode production. Chakkaravarthy *et al*. (1991) and Caldas *et al*. (1998) highlighted that pressed type electrodes incur low-cost of production and exhibit good charge characteristics and durability under optimal current drains (C/5-10).

- **Cell/Battery Design**

The prismatic design is simple in construction thus ideal for the construction of test cells. The bipolar design was employed to construct the Ni-Fe prototype. The design utilises a low cost and corrosion-free conductive polymer film (bipolar plate), by employing the design it is possible to save over 75% of conventional battery materials such as insulating material and cables (Fraunhofer, 2019).

It is believed by encompassing the abovementioned proposed solutions, a low cost and high performing battery that can be used in energy storage systems can be constructed.

Chapter 3: Experimental Methodology

3.1 Overview

This chapter describes the syntheses process of the composite Fe-based electrodes (Section 3.2) and the material and electrochemical characterization techniques (Section 3.3 and 3.4) employed to assess their respective electrochemical performance.

3.2 Electrode Modification

To ensure consistency in the in-house synthesized electrodes, the process was well designed and controlled, operating parameters temperature, pressure, time were optimally stipulated, and equipment was calibrated before research work commenced.

3.2.1 Material and Chemicals

Table 3-1 provides a list of materials and chemicals (including their details) that were employed during the course of this research.

Table 3-1: Materials and chemicals utilised during the course of this research

Material/Chemical	Supplier	Comp.	Details
Iron (Fe)	Hoganas	99.9%	Particle size 0.1-0.2µm
Iron Sulphide (FeS)	Sigma Aldrich	99.9%	
Copper Sulphate ($CuSO_4$) Pentahydrate ($CuSO_4.5H_2O$)	ACE	99.9%	
Graphite	Alfa Aesar	99.9%	Universal grade, -200 mesh
Ammonium Carbonate $(NH_4)_2CO_2$	ACE	60% min	Impurities include Fe, Pb, SO_4^{2-}, As
Coathylene HA1592	AXALTA	99.9%	MP=105^{O}C, (LDPE)

Nickel Mesh	Q-Lite Industrial Ltd.	99.9%	1mm aperture size, 1mm thickness
Sodium Borohydride ($NaBH_4$)	Fluka Chemicals Corp.	99.9%	
Graphite Bipolar Plate	Fraunhofer Umsicht	99.9%	

3.2.2 Equipment

During the experiments, various machines were utilised to produce the Fe-based composite electrode.

3.2.2.1 Hydraulic Press

A custom-designed hydraulic press (HyJack, Cape Town) was used to compact the electrode materials to form mechanically stable electrodes. The machine has flexible control features which makes it easy to manipulate pressure and temperature during the pressing. The hydraulic system can generate pressure up to 80 MPa, which constitutes a force of 40 MN Both pressure plates are equipped with 3 heating rods each. A Gefran 600 digital thermal controller is employed to easily control and regulate the temperature. The maximum attainable temperature is 280 °C. The press can be operated in manual and automatic modes. The hydraulic press is depicted in Figure 3-1a with a close-up of the controller box in Figure 3-1b.

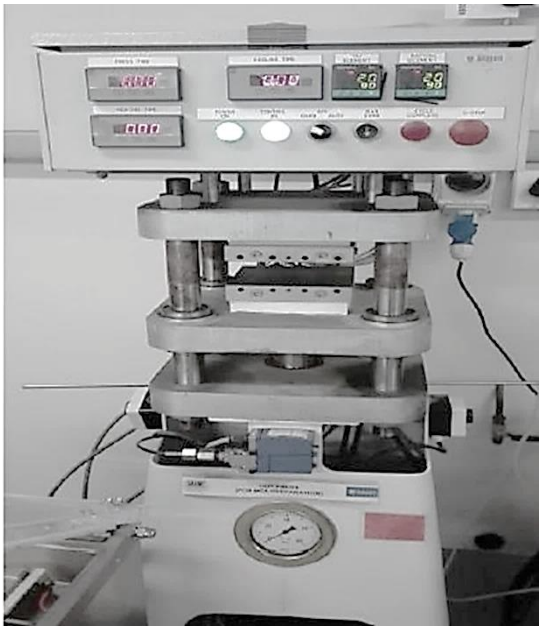

a) **b)**

Figure 3-1: a) Hydraulic press and b) thermal controller box

3.2.2.2 Vacuum Oven

The vacuum oven (VWR, Germany), depicted in Figure 3-5, was employed to facilitate the drying of $FeCu_X$ material after centrifugation and filtration during $FeCu_X$ material synthesis.

Figure 3-2: The vacuum oven employed during Fe-Cu material synthesis

3.2.2.3 Press Moulds

Three press dies were designed and manufactured by WAKE Engineering, SA. The schematic drawings of these dies are provided in Figure 3-3. A photo of the produced dies is included in Figure 3-4.

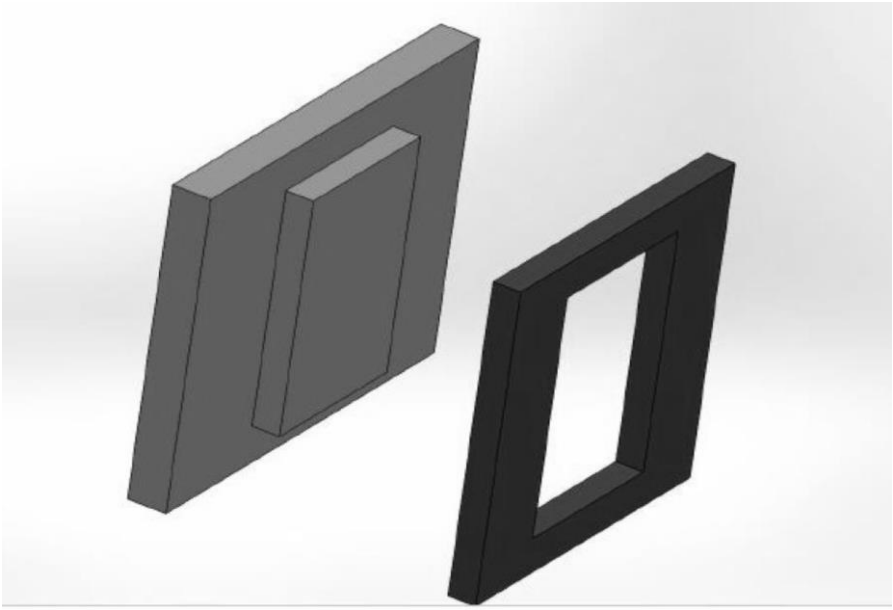

Figure 3-3: Schematic diagram for a press mould

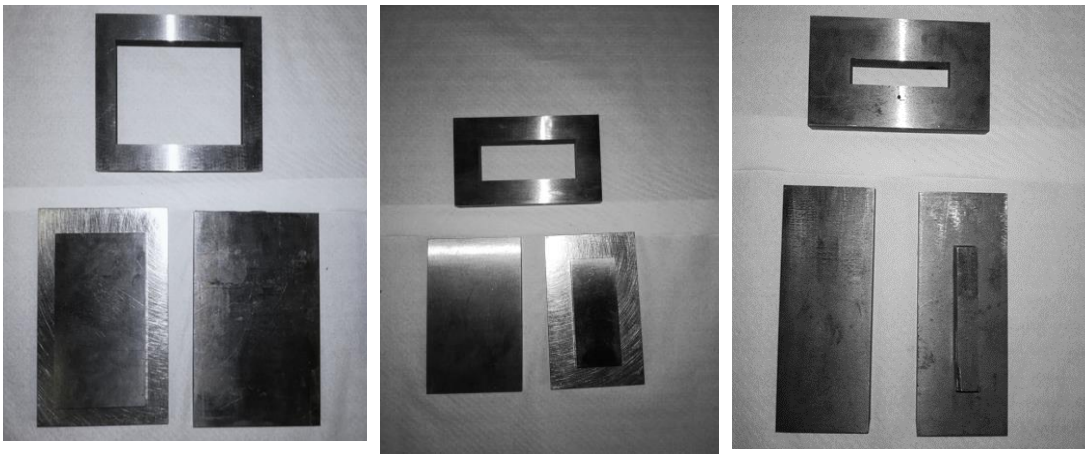

a) **b)** **c)**

Figure 3-4: Different sizes of electrode molds (a)-for cell electrode production (90 x 60 mm), b) for cell electrode production (30 x 60 mm)and c) for CV electrode production (10 x 60 mm))

3.2.2.4 Overhead Mixer

The overhead mixer (VWR, Germany), depicted in Figure 3-5, was employed to facilitate dissolution of materials in solvents and induce homogeneity in solutions.

Figure 3-5: Overhead mixer

3.2.2.5 Other Equipment

Other small equipment employed during the course of the research include;

Table 3-2: Small equipment compilation

Equipment / Item	Make / Model	Details
Spatulas	Flat and spoon spatulas, Lasec Co.	Stainless steel
Stirring Rods	Stainless steel rods, Lasec Co.	15 mm length
Mixing Vessels	Glass vessels, Lasec Co.	1L, 2L
Water Purification System	PURELAB® Prima, Elga Veola Co.	

3.2.3 Electrode Production

3.2.3.1 Methodology Overview

The overall methodology adopted in this study is depicted in Figure 3-6.

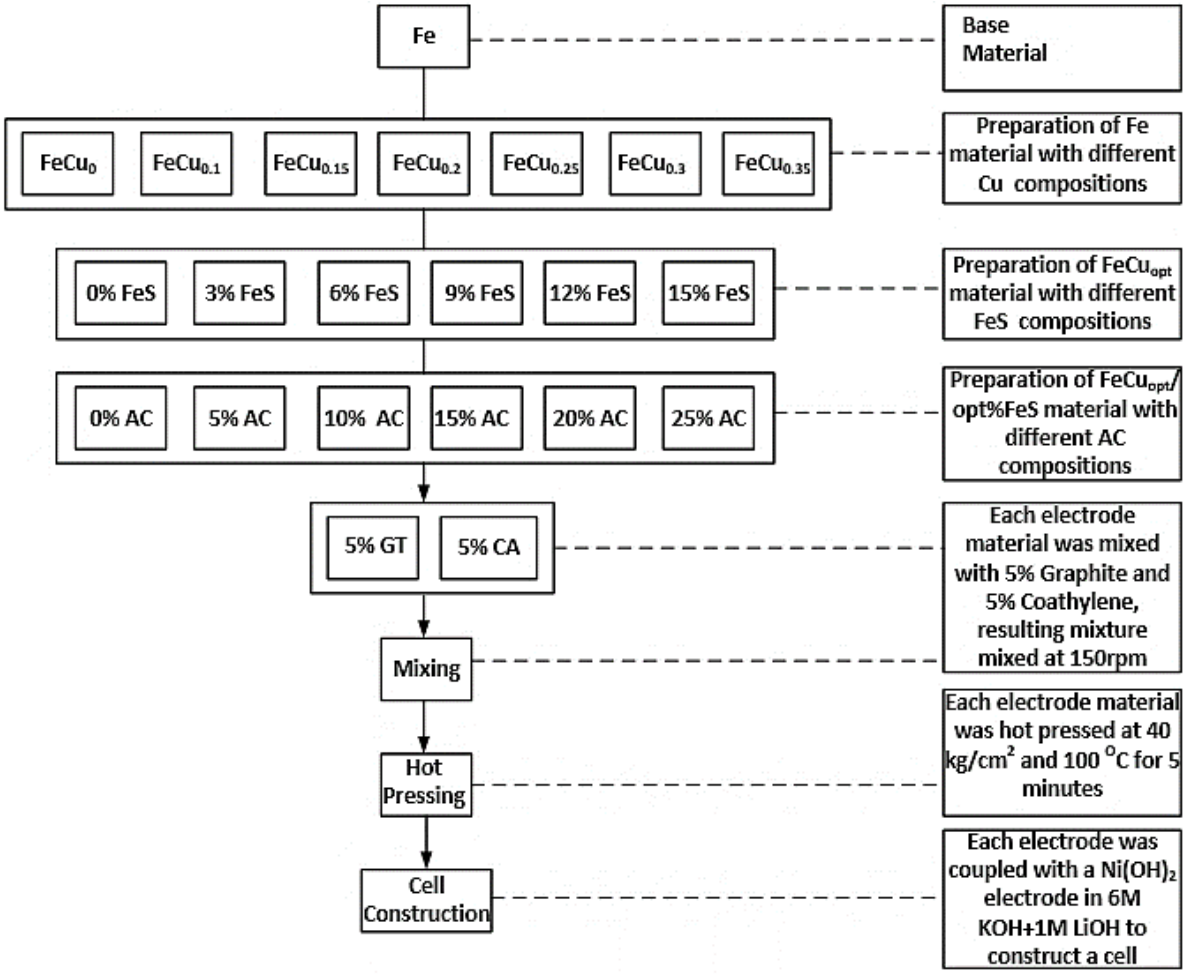

Figure 3-6: Schematic representation of the experimental methodology adopted for this study

The methodology constitutes; the synthesis of $FeCu_x$ composite particles, the mixing $FeCu_x$ material with FeS, C, AC and CA to formulate the electrode composite material mix followed by the compaction of the electrode mixture onto an electroconductive Ni mesh. The electrode produced is utilised as the anode in constructing the test cell. Each step will be discussed in the subsequent sections.

3.2.3.2 Synthesis of $FeCu_X$ Composite Material

The reagents employed (stipulated in Section 3.2.1) were purchased and used without further purification. The $FeCu_x$ composite electrode materials were synthesized through autocatalytic and electroless deposition, followed washing with deionized water and vacuum drying at room temperature to acquire the precursor materials $FeCu_x$ (x=0, 0.1, 0.15, 0.2, 0.25, 0.3, 0.35). The synthesis process of the $FeCu_X$/FeS/C microparticles is schematically presented in Figure 3-7. The typical process employed to synthesize $FeCu_{0.25}$ composite was executed as follows:

16.8 g (0.3 mol) of Fe powder (150±60 nm) was dispersed into 400 ml deionized water. The dispersion was stirred on an overhead stirrer at 100rpm (0.55: Impeller to vessel diameter ratio) for 10 minutes. 18.75 g of $CuSO_4.5H_2O$ (0.075 mol) was dissolved in 200 ml deionized water by stirring at 100 rpm impeller speed for 2 mins on an overhead mixer at room temperature to produce the 0.375 M $CuSO_4$ solution. A 0.3 M $NaBH_4$ solution was prepared by adding 9.4575 g of $NaBH_4$ into 850 ml deionized water and stirred at 100 rpm for 2 minutes on an overhead stirrer.

The 0.375 M $CuSO_4$ solution was added dropwise to the Fe dispersion under continuous stirring at 100 rpm. When the solution turned from blue to green, dropwise addition of the aqueous 0.3 M $NaBH_4$ solution commenced under continuous stirring (at 100 rpm). Shortly after all the $NaBH_4$ was added, the formation of gas bubbles was visible. The absence of gas bubbles production combined with a complete solution colour change from green to colourless indicated the successful reduction of residual Fe^{2+} ions; the composition of the composite was noted as $FeCu_{0.25}$. Correspondingly, the sample $FeCu_x$ (x=0.2) was also prepared by altering the Fe/Cu mole ratio to 5 to suit the molecular denotation $FeCu_{0.2}$. After 10 minutes of continuous stirring (at 100 rpm) the mixture was allowed to cool down. The reaction products were separated by means of centrifugation, washed three times with deionized water, and finally dried in a vacuum oven at room temperature for 3 days.

3.2.3.3 Synthesis of the Composite Mix

Synthesized $FeCu_{x=opt}$ material was mixed with a varied amount of FeS for the second set of electrodes. $FeCu_{x=opt}$ mixed with optimum amount of FeS was mixed with varied amount of $(NH_3)_2CO_3$ for the third set of electrodes. All electrode formulations constituted 5% Graphite,

and 5% of PE to form the composite mixture. Figure 3-7 illustrates the synthesis process of the $FeCu_x$/FeS/C particulates.

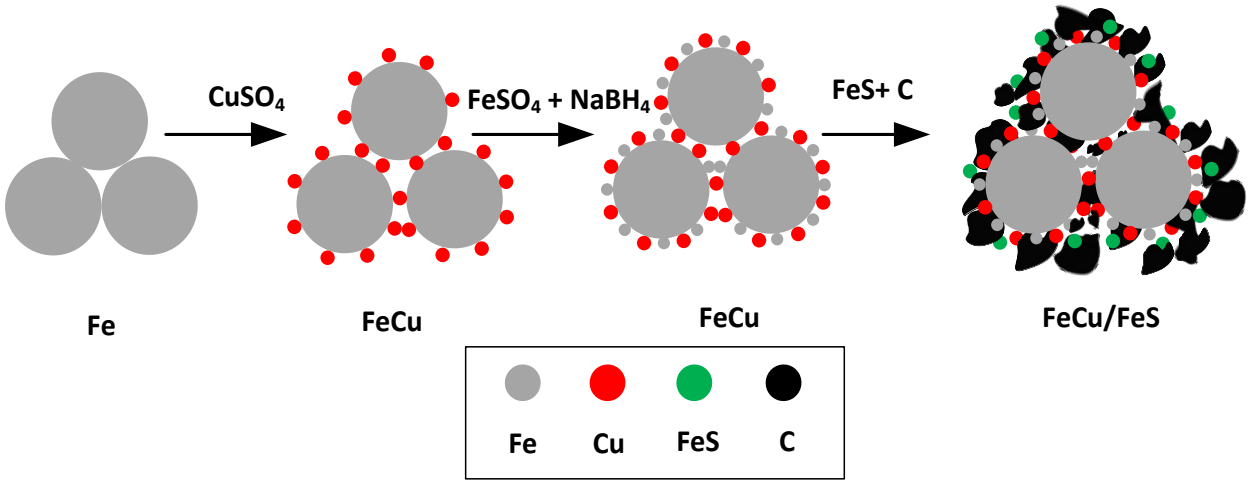

Figure 3-7: Schematic illustration of the synthesis process of the $FeCu_x$/FeS/C microparticles

Stipulated varied compositions for each electrode produced are indicated in Figure 3-6.

3.2.3.4 Electrode Production

Following the mixing process, composite mixtures were rapidly stuffed by auto-hot pressing onto the Ni mesh. The final electrode thickness and active material loading were 0.75±0.10 mm and 0.15±01 g cm^{-2} respectively. The composite powder deposition density on Ni mesh was approximately 0.16 g/cm^2. The composite mixture was deposited into two designs of Ni mesh substrates with different dimensions, 90 x 60 mm mesh for galvanostatic cycling measurements and 10 x 10mm mesh for cyclic voltammetry. The process was executed in concordance with the following parameters presented in Table 3-3. It should be noted that the plastic binders are always processed below their melting point so that the particles agglomerate only to electrode material and do not melt altogether. The melting point for Coathelyne binder is 105 ^{O}C thus a compacting temperature of 95-100 was adhered to.

Table 3-3: Operating parameters of the hot-pressing process

Parameter	Compacting Pressure ($kg.cm^{-2}$)	Temperature (°C)	Time (minute)
Value	40	97.5±2.5	5

The processes employed to construct test cells and bipolar are outlined in the section below.

3.2.4 Test Cell Construction

After producing the electrode, the cell assembly is the final step. For this step, a prismatic polycarbonate plastic case was designed and created. The case housed the synthesized Fe-based electrode, electrolyte and the commercial Ni cathode. A 3D conception of the cell with two electrodes is shown below in Figure 3-8.

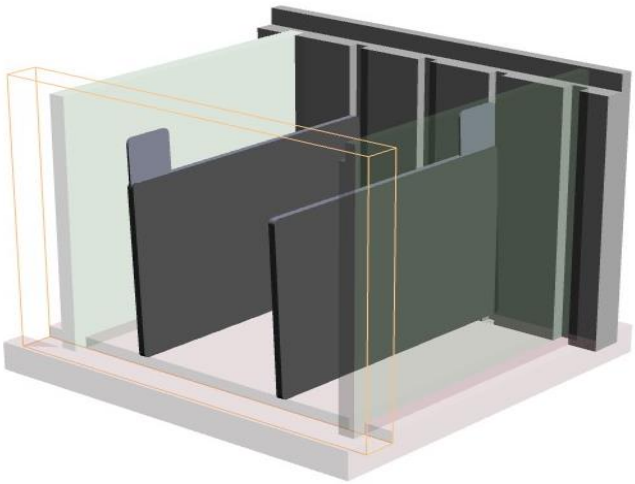

Figure 3-8: 3D conception of the cell with two electrodes

Basically, for this type of cell, only one anode and one cathode could be put inside the cell. The two electrodes should have the same dimensions, the same surface area, and the same weight.

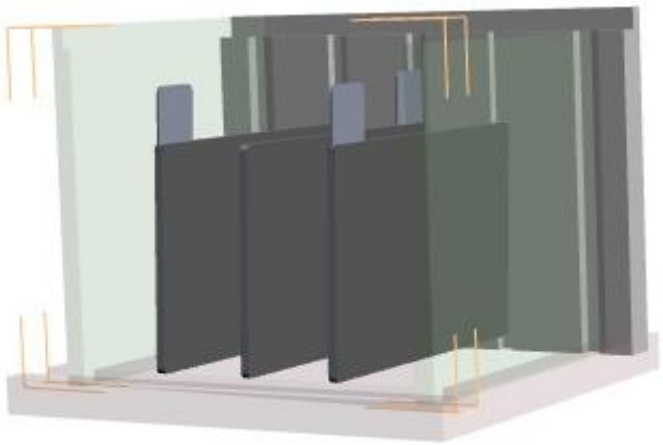

Figure 3-9: 3D conception of the cell with three electrodes

In the case of a three-electrode cell, which is depicted in Figure 3-9, two positive electrodes are connected to the same electrical output and to one negative electrode only. This configuration was only utilised for the quantification of capacity, coulombic efficiency and polarization characteristics (as described in Section 3.4.2). The design adopted for the Ni-Fe

commercial prototype is discussed in Section 3.2.5). Figure 3-10 depicts the summated process flow adopted for this study.

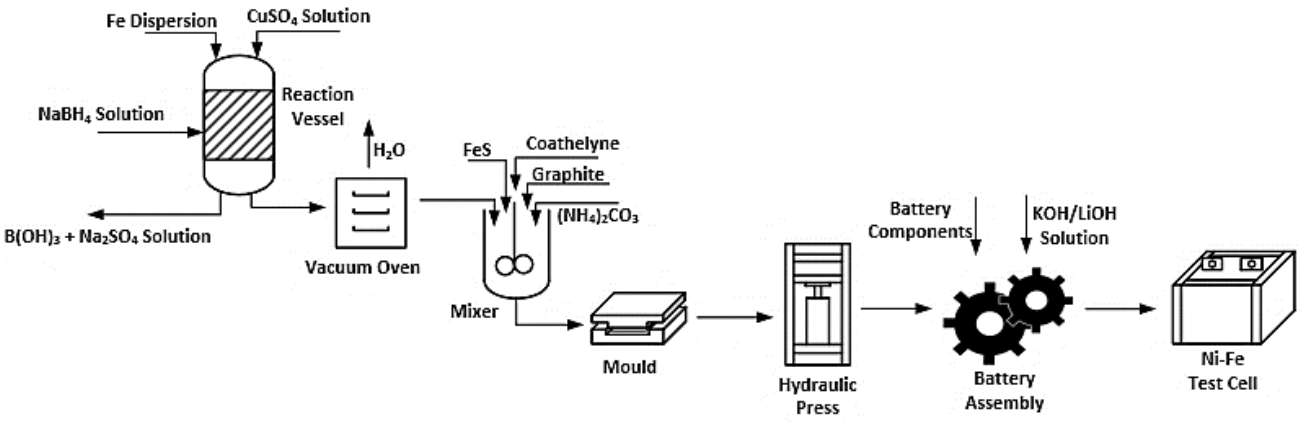

Figure 3-10: Process flow diagram of the Ni-Fe test cell production

3.2.5 Bipolar Ni-Fe Battery Construction

After optimisation of the electrode, the battery assembly is the final step. For this step, a bipolar battery was constructed (Fraunhofer UMSICHT, 2019). Fraunhofer UMSICHT (2019) stated that the bipolar Ni-Fe design exploits an innovative combination of optimised battery components and design in conjunction with the application of novel mass-production techniques. By employing the bipolar battery design, more than 75% of conventional battery constituents such as insulating material, electrolyte and cables can be saved. This design offers a more cost-effective alternative approach through complete replacement of costly nickel-mesh with a non-corrosive electro-conductive polymer film also known as a bipolar plate.

In this research project, in collaboration with Fraunhofer UMSICHT and Volterion GmbH technology partners, the development and optimisation of the individual components and individual battery cells were addressed and the knowledge acquired was utilised to construct a bipolar Ni-Fe battery prototype model. The 25 Wh (5.25 Ah/4.8 V) Ni-Fe prototype in the bipolar design was constructed and examined. The successful construction of the bipolar battery prototype should pioneer a new generation of efficient and cost-effective storage

batteries. The process flow adopted for the production of 25Wh bipolar Ni-Fe battery is illustrated in Figure 3-11.

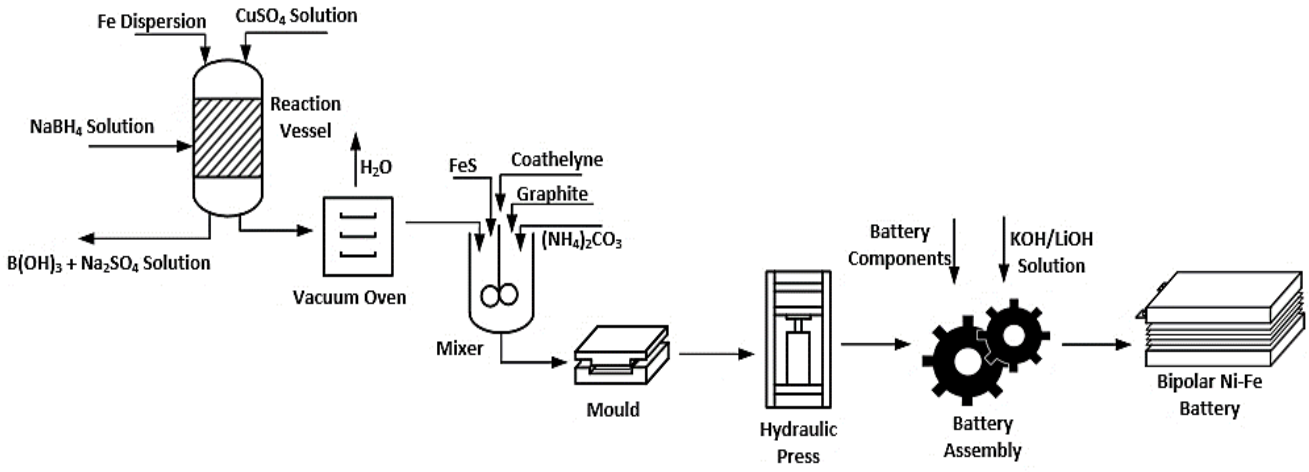

Figure 3-11: Process flow diagram for the production of 25Wh bipolar Ni-Fe battery

3.3 Material Characterization

3.3.1 X-Ray Diffraction

3.3.1.1 Working Principle

X-ray diffraction is computed from the constructive interference of monochromatic X-rays with a crystalline sample (Guinier, 2013). Guinier (2013) added that these X-rays are generated by a cathode ray tube, filtered to produce monochromatic radiation, collimated to concentrate, and projected into the crystalline sample. The interaction of the incident rays with the sample formulates constructive interference signals (diffracted X-ray) which satisfy Bragg's law (Equation 3-1);

$$n\lambda = 2d\sin\theta \qquad [3\text{-}1]$$

where n is a positive integer, λ is the wavelength of the incident ray, θ is the scattering angle and d is the interplanar distance (in Angstroms). Bragg's law relates the wavelength of electromagnetic radiation to the diffraction angle and the lattice spacing (interplanar distance) in the crystalline structure of the sample. The formulated diffracted X-ray signals are then detected, processed and counted. By scanning the sample through a range of 2θ angles, all

possible constructive interference signals (diffraction X-ray) of the lattice should be obtained attributable to the random orientation of the crystals. Conversion of the diffraction peaks to *d*-spacings sanction the identification of the compound(s) in the sample because each compound has a set of unique *d*-spacings. Typically, the compound identification is attained by comparison of *d*-spacings with standard reference patterns.

3.3.1.2 Procedure for XRD Analysis

The fresh electrode materials, as well as the charged and discharged electrode materials, were characterized by X-ray diffraction (XRD) using a D8 Diffractometer with a theta-theta goniometer (iThemba Labs, South Africa). Phase identification was done in DIFFRAC.EVA software and the plane reflection were indexed using powder diffraction file (PDF). A qualified lab technician conducted the analysis and provided the results.

3.3.1 Scanning Electron Microscopy

3.3.1.1 Working Principle

Stokes (2008) defined a scanning electron microscope (SEM) as a type of electron microscope that creates images by scanning the specimen's surface with a focused beam of high energy electrons. The electrons interact with atoms in the specimen, generating various signals that constitute information about the specimen's surface topography, morphology and composition. The electron beam is scanned in a raster scan pattern. The position of the electron beam is coupled with the frequency of the detected signal to formulate an image. Detection of secondary electrons emitted by atoms excited by the electron beam is the prevalently applied SEM mode according to Suryanarayana (2016). The schematic diagram of a typical SEM is presented in Figure 3-12.

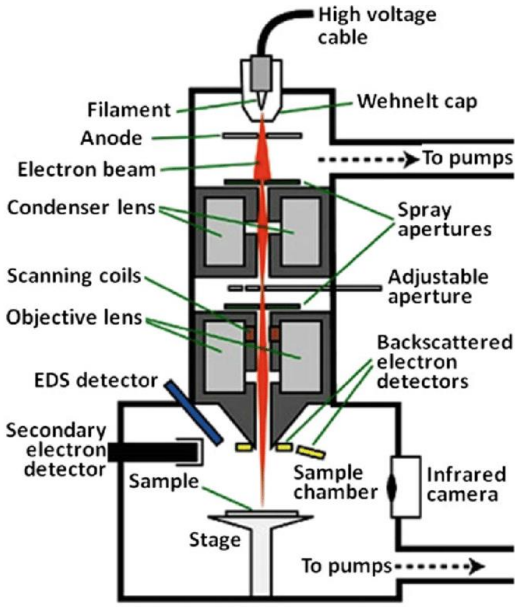

Figure 3-12: Schematic diagram of a SEM machine (Suryanarayana, 2016)

3.3.1.2 Procedure for SEM Analysis

The morphologies of all Fe-matrix electrodes were taken by a TESCAN MIRA SEM with Raman confocal system (EMU-University of Cape Town, South Africa). A qualified lab technician conducted the analysis and provided the results.

3.3.1 Transmission Electron Microscopy

3.3.1.1 Working Principle

Transmission electron microscopy (TEM) operates like a slide projector (Reimer, 2013). Reimer (2013) annotated that a projector fires a beam of light which transmits through the slide. The patterns painted on the slide only allow certain segments of the light beam to pass through. Therefore, when the light falls on the screen, the transmitted light beam replicates the patterns on the slide, formulating an expanded image of the slide. TEMs employs the same principle, except that they fire a beam of electrons (like the light in a slide projector) through the specimen (like the slide) to generate a highly magnified image (like the enlarged image). However, in TEM, the electron beam transmission is eminently dependent on the properties of the specimen being examined. The determinant properties include particle size, density, composition, etc. For example, porous (less dense) material will transmit more electrons while dense material will transmit less. As a result, a specimen with small particle size, low density

and non-uniform composition is ideal to be examined by this technique. The signal generated the by high energy electron transmission is projected onto a phosphor screen as a visual image for the operator to see. Figure 3-13 exhibits the schematic of TEM imaging methodology.

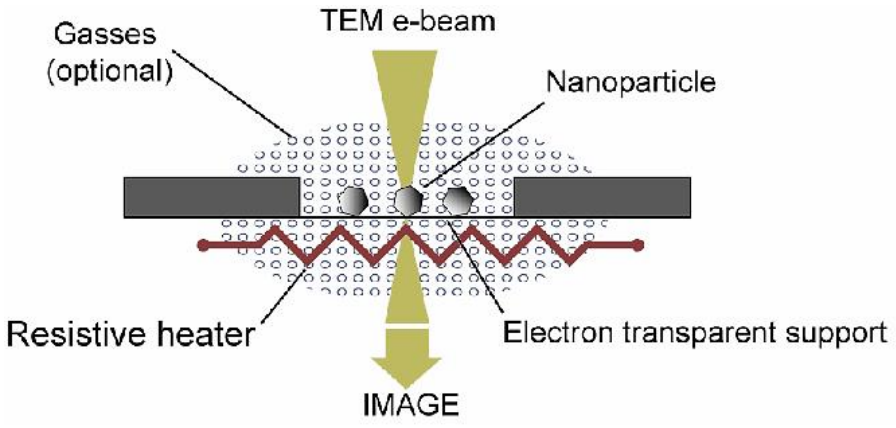

Figure 3-13: Schematic of TEM imaging methodology (Inkson, 2016)

3.3.1.2 Procedure for TEM Analysis

The nanostructure of Fe-matrix material was analysed by a Zeiss EM 912 CRYO EFTEM (EMU-University of Cape Town, South Africa). A qualified lab technician conducted the analysis and provided the results.

3.3.2 Porosimetry

3.3.2.1 Working Principle

Porosity is a measure of fluid-accessible void spaces in a solid material. Porosity, reported as either a fraction or a percentage, is defined as the void space fraction of the bulk volume (Sasanian & Newson, 2013). Sasanian & Newson (2013) iterated that since water wet or penetrate most solid porous substances, it will spontaneously penetrate pores through capillary action, it mustn't be forced into the pores by the application of external pressure. The porosity is determined by quantifying two of the three variables: bulk volume (V_b), pore volume (V_p) or grain volume (V_g). Equations 3-2 are then used to compute porosity (Φ):

$$\Phi = \frac{V_p}{V_b} \qquad [3\text{-}2]$$

By quantifying the volume of water that intrudes into the sample material, the volume of pores in the corresponding electrode is approximately quantified.

3.3.2.2 Procedure for Porosimetry

Porosity quantification was executed by first immersing the Fe-based composite electrode in a water bath. The electrode was drawn off the water bath after being completely submerged for 10 minutes. The excess water on the surface of the electrode was quickly absorbed by a paper towel, and afterwards, the electrode was weighed. The mass of the electrode before and after submergence in the water bath was noted. The difference between the two mass values (mass before and after water absorption) stipulated the quantity of water occupying the pores of the electrode. The pore volume was computed from multiplying the water mass uptake with the specific volume of water. The ratio of the volume of pores to the geometric volume of the electrode was inferred as the porosity of the electrode. The porosity of the electrode was calculated as illustrated in Equation 3-2. The pore volume is the sole representative of the volume accessible by the electrolyte solution.

3.4 Electrochemical Characterization

3.4.1 Cycling Voltammetry

3.4.1.1 Working Principal

Cyclic voltammetry (CV) is a technique the expansively utilised for acquiring quantitative and qualitative information about electrochemical reactions and reactivity. It offers the instantaneous identification of redox potentials relative to the electro-active species under investigation, substantial information about the thermodynamics and kinetics of the redox reactions and analysis of electron transfer-initiated chemical reactions, which includes adsorption reactions (catalysis) (Davies *et al.*, 2005).

Cyclic voltammetry consists of linearly scanning the potential of the working electrode through a zigzag potential waveform. Figure 3-14 below depicts the typical potential-time profiles generated during linear sweep and cyclic voltammetry.

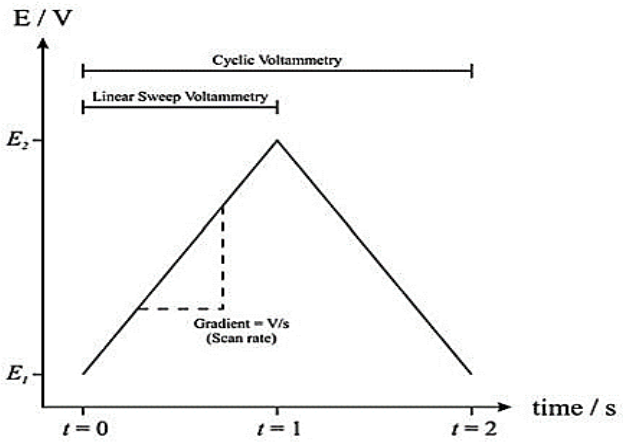

Figure 3-14: Potential-time profiles generated during linear sweep and cyclic voltammetry

The rate at which the potential is swept from E1 to E2 is termed the voltammetry scan rate (mV/s). In the case where the potential sweep is stopped at E2, this is regarded as linear sweep voltammetry (Davies *et al.*, 2005).

If the potential is swept back to E1, a full potential cycle is generated, this is identified as cyclic voltammetry. Single or multiple cycles can be enacted depending on the information being sought. The potentiostat measures the resulting current that emanates during the full duration of the potential sweep when potential (voltage) is applied.

The current versus potential (voltage) plot depicted in Figure 3-15 is termed a "cyclic voltammogram", CV. A cyclic voltammogram is multifaceted and dependent on multiple factors that include time and chemical and physical properties of the sample.

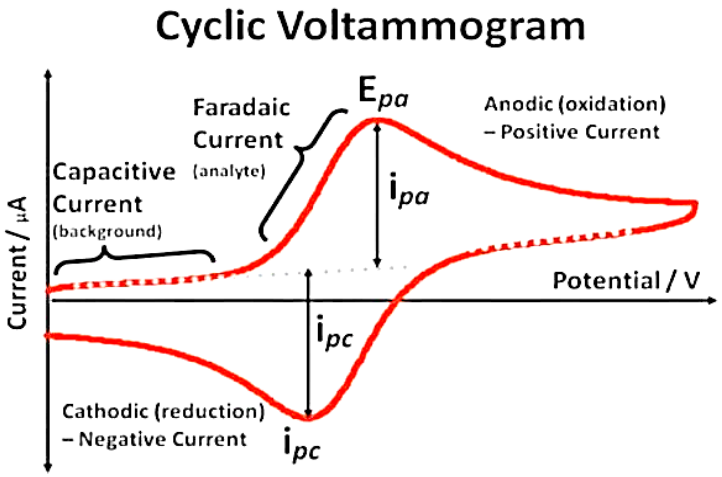

Figure 3-15: Cyclic voltammogram (Davies *et al.*, 2005)

As shown in Figure 3-15 the voltammogram consists of, mainly, two current peaks which are the oxidation peak (anodic peak) and the reduction peak (cathodic peak). The potential window is fixed before testing, taking into consideration that all the standard potential of species' electrochemical reactions involved should fall within the specified potential range.

3.4.1.2 Procedure for Cycling Voltammetry

Figure 3-16 presents the experimental testing configuration for cycling voltammetry.

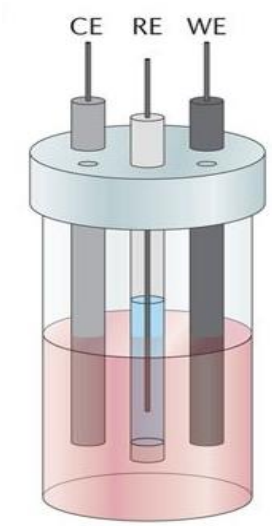

Figure 3-16: Experimental testing configuration for cycling voltammetry (Lee *at al*., 2017)

The experimental testing configuration for cyclic voltammetry consists of three electrodes immersed in 6 M KOH/1 M LiOH electrolyte solution. The three electrodes, namely the working electrode (Fe-based electrode), the counter electrode (Pt electrode) and the reference electrode (Hg/HgO electrode), are connected to the N series Autolab potentiostat/galvanostat system.

All the electrodes were immersed totally in the electrolyte to obtain accurate data results. This configuration serves just for electrochemical testing purposes. But during the experiment, it must be ensured that there is no side reaction going on inside the testing cell. Gas tightness is important since CO_2 present in the air that fills the laboratory, reacts with KOH to form K_2CO_3 and H_2O as shown in the reaction below:

$$CO_2 + 2KOH \rightarrow K_2CO_3 + H_2O \qquad [3\text{-}3]$$

This reaction was curbed by gas tightening the apparatus. If the apparatus is not gas-tight, the concentration of electrolyte falls further and decreases the measuring results. The reason for even temperature control is that the electrolyte has a different conductivity depending on the temperature and thus, a comparability of the measuring results at different temperatures is difficult.

The temperature control also helps to ensure that the internal pressure in the apparatus does not become smaller than the ambient pressure since the temperature thus no longer has a disturbing effect on the cell internal pressure. Figure 3-18 depicts the on-ground schematic representation of the test environment.

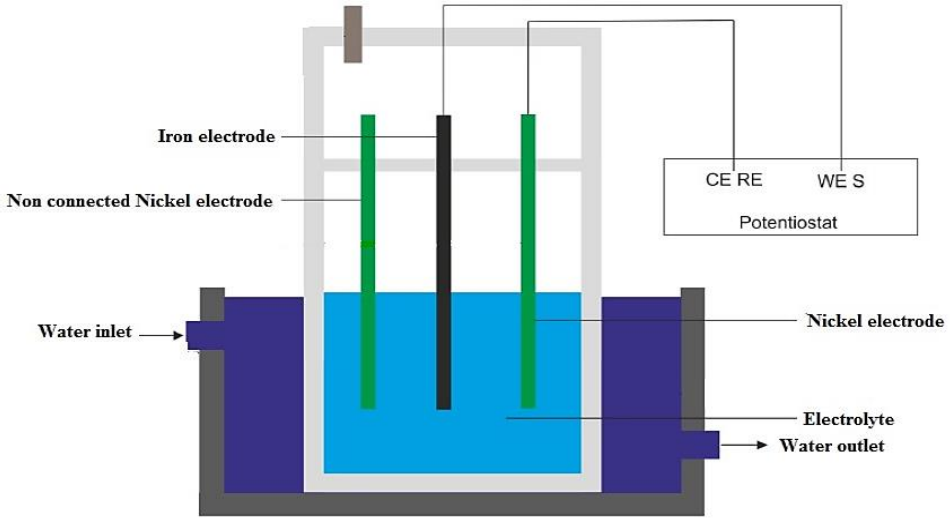

Figure 3-17: Schematic representation of the on-ground test environment

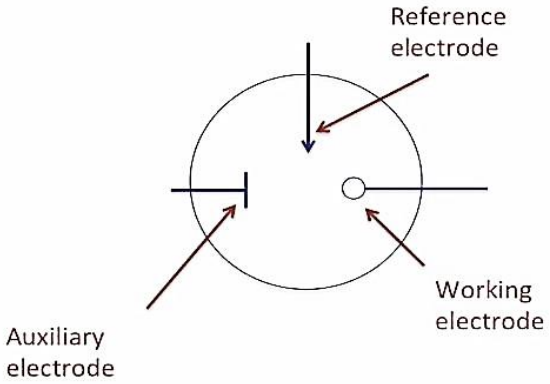

Figure 3-18: Schematic representation of the on-ground test environment (Top view)

Nitrogen was filled into the apparatus via the rubber stopper, in which a fermenting tube is attached to the apparatus during the execution of the test run. This nitrogen is supposed to

displace the CO_2 from the apparatus so that it is not absorbed by the electrolyte and thus no potassium carbonate forms in the electrolyte.

The 10x10 mm Fe-based electrode was immersed in the electrolyte (6 M KOH/1 M LiOH) together with a Pt counter electrode and Hg/HgO reference electrode (as indicated in Figure 3-16). The electrodes were contacted with alligator clips, which are located at the end of the measuring lines. These measuring cables were connected to the Autolab potentiostat via cable glands through the cover of the apparatus. The measurements were recorded at a sweep rate of 2.5 mVs^{-1} and within a potential range from -0.4 to -1.4 V.

3.4.2 Galvanostatic Charge/Discharge

3.4.2.1 Working Principle

In galvanostatic charge/discharge, the working electrode is subjected to constant current and the resultant potential (voltage) is gauged against a standard potential of a reference electrode as a function of time (Pyun *et al*., 2012). Pyun *et al*. (2012) iterated that when applied current (lower than limiting current) is initially inflicted onto the electrode, the gauged potential abruptly drops due to the ohmic potential drop (I*R loss), and after that, it drops gradually, because concentration overpotential (due to limited mass transport) is generated as the concentration of the reactant species is depleted at the electrode surface.

If the applied current is more than the limiting current the diffusion process cannot deliver the required current flux. The electrode potential consequently increases rapidly until it reaches the electrode potential of the next existing reaction, and so on.

In galvanostatic cycling, the constant current (anodic/cathodic) applied to the working electrode prompt the electroactive species to be oxidized/reduced at a constant rate. The electrode potential varies with time as the concentration ratio of reactant species to product species changes at the electrode surface. After the concentration of the reactant drops to zero at the electrode surface, the reactant might be insufficiently present at the surface to accept all of the electrons being emitted by the applying constant current.

The potential of the electrode will then sharply shift to more anodic/cathodic values. The shape or profile of the curve is regulated by the reversibility of the electrochemical reaction(s)

occurring at the working electrode. The current applied to the working electrode can be varied with time, to inspect other electrochemical reaction behaviours of the working electrode.

If the current is abruptly shifted from an anodic to cathodic, the reduction the anodic reaction product (i.e., anodic product) initiates. Then, the electrode potential proceeds in the cathodic direction as the concentration of the cathodic reaction product (i.e., cathodic product) increases. On the other hand, in cyclic chronopotentiometry, the applied constant current is repeatedly reversed.

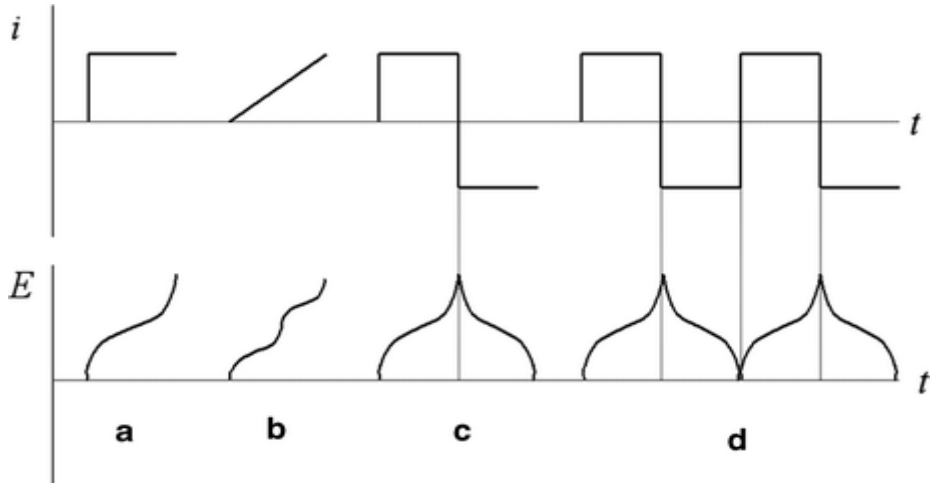

Figure 3-19: Different types of chronopotentiometry experiments: (a) constant current chronopotentiometry, (b) linearly rising current chronopotentiometry with linearly, (c) current reversal chronopotentiometry and (d) cyclic chronopotentiometry (Pyun *et al*., 2012)

The standard galvanostatic techniques (presented in Figure 3-19) can be readily extended to comprehensively characterize the electrochemical properties of electroactive materials. Generally, current reversal and cyclic galvanostatic programs are frequently applied to quantify and evaluate the specific capacity, energy efficiency and cycling stability of the respective electrode.

A typical galvanostatic charge/discharge profile of Ni-Fe cell at a rate of 0.2C is frequently utilised (In battery field, 0.2C (same as C5) rate represents the optimal discharging/charging rate at which the Ni-Fe battery will deliver nominal or highest capacity (Reddy & linden, 2010).

The total quantity of charge per total active mass existing in a fully charged cell (or storable in a fully discharged cell) can be calculated at the optimal C rate (0.2C for Ni-Fe batteries) from the charge transferred during the charging (or discharging) process in terms of $mAh \cdot g^{-1}$ or $C \cdot g^{-1}$.

Alternatively, the quantity of current (or charge) accepted or discharged can be converted to the number of moles of electroactive atoms as long as the electrode potential is attained in a (quasi-) equilibrium state. The potential-time plot, generated through cyclic chronopotentiometry or current reversal chronopotentiometry, can be effectively utilised to characterize or identify the multi-step redox reactions occurring during the electrochemical process.

3.4.2.2 Equipment for Galvanostatic Analysis

- **Equipment and Software for Galvanostatic Analysis**

In order to make the galvanostatic cycling measurement, a battery testing system BTS TC54 is used.

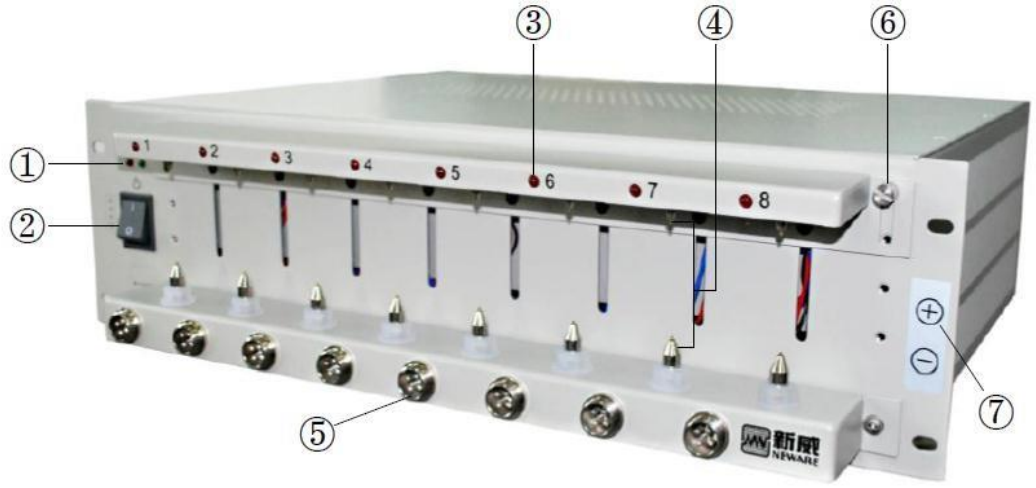

Figure 3-20: Front panel of the battery testing station

Where:

1- Power and Signal LED 2- Power On/Off

3- Channel working LED (8 in all) 4- Battery clamp (battery fixed middle)

5- 164 Air socket (connecting alligator clamp) 6- clamp spacing adjustment handle

7- Test channel positive and negative directions tags

BTS Series Battery test system has three clamps: universal, alligator and polymer clamps.

- **Software**

The host computer software of BTS Battery Testing System (serial port version) consists mainly of two parts:

A: BTS Test control software: BTS controle.exe, TC54 is the version number of the test control software, the software controls the entire process of the battery-testing, this includes test step configuration, generation of test data files and back up management.

B: BTS battery testing system "data analysis software" ___ BTSDA.exe, the software encompasses analysis test data, generation of graphs and data export.

Test control software is NEWARE BTS series for battery testing systems.

3.4.2.3 Procedure for Galvanostatic Analysis

- **Start-up and Operation**

Start-up: set steps on the battery channel, start channels work according to the setting step: including constant current discharge, constant current charge, constant voltage charge, constant current constant voltage charge, constant power discharge, rest, cycle, etc.

- End: working channel will automatically stop after completion of all settings of the steps, while users can request the program to be stopped whenever.
- Resume: for resuming a stopped channel, it's available to use the "resume "to restore the original testing process and maintain data on.
- Jump: the users can force to stop the current step of the channel and jump the target steps to continue the test.
- Move: the user could move the current step to the target channel, and the original stops.
- Channel info: Query the situation of the working channel;
- Open Data: for working channel data (Voltage, current, capacity, and cycles) for real-time display.

Software Main Window, opening the software, the system will automatically search all online testing channels:

Figure 3-21: Main window of TC54

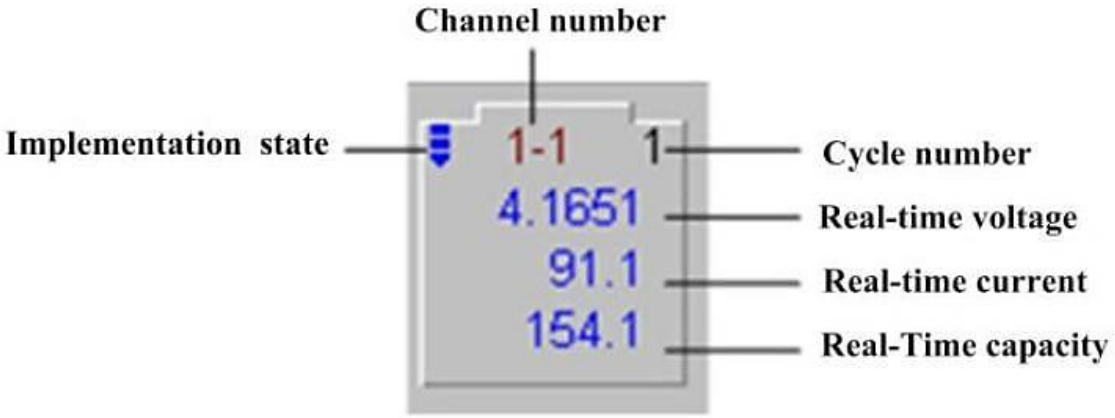

Figure 3-22: Analog battery display of the channel

In the step set column, users can set up the testing process, meanwhile set "the record condition" and "protect param" and other restrictions. The types of step utilised include a total of ten: Constant Current (C_C) Charge, Constant Current (C_C) Discharge, Constant Voltage (C_V) Charge, Constant Power (C_P) Discharge, Constant Resistance (C_R) Discharge, CC_CV Charge, Rest, Pause, Cycle, End, Step over conditions including current, time, voltage, capacity and change in voltage (*-ΔV*).

• C_C charge: the parameter of the current must be set; the user can set the step over conditions according to different requisites of the test.

• C_C discharge: The parameter of current must be set; the user can set the step over conditions according to different requisites of the test.

• C_C charging: the parameter of voltage must be set; the user can set the step over the conditions according to different requisites of the test.

The above-mentioned programs are the mostly employed programs for galvanostatic analysis.

- **Electrochemical Activation**

Throughout the whole activation/formation period, the cells were placed in a water bath at a temperature of 25±2 ^{O}C. Cells were connected to a battery management device where they undergo a series of charge/discharge cycles for X (10-20) cycles until a steady capacity was attained, each cycle comprised of:

a) A rest step of 30 minutes
b) A charge step at current, in amperes, of *I*=50 mA/g with voltage limit, V_{max}=1.8 V/Cell
c) A discharge at current, in amperes, of *I*=50 mA/g with voltage limit, V_{min}=0.8 V/Cell
d) A rest step for 30 minutes

- **Cycling Test**

Throughout the whole test period, the cells were placed in a water bath at a temperature of 25±2 ^{O}C. Cells were connected to a device where they undergo a series of discharge cycles for 40 cycles, each cycle comprised of:

a) A rest step of 30 minutes
b) A charge step at current, in amperes, of *I*=100 mA/g with voltage limit, V_{max}=1.75 V/Cell
c) A discharge at current, in amperes, of *I*=100 mA/g with voltage limit, V_{min}=0.8 V/Cell
d) A rest step for 30 minutes

- **Charge Retention Test**

Throughout the whole test period, the cells were placed in a water bath at a temperature of 25±2 ^{O}C. The cells were connected to a device where they will be fully charged, the charge step comprised of:

a) A charge step at current, in amperes, of *I*=100 mA/g with voltage limit, V_{max}=1.75 V/Cell

After its fully charged, the cells were stored for 10 days. After this storage period, the cells were discharged, the discharge step comprised of:

b) A discharge at current, in amperes, of *I*=100 mA/g with voltage limit, V_{min}=0.8 V/Cell
c) A charge step at current, in amperes, of *I*=100 mA/g with voltage limit, V_{max}=1.75 V/Cell

- **Polarization Test**

Throughout the whole activation/formation period, the cell was placed in a water bath at a temperature of 25±2 ^{O}C. Cells were connected to a battery management device where they undergo a charge step and then discharge at a specific current for 5 seconds with the voltage output measured at each specific current, each cycle comprised of:

a) A rest step of 30 minutes
b) A charge step at current, in amperes, of *I*=1000 mA/g for 90 mins
c) A discharge at current, in amperes, of (*I*=200-2500 mA/g) for 5 seconds
d) A rest step for 30 minutes

Chapter 4: Results and Discussion

4.1 Overview

This chapter is focused on the discussion and presentation of results attained from the experimental study focusing on the development of a high-performing Fe-matrix electrode for Fe-based alkaline batteries. In order to assess the electrochemical performance of the in-house produced electrodes, the electrodes were characterised by physical and electrochemical examinations. Based on the gathered analysis the optimally performing electrode can then be qualified for use as a negative electrode in construction of a bipolar Ni-Fe alkaline battery. In this chapter, the production of in-house electrodes started by analysing the electrode materials followed by investigating the electrodes' redox behaviour, specific capacity, coulombic efficiency and polarization performance. The material and energy balances of the bipolar Ni-Fe battery construction process were determined. This chapter also presents the cost of bipolar Ni-Fe battery products developed and the cost of production incurred during the bipolar Ni-Fe battery construction process.

The study was performed as described in chapter three (Section 3.2) and results are presented and discussed in Section 4.2, Section 4.3 and Section 4.4. The bipolar Ni-Fe battery prototype developed in this study is discussed in Section 4.5. The material and energy balance calculations are presented in Section 4.6 followed by a cost evaluation section on Section 4.7.

4.2 $FeCu_x$ Electrode Materials: The Effects of Cu

4.2.1 Materials Characterisation

4.2.1.1 Transmission Electrode Microscopy

Figure 4-1 shows the energy-filtered transmission electron microscopy (EFTEM) imaging of the $FeCu_{0.2}$ composite material to confirm the Fe core-Cu shell particle arrangement. It is evident from Figs. 4 a-c that the particles are in a core-shell structure with particle sizes in a typical range of 150 to 250 nm. In Figure 4-1 a and c, the light portion of the image represents the Cu and Fe distribution respectively. Because a part of Fe was oxide and dissolved Fe^{2+} was reduced back to elemental Fe after initial Cu precipitation, the coating layer contained Cu and some Fe as depicted by EFTEM imaging (Figure 4-1).

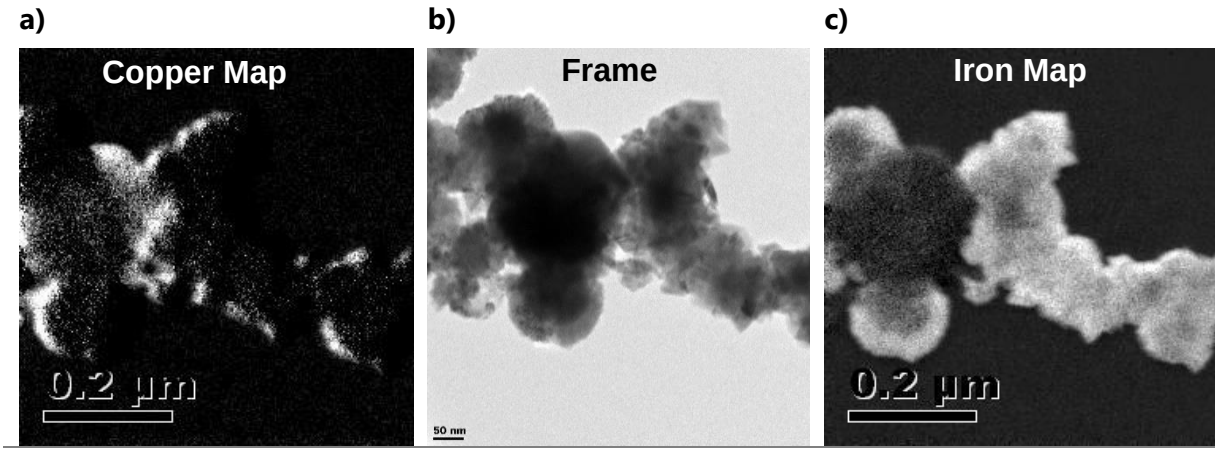

Figure 4-1: $FeCu_{0.25}$ material EFTEM imaging analysis

4.2.1.2 X-Ray Diffraction Analysis

Figure 4-2 and Figure 4-3 depicts the XRD patterns of pure Fe, $FeCu_{0.25}$ composite electrodes respectively. Per each electrode, 3 samples in fresh, charged (after 40 cycles) and discharged (after 40 cycles) state are analysed. The different crystal planes in the pattern are identified using the powder diffraction file directory (PDF numbers). The PDFs for Fe, Cu, C, Fe_3O_4 and Cu_2O are 00-006-0696, 00-004-0836, 00-026-1076, 00-019-0629 and 00-0050667 respectively.

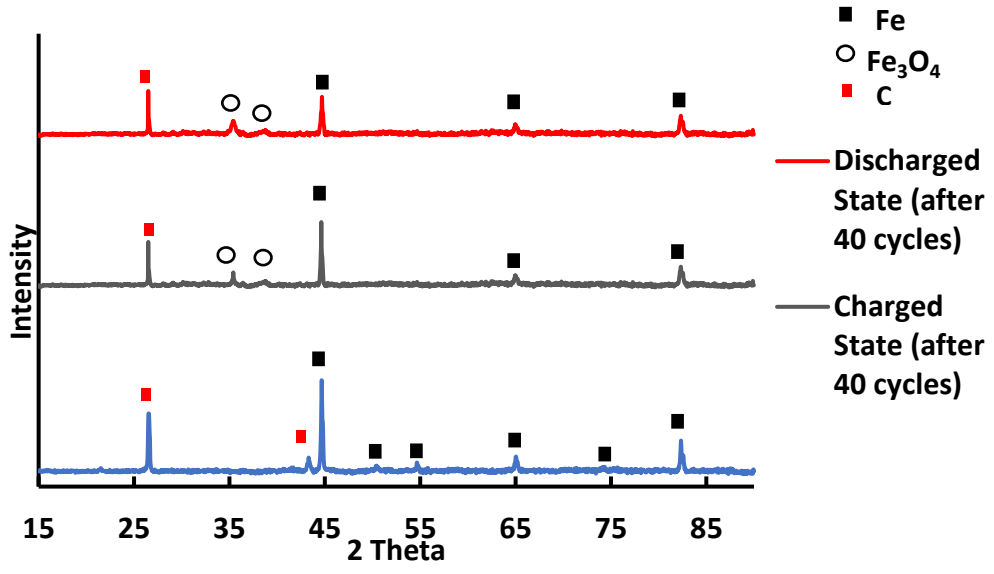

Figure 4-2: XRD patterns for pure Fe electrode

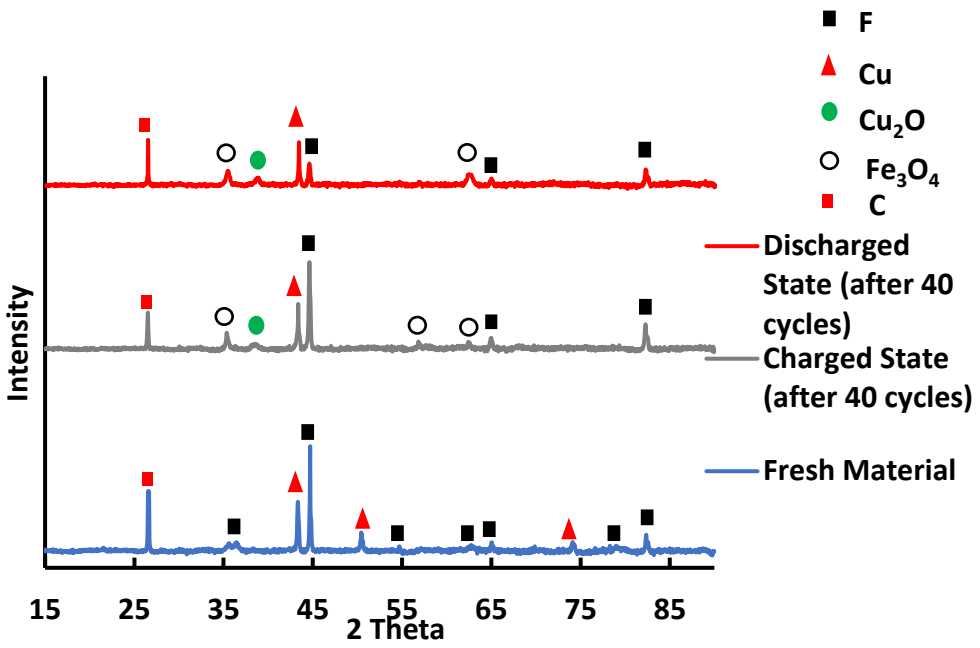

Figure 4-3: XRD patterns for $FeCu_{0.25}$ electrode

In Figure 4-2 peaks for Fe and C can be visibly identified as the dominant phases for the pure Fe sample in fresh state. The (110) plane for Fe occurring at 2θ between 42.5 and 45.4 ° was the dominant facet for Fe in all electrode formulations analysed. The crystallite size of fresh material particles is approximately 192 nm which decreased to 161 nm (charged state after 40 cycles) due to particle surface passivation (Manohar *et al*. 2016). Particle sizes were calculated using Math! Software that adopts the Scherrer equation. When the fresh material is deeply discharged, the XRD analysis of the pure Fe material indicated a decrease in Fe peak intensity with notable peaks of Fe_3O_4. However, the variance between Fe peaks in fresh and discharged material is minimal indicating a low utilisation of active material (Kao *et al*., 2011). In theory, the major product during discharge should be $Fe(OH)_2$ which was not detected by XRD of discharged Pure Fe electrode material, implying that it was amorphous (Huang *et al*., 2018; Kao *et al*., 2011). The absence of $Fe(OH)_2$ was observed in all XRD results from discharged electrode materials. The decrease in Fe peak intensity between fresh Fe and charged electrode material might be ascribed to the limited reversibility of the electrochemical reaction.

Figure 4-3 shows that the fresh $FeCu_{0.25}$ composite has strong peaks of Fe and Cu and weaker peaks of Cu which aligns with high Fe to Cu ratio. When the fresh $FeCu_{0.25}$ composite material was deeply discharged, the XRD analysis indicated that the peaks of Fe become weaker and the peaks of Fe_3O_4 are observed. The XRD analysis of the discharged $FeCu_{0.25}$ composite material also depicts that little Fe remains after deep discharge indicating a high utilisation of

active material compared to that pure Fe electrode material, and the peaks of Fe_3O_4 are much stronger (compared to peaks pure Fe electrode material) due to an increased amount of active material (Fe) participating the electrochemical reaction (Kao *et al*., 2011). Furthermore, the peak of Cu_2O was observed, indicating that some of the Cu was oxidized at a deep discharge state. The negligible decrease in Fe peak intensity between fresh $FeCu_{0.25}$ and charged $FeCu_{0.25}$ electrode material might be ascribed to the amplified reversibility of the electrochemical reaction induced by Cu's ability to increase electro-conductivity of the electrode (Huang *et al*., 2018).

The average crystallite size of the $FeCu_{0.25}$ particles slightly decreased from 141 nm to 117 nm after 40-cycles. The lack of anti-passivation agent in the electrode composite leads to surface passivation due to the inevitable formation of the discharge products (Fe_2O_3 and $Fe(OH)_2$) which exhibit sparse electro-conductivity (Posada *et al*., 2016).

4.2.1.3 Scanning Electrode Microscopy

Figure 4-4 6 a1 and a2 shows the SEM images for the pure Fe in the fresh and charged state respectively while Figure 4-4 b1 and b2 arrays the SEM images for the $FeCu_{0.25}$ electrode in the fresh and charged state. The $FeCu_{0.25}$ composite particles were synthesized by a two-step method that included Cu autocatalytic and Fe electroless deposition. The original Fe particles (visible in Figure 4-4.a1) appear cubical in shape with particle size ranging from 150-250nm. When Cu was autocratically deposited onto Fe particles and subsequently electroless plated with Fe using the $NaBH_4$, particles appear more spherical and larger with a particle size distribution between 150 and 300nm ((visible in Figure 6.b1). Zhao *et al.* (2016) stipulated that shape of nanoparticles is mostly regulated by surface energy minimization; therefore, rather intuitively, spherical or roughly spherical polyhedral shapes with the lowest surface-to-volume ratio (i.e. number of surface atoms over number of bulk atoms) are the most likely to form in a process characterised by spontaneous chemical kinetics. The SEM images in Figure 4-4 a2 and b2 confirm that the $FeCu_{0.2}$ based composites inhibit particle agglomeration upon cycling compared to pure Fe material which indicates visible particle agglomeration after 40 cycles as depicted in Figure 4-4 a2.

a1) Fresh Fe electrode **a2) Charged Fe electrode (after 40 cycles)**

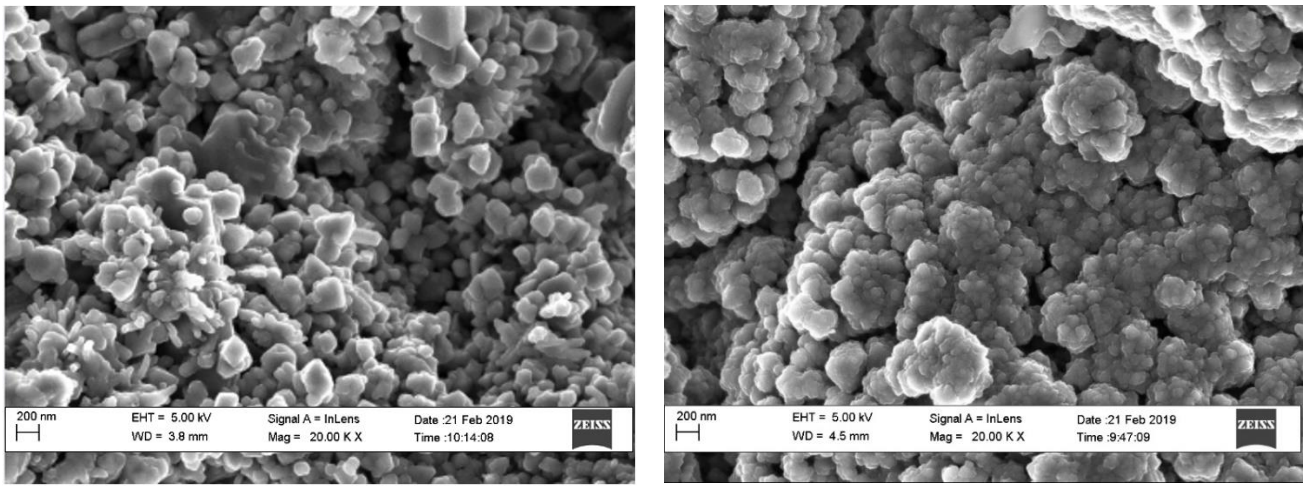

b1) Fresh $FeCu_{0.25}$ electrode **b2) Charged $FeCu_{0.25}$ electrode (after 40 cycles)**

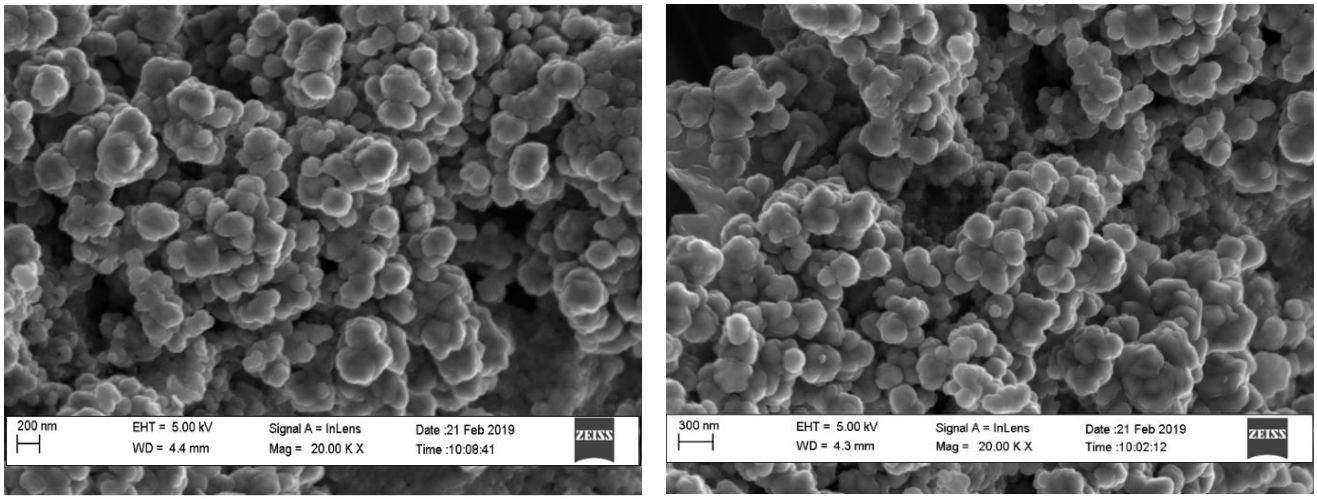

Figure 4-4: SEM images for a) pure Fe electrode before and after 40 cycles and b) $FeCu_{0.25}$ electrode before and after 40 cycles

4.2.2 Electrochemical Characterisation

4.2.2.1 Cyclic Voltammetry

Cyclic voltammograms of pure Fe and $FeCu_{0.25}$ composite electrodes are shown in Figure 4-5. The electrodes were activated for 50 cycles at a scan rate of 200 mVs^{-1} vs. the Hg/HgO in 6 M KOH/1LiOH electrolyte. The activation step was to remove any surface impurities and stabilize the electrochemical response of the electrode. The graph shows the cyclic voltammograms obtained after the 30^{th} cycle at a scan rate of 2.5 mVs^{-1} vs. the Hg/HgO in 6 M KOH/1LiOH electrolyte.

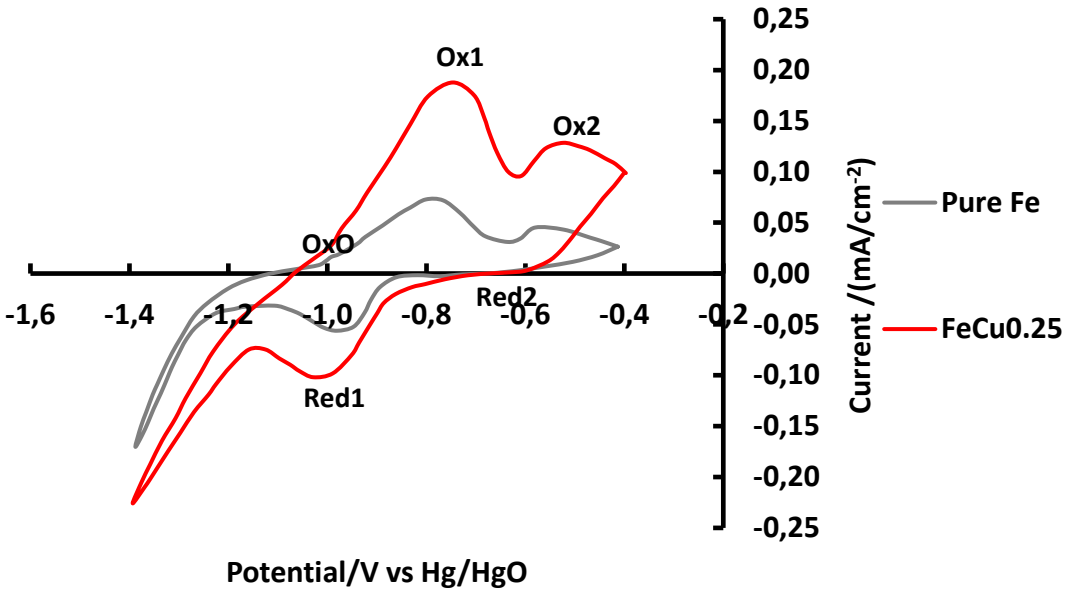

Figure 4-5: Cycling voltammetry of pure Fe electrode and $FeCu_{0.25}$ electrode electrode in 6M KOH /1M LiOH at 2mV/s

All three cyclic voltammograms depict two major oxidation peaks (Ox1 and Ox2) for Fe as well as an additional small pre-peak (Ox0) due hydrogen oxidation and hydroxyl ion adsorption i.e. $H_2 \rightarrow 2H_2O$ (Posada & Hall, 2016). The peak Ox1 corresponds to the $Fe \rightarrow Fe(OH)_2$ while Ox2 corresponds to the $Fe(OH)_2 \rightarrow Fe_3O_4$ reaction (Huang *et al.*, 2018; Paulraj *et al.*, 2018). The phenomenon of the elimination of adsorbed hydrogen from the electrode during the anodic sweeping has also been observed by the electrochemical quartz crystal microbalance method, confirming the initial Fe/Fe(II) reaction step (Joiret *et al.*, 2002).

The Ox1 reaction is more favoured under the test conditions and appears twice as large as the Ox2 peak which indicates that there is a significantly higher charge associated with it. However other literature reports have shown a larger or equal sized Ox2 peak compared to the Ox1 peak (Luo *et al.*, 2017; Shangguan *et al.*, 2019; Weinrich *et al.*, 2017). A possible explanation for the smaller Ox2 peak could be due to partial oxidation which is limited by repulsion from the neighbouring Fe (II) sites. The ratio of the oxidation peaks may also be dependent on the type of Fe material analysed and the type of additives incorporated.

The Ox1 peaks show maximum peak heights at – 0.78 V and - 0.75 V for the pure Fe and $FeCu_{0.25}$ electrodes respectively. The Ox2 peaks show maximum peak heights at – 0.56 V and – 0.52 V for the pure Fe and $FeCu_{0.25}$ electrodes respectively. The addition of Cu element shifts the oxidation potentials to slightly lesser negative potentials. This shift implies a lowering in

over-potential. It was reported that the oxidation of Cu to Cu_2O takes place at −0.4641 V vs Hg/HgO (Giri & Sarkar, 2016; Manohar *et al.*, 2013). In case of the $FeCu_{0.25}$ electrode, the oxidation of Cu may also exist in parallel with the Fe (II)/Fe (III), though its peak was not distinct due its relatively small quantity in the electrode composite material.

The Red1 peaks, corresponding to the reduction of Fe (II) to Fe(0), shows maximum peak heights at – 0.98 V, – 1 V and – 1 V for the pure Fe, $FeCu_{0.25}$ and $FeCu_{0.25}$/15%FeS electrodes respectively. No clear peaks on the reduction of Fe_3O_4 to $Fe(OH)_2$ can be observed in all voltammograms, as this reaction would have preceded the $Fe(OH)_2$/Fe reduction peaks (Wang and Wang, 2016; Weinrich *et al.*, 2017). However, it cannot be ruled out that the reduction peak is an overlap of both the Fe(III)/Fe(II) and Fe(II)/Fe(0) reduction reactions as these two reduction reactions both occur within a very small potential window (Li *et al.*, 2017; Luo *et al.*, 2017; Shangguan *et al.*, 2015). Following this peak, however, the hydrogen evolution reaction becomes predominant at potentials more negative than − 1.16 V. The pure Fe electrode shows the smallest redox peaks compared to the $FeCu_{0.2}$ composite electrodes which indicate a lower ability of the electrode to store charge. The specific capacitance (C_s) were calculated using the following equation:

$$C_s = \frac{\int IdV}{mv\Delta V} \qquad [4\text{-}1]$$

Where C_s is specific capacitance (Fg^{-1}), $\int IdV$ is the area under the anodic curve, m is the mass of the active electrode material (g), v is the scan rate (Vs^{-1}) and ΔV is the potential window (V). The calculated specific capacitances for the pure Fe, $FeCu_{0.2}$ composite and $FeCu_{0.2}$/15%FeS composite electrodes are 84.7 Fg^{-1}, 233.3 Fg^{-1} and 286.7 Fg^{-1} respectively. Furthermore higher cathodic current densities are observed with the addition of Cu (from 74 to 188 mA cm^{-2}) which is beneficial for battery operations and utilization at high discharge rates (Paulraj *et al.*, 2017). The increased cathodic current density is attributed to the enhanced electronic conductivity by the metallic Cu present in the composite material (Huang *et al.*, 2018).

4.2.2.2 Galvanostatic Cycling

Figure 4-6 displays the discharge curves of pure Fe, and $FeCu_{0.2}$ composite electrode materials while Figure 4-7 displays the polarization curves of pure Fe and $FeCu_{0.25}$ composite electrode materials.

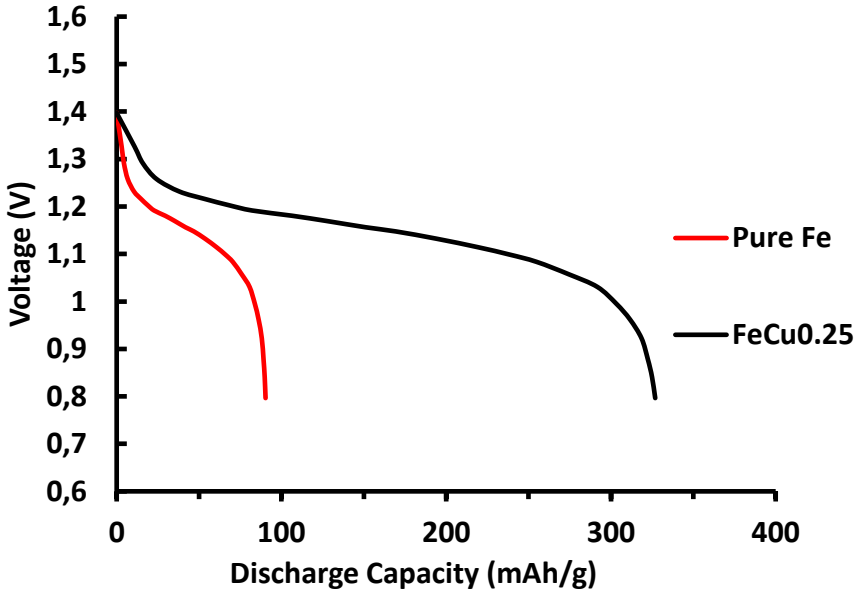

Figure 4-6: Discharge curves of pure Fe electrode and $FeCu_{0.25}$ electrode: the cells were charged at 100mA/g to 1.75 V, and then discharged at 100 mA/g C to 0.8 V

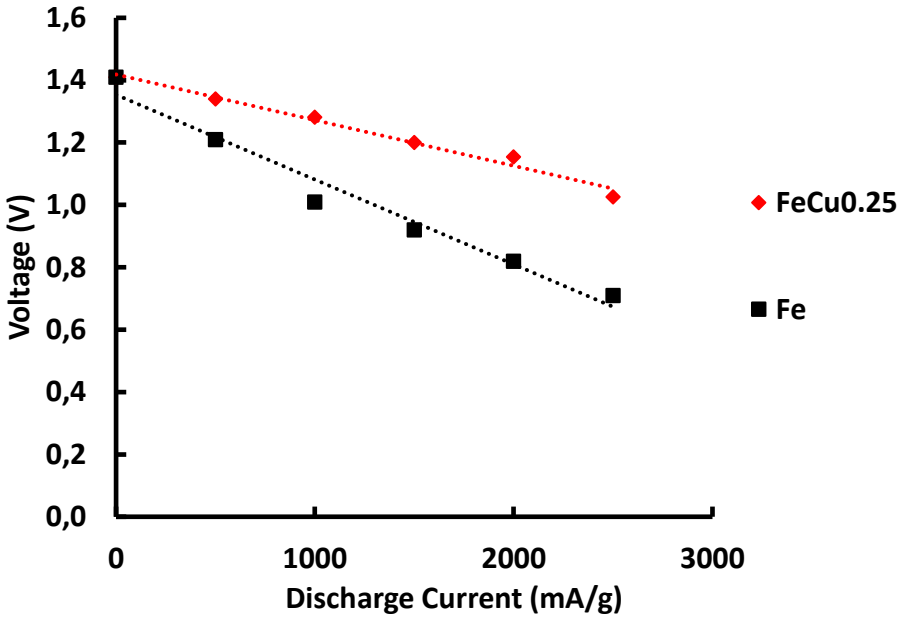

Figure 4-7: Polarization curves of pure Fe electrode and $FeCu_{0.25}$ electrode: the cells were charged at 1000 mA/g for 90 min, and then discharged at the rate ranging from 200 mA/g C to 2500 mA/g for 5 s

It is worth noting that the activation process is a vital step in the development of alkaline Ni-F battery technology. Generally, Fe electrodes suffer from sluggish activation progress in the initial cycles compared to other analogous electrodes (Ni, Zn, Na, Air, Al etc)(Huang *et al.*, 2018). The discharge curve of pure Fe had only one plateau which suggested the conversion of Fe to $Fe(OH)_2$. The capacity was about 90 mAh g^{-1}, significantly lower than the theoretical value for

Fe of 962 mAh g^{-1} (Chakkaravarthy *et al.*, 1991). This large deviation was influenced chiefly by the parasitic hydrogen evolution side reaction and significant particle agglomeration which was confirmed by SEM and in line with observations by Caldas, Lopes & Carlos (1998); Rajan *et al.* (2014) and Wang & Wang (2016).

The discharge curve of $FeCu_{0.25}$ had exhibited only one plateau which suggested the conversion of Fe to $Fe(OH)_2$ (Hang *et al.*, 2006; Kao *et al.*, 2011). The capacity was approximately 340 mAh g^{-1}, significantly higher than the capacity of the pure Fe electrode. The higher capacity was due to the presence of Cu nanoparticles constructing an electron transfer network for the oxidation reaction of Fe to Fe(II) species to proceed. Since $NaBH_4$ acted as the reducing agent, the generation and incorporation of hydrogen into the Fe electrode could, therefore, be expected (Hang *et al.*, 2006; Kao *et al.*, 2011). During the discharge process, hydrogen could react with OH^- to produce water. This reaction may contribute an extra electrical capacity of the electrode (Kao *et al.*, 2011). However, the polarization of $FeCu_{0.25}$ composite electrode (as portrayed in Figure 4-7) is less intense (less ohmic potential drops) compared to that of pure Fe electrode. This is attributed to the ability of Cu particles to construct an electro-conductive network for the redox reactions to progress.

In Figure 4-8, the specific capacities of the electrode materials constituting different quantities of copper were shown up to 40 cycles. The battery was operated between 1.75 V and 0.8 V at a charge and discharge current density of 100mA g^{-1}.

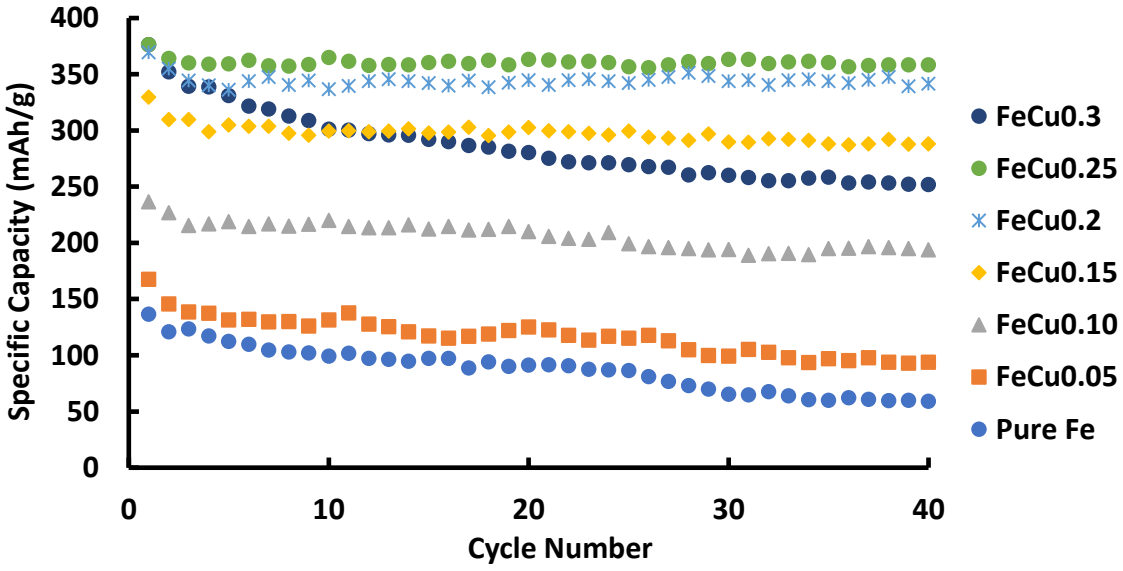

Figure 4-8: Cycling stability curves of pure Fe and various $FeCu_x$ composite electrodes: the cells were charged at 100mA/g to 1.75 V, and then discharged at 100 mA/g C to 0.8 V

The discharge specific capacities of composite electrodes increase gradually with Cu content. The specific capacity of the pure Fe electrode decreased abruptly to around 100 $mAhg^{-1}$ at about 10 charge-discharge cycles. From 10 cycles onwards, the specific capacity of Pure Fe gradually decreases with cycle number. This is due to reduced particle surface area characterised by massive particle agglomeration as noted in SEM images depicted in Figure 4-4.

The highest specific capacity of approximately 360 mAh g^{-1} was attained when the $FeCu_{0.25}$ electrode composite material was employed. The electrode exhibited superlative cycling stability as it retained more than 95% of the initial capacity over 40 cycles. This is attributed to the ability of Cu to prevent particle agglomeration by lowering the particle surface energy through its highly electro-conductive network embedded in the electrode material (Huang *et al*., 2018). When the material was $FeCu_{0.1}$, the effect of Cu content was only minimal and directly comparable to that of the pure Fe electrode. At this stage, the Cu nanoparticles were insufficient to formulate an electron-conducting network to facilitate the oxidation/reduction electrochemical reactions occurring at the electrode. On the other hand, when the Cu nanoparticles content was $FeCu_x$ ($x>0.25$), the Cu nanoparticles might cover the entire Fe particle electroactive surface consequently yielding a low specific capacity (Kao *et al*., 2011).

In an attempt to limit utilisation of high amounts of costly Cu material, the optimum Cu composition was $FeCu_x$ ($x=0.25$), since there was no significant difference between $FeCu_x$ ($x=0.25$) and $FeCu_x$ ($x=0.3$) in terms of electrochemical performance. The nominal specific capacity of 350 mAh g^{-1} (Fe) is a very promising quantity for future applications in large-scale renewable energy storage systems (RESS).

Figure 4-9 displays the Coulombic efficiency of the electrodes containing various amounts of copper. As the fractional copper content increases, the coulombic efficiency increases. This is attributed to the ability of Cu electro-conductive networks ability to amplify reversibility of the Fe(3+)/Fe(2+)/Fe (0) reaction (Dang *et al*., 2011; Paulraj *et al*., 2017). Abdalla *et al*. (2017) highlighted that the presence of Cu increases the overvoltage of the hydrogen evolution consequently effectuating an upswing of the charge efficiency.

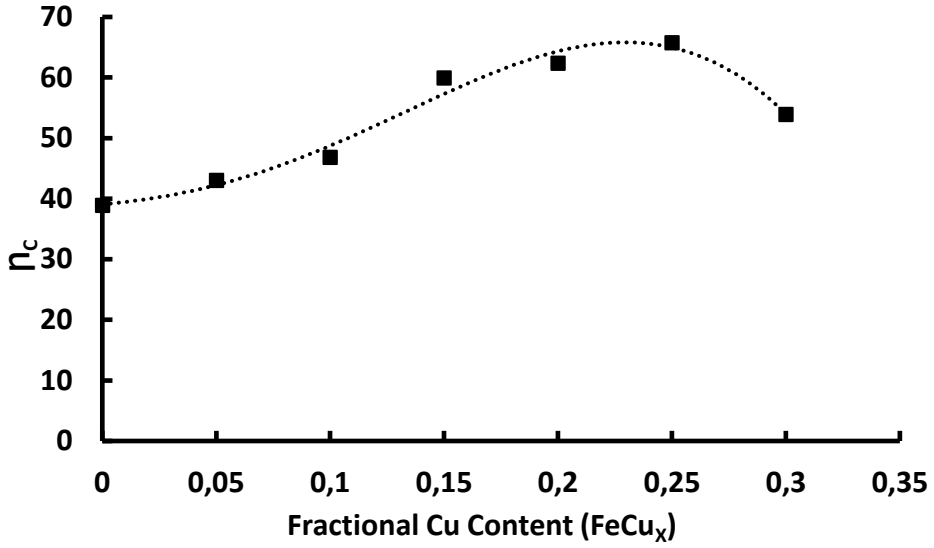

Figure 4-9: Coulombic efficiency of Fe-based electrodes containing various amounts of Cu: The cells were charged at 100mA/g to 1.75 V, and then discharged at 100 mA/g C to 0.8 V

Figure 4-10 depicts the rate capability of $FeCu_{0.25}$ and pure Fe electrode.

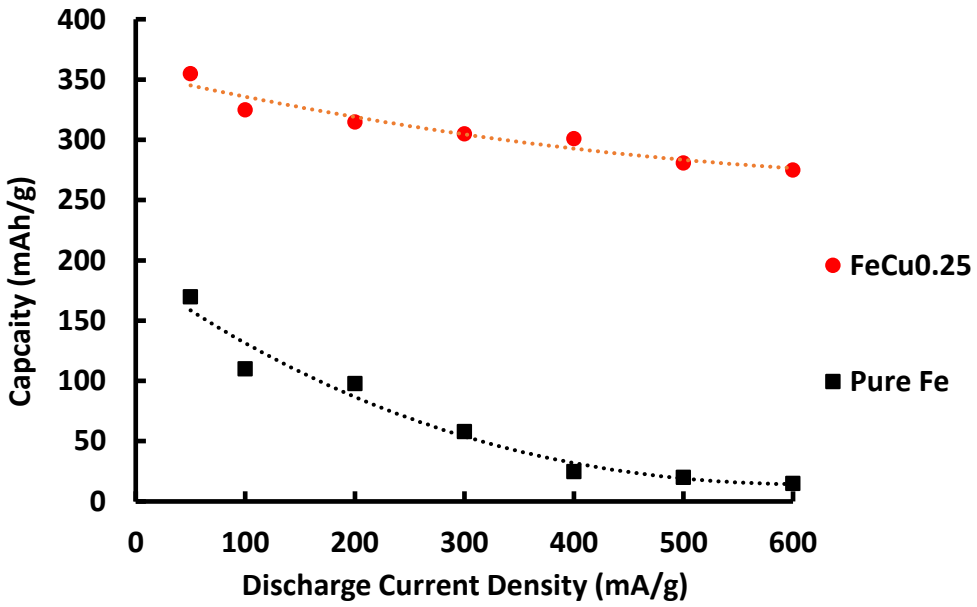

Figure 4-10: Discharge capability at different current densities for Fe and $FeCu_{0.25}$ electrode materials: The cells were charged at 100mA/g to 1.75 V, and then discharged at rates from 50 to 600 mA/g to 0.8 V

The Fe electrode performs poorly at higher discharge rates. This is indicated by the drastic drop in the specific capacity as the current density increases. The $FeCu_{0.25}$ electrode material exhibits the best rate performance even at an impressively high rate of 600 mA g^{-1} and a specific discharge capacity of about 300 mAh g^{-1} is achieved with 85% of the nominal specific capacity

retained. This indicates that the $FeCu_{0.25}$ composite electrode materials have enormous potential as a high-rate electrode material for Fe-based rechargeable batteries. This inimitable high rate discharge capability is attributed to the ability of Cu to improve the electron transfer between Fe particles by constructing a stable electron transfer network (Kao *et al.*, 2011; Paulraj *et al.*, 2017). Generally, the discharge rate capability of the pure Fe electrodes was limited to 600 mA g^{-1} due to the inevitable rampant bulk formation of a $Fe(OH)_2$ passive layer (Kao *et al.*, 2011).

4.3 $FeCu_x$/FeS Electrode Materials: The Effects of FeS

4.3.1 Materials Characterisation

4.3.1.1 X-Ray Diffraction Analysis

Figure 4-11 and Figure 4-12 depicts the XRD patterns of pure Fe and $FeCu_{0.25}$/15%FeS composite electrodes respectively. The different crystal planes in the pattern are identified using the powder diffraction file directory (PDF numbers). The PDFs for Fe, Cu, FeS, C, Fe_3O_4 and Cu_2O are 00-006-0696, 00-004-0836, 00-037-0477, 00-026-1076, 00-019-0629 and 00-0050667 respectively.

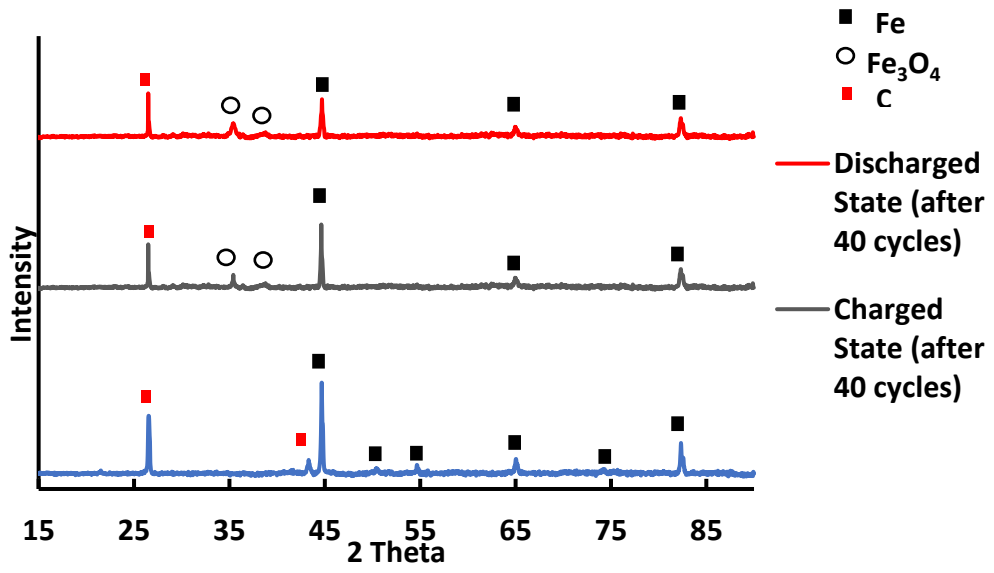

Figure 4-11: XRD patterns for pure Fe electrode

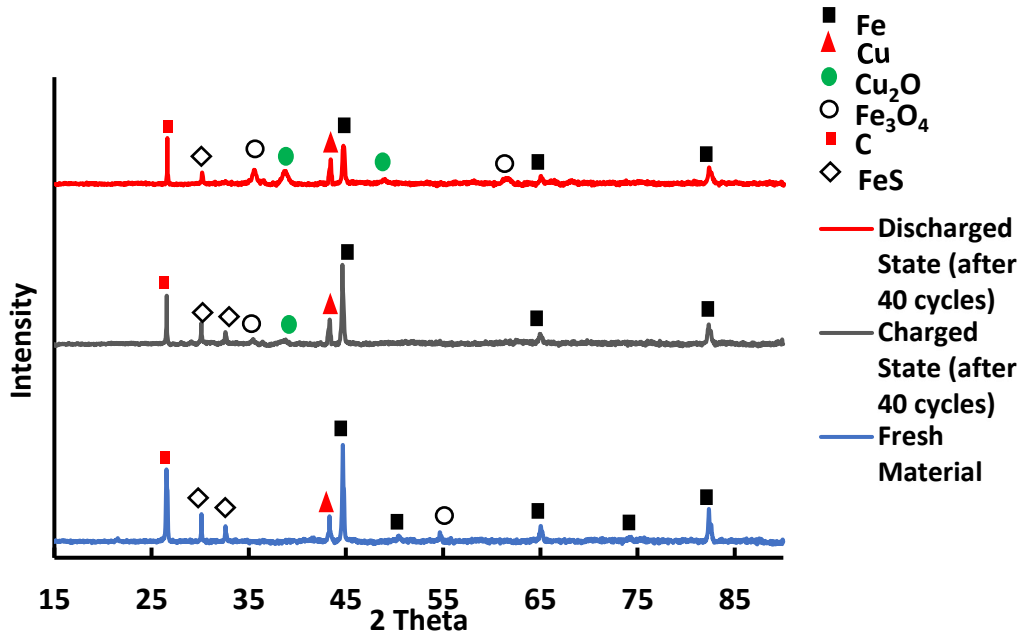

Figure 4-12: XRD patterns for $FeCu_{0.25}$/15%FeS electrode

In Figure 4-11 peaks for Fe and C can be identified for the pure Fe sample. The (110) plane for Fe (maintained in all formulations) occurring at 2θ between 42.5 and 45.4 ^{O} was the dominant facet for Fe. The crystallite size of fresh material particles is approximately 192 nm which decreased to 161 nm (after 40 cycles) due to particle surface passivation (Posada & Hall, 2016; Caldas *et al.*, 1998).

Figure 4-12 shows that the fresh $FeCu_{0.25}$/15%FeS composite has strong peaks of Fe and weaker peaks of Cu which aligns with the ratio of Fe to Cu. When the fresh $FeCu_{0.25}$/15% FeS was deeply discharged, the XRD analysis of the pure Fe material indicated that the peaks of Fe become weaker and the peaks of Fe_3O_4 are observed. This indicates a high utilisation of active material compared to the pure Fe electrode, and the peaks of Fe_3O_4 are much stronger due to the colossal amount of Fe participating in the electrochemical reaction.

In theory, the major product of the discharge process should be $Fe(OH)_2$ which was not detected in the discharged electrode material, suggesting that $Fe(OH)_2$ phase was amorphous. Furthermore, the Cu_2O peak was observed, indicating that some of the Cu was oxidized at a deep discharge state. The average crystallite size of the $FeCu_{0.25}$ particles decreased from 139 to 121 nm after 40-cycles. This is due to the S^{2-} additive's ability to inhibits surface passivation (Caldas *et al.*, 1998). Caldas *et al.* (1998) elucidated that the S^{2-} additive's adsorption onto the Fe-$Fe(OH)_2$ particle structure fosters a distortion that leads to an increase in defect

concentration of the film and consequently, its ionic conductivity increases. Inevitably, this retards the passivation process and formation of a thicker passivation film.

4.3.2 Electrochemical Characterisation

4.3.2.1 Cyclic Voltammetry

Cyclic voltammograms of pure Fe, $FeCu_{0.25}$ and $FeCu_{0.25}$/15%FeS composite electrodes are shown in Figure 4-13.

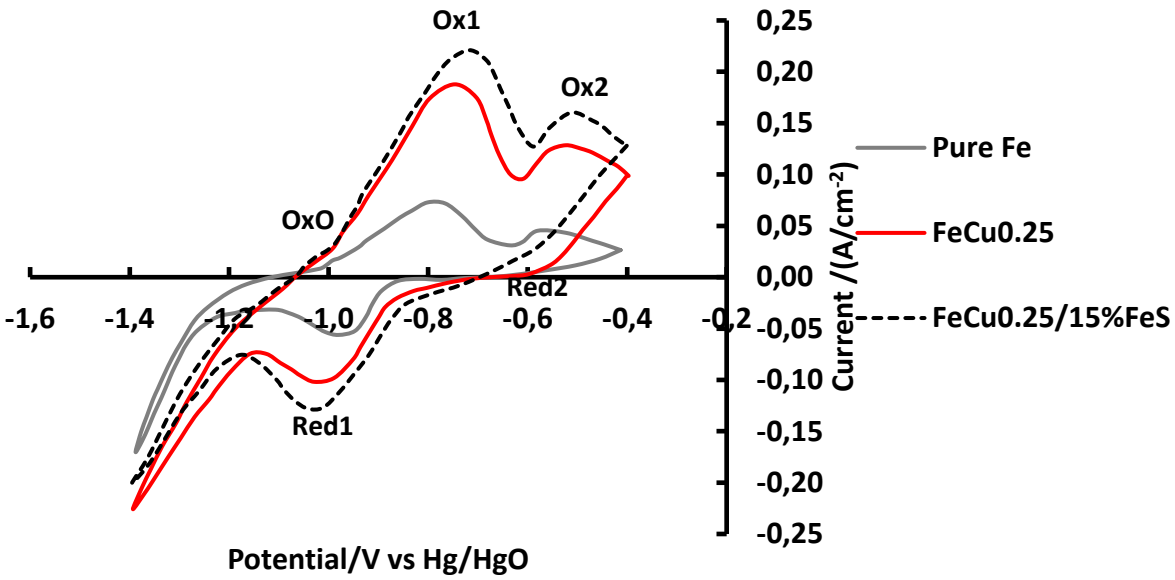

Figure 4-13: Cycling voltammetry of pure Fe electrode, $FeCu_{0.25}$ electrode and $FeCu_{0.25}$/15%FeS electrode in 6M KOH /1M LiOH at 2mV/s.

The voltammograms comprises of three pairs of reduction/oxidation peaks; where the first reduction/oxidation (Ox0/ Red0) peaks can be attributed to the $H_2 \leftrightarrow 2H_2O$ reaction, the second reduction/oxidation (Ox1/Red1) peaks can be attributed to the $Fe(OH)_{ads} \leftrightarrow Fe(OH)_2$ reaction and the third reduction/oxidation (Ox2/Red2) peaks are attributed to the $Fe(OH)_2 \leftrightarrow Fe_3O_4$ reaction (Huang *et al.*, 2018; Paulraj *et al.*, 2017, 2018).

The phenomenon of the elimination of adsorbed hydrogen (Ox0) from the electrode surface during the anodic sweeping has also been observed by the electrochemical quartz crystal microbalance method, confirming the existence of the initial Fe/Fe(II) reaction step (Joiret *et al.*, 2002). The Ox1 reaction is more feasible under the test conditions and appears twice as large as the Ox2 peak which indicates that there is a significantly higher charge associated with

it. However other literature reports have shown a larger or equal sized Ox2 peak compared to the Ox1 peak (Shangguan *et al*., 2015, 2019; Luo *et al*., 2017; Weinrich *et al*., 2017). A possible explanation for the smaller Ox2 peak could be due to partial oxidation which is limited by repulsion from the neighbouring Fe (II) sites. The ratio of the oxidation peaks may also be dependent on the type of Fe material analysed and the type of additives incorporated. The Ox1 peaks exhibit maximum peak heights at – 0.78 V, - 0.75 V and – 0.72 V for the pure Fe, $FeCu_{0.25}$ and $FeCu_{0.25}$/15%FeS electrodes respectively. The Ox2 peaks show maximum peak heights at – 0.56 V, – 0.52 V and – 0.51 V for the pure Fe, $FeCu_{0.25}$ and $FeCu_{0.25}$/15%FeS electrodes respectively.

The addition of Cu shifts the oxidation potentials to slightly lesser negative potentials. This shift implies a lowering in over-potential. It was reported that the oxidation of Cu to Cu_2O takes place at −0.4641 V vs Hg/HgO (Manohar *et al*., 2013; Giri and Sarkar, 2016). In the case of the $FeCu_{0.25}$ electrode, the oxidation of Cu may also exist in parallel with the Fe (II)/Fe (III), though its peak was not distinct due its relatively small amount in the electrode composite.

The Red1 peaks, corresponding to the reduction of Fe (II) to Fe(0), shows maximum peak heights at – 0.98 V, – 1 V and – 1 V for the pure Fe, $FeCu_{0.25}$ and $FeCu_{0.25}$/15%FeS electrodes respectively. No clear peaks on the reduction of Fe_3O_4 to $Fe(OH)_2$ can be observed in all voltammograms, as this reaction would have preceded the $Fe(OH)_2$/Fe reduction peaks (Wang & Wang, 2016; Weinrich *et al*., 2017). However, it cannot be ruled out that the reduction peak is an overlap of both the Fe(III)/Fe(II) and Fe(II)/Fe(0) reduction reactions as these two reduction reactions both occur within a very small potential window (Shangguan *et al*., 2015; Li *et al*., 2017; Luo *et al*., 2017). Following this peak, however, the hydrogen evolution reaction becomes predominant at potentials more negative than – 1.16 V. The pure Fe electrode shows the smallest redox peaks compared the $FeCu_{0.25}$ composite and $FeCu_{0.25}$/15%FeS composite electrodes which indicates a lower ability of the electrode to store charge. The specific capacitance (C_s) were calculated using the following Equation 4-1.

The calculated specific capacitances for the pure Fe, $FeCu_{0.25}$ composite and $FeCu_{0.25}$/15%FeS composite electrodes are 84.7 Fg^{-1}, 233.3 Fg^{-1} and 286.7 Fg^{-1} respectively. Furthermore, higher cathodic current densities are observed with the addition of Cu (from 74 to 188 mA cm^{-2}) which is beneficial for battery operations and utilization at high discharge rates (Paulraj *et al*., 2017). The augmented current density could be attributed to the enhanced electronic conductivity by

the metallic Cu present in the composite material (Huang *et al.*, 2018). The addition of FeS effectuated a further increase in current density to 220 mA cm^{-2} which could be due to the beneficial role of FeS to improve the ionic conductivity of the passivation layer (Shangguan *et al.*, 2015). The sulphide released from the metal sulphide additive attaches to the Fe electrode particles to modify its morphology (Caldas *et al.*, 1998; Hang *et al.*, 2006). This modification restrains the formation of the passive $Fe(OH)_2$ layer, enhancing the bulk conductivity of the Fe electrode and blocking the hydrogen evolution electrochemical process. (Shangguan *et al.*, 2019). It should be noted that the addition of Cu additive also decreases the anodic current density of the hydrogen evolution reaction which is beneficial for the charging process (higher charging efficiency). The addition of the FeS to the $FeCu_{0.25}$ composite has exhibited the ability to lower the hydrogen evolution reaction current density as expected.

4.3.2.2 Galvanostatic Cycling

Figure 4-14 displays the discharge curves of pure Fe, $FeCu_{0.25}$ and $FeCu_{0.25}$/15%FeS composite electrode materials while Figure 4-15 displays the polarization curves of pure Fe, $FeCu_{0.25}$ and $FeCu_{0.25}$/15%FeS composite electrode materials.

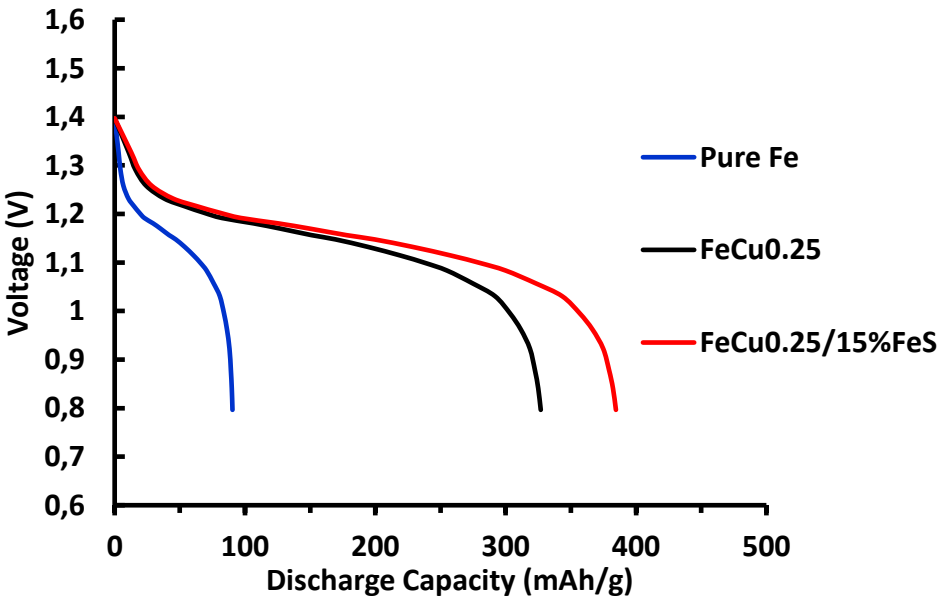

Figure 4-14: Discharge curves of pure Fe electrode, $FeCu_{0.25}$ electrode and $FeCu_{0.25}$/15%FeS electrode: The cells were charged at 100mA/g to 1.75 V, and then discharged at 100 mA/g C to 0.8 V

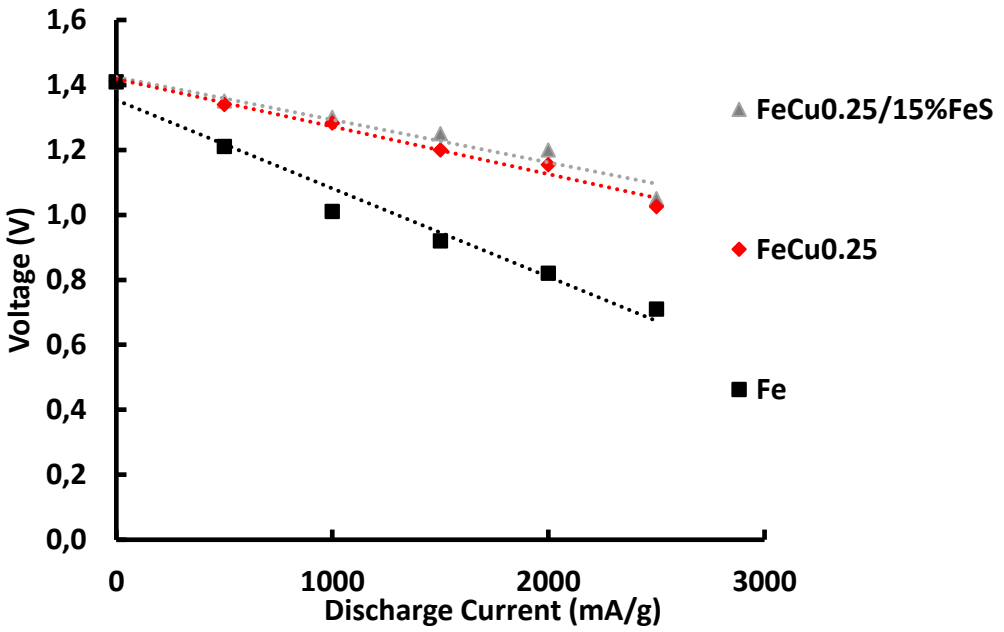

Figure 4-15: Polarization curves of pure Fe, $FeCu_{0.25}$ and $FeCu_{0.25}$/15%FeS electrodes: the cells were charged at 1000 mA/g for 90 min, and then discharged at the rate ranging from 200 mA/g C to 2500 mA/g for 5 s

It is noteworthy that the formation/activation process is a fundamental step in a secondary alkaline battery system. Generally, Fe electrodes always suffer from slow activation progress in the first cycles compared to other analogous electrodes (Ni, Zn, Na, Air, Al etc) (Huang *et al.*, 2018). The discharge curve of pure Fe had only one plateau which suggested the conversion of Fe to $Fe(OH)_2$. The capacity was about 90 mAh g^{-1}, significantly lower than the theoretical value for Fe of 962 $mAhg^{-1}$ (Kao *et al.*, 2011). This large deviation was influenced chiefly by the parasitic hydrogen evolution side reaction and significant particle agglomeration (Caldas *et al.*, 1998; Rajan *et al.*, 2014; Wang & Wang, 2016). The discharge curve of $FeCu_{0.25}$ had exhibited only one plateau which suggested the conversion of Fe to $Fe(OH)_2$ (Hang *et al.*, 2006; Kao *et al.*, 2011) The capacity was about 380 mAh g^{-1}, significantly higher than the capacity of pure Fe electrode. The higher capacity was due to the presence of Cu particles constructing an electron transfer network for the oxidation reaction of Fe to Fe(II) species to progress. The discharge curve of $FeCu_{0.25}$/15%FeS had exhibited only one plateau which suggested the conversion of Fe to $Fe(OH)_2$ (Kao *et al.*, 2011; Huang *et al.*, 2018). The capacity was about 380 mAh g^{-1}, slightly higher than the capacity of $FeCu_{0.25}$ electrode. The slightly higher capacity was due to the presence of FeS that aids in circumventing the hydrogen evolution reaction and enhancing bulk electrode conductivity, consequently the electrode accepts and transports

more charge. Figure 4-15 showed the polarization curves of Fe, $FeCu_{0.25}$ and $FeCu_{0.25}$/15%FeS composite electrode materials. As the current densities are increased, the polarization becomes intensified. However, as represented in Figure 4-15, the polarization of $FeCu_{0.25}$ composite electrode (which co-aligns with polarization curve of the $FeCu_{0.25}$/15%FeS electrode) is less intense (less ohmic potential drops) compared to that pure Fe electrode. This is attributed to the ability of Cu particles to construct an electro-conductive network for the redox reactions to progress.

In Figure 4-16, the specific capacities of the $FeCu_{0.25}$ electrode materials containing different amounts of FeS were depicted.

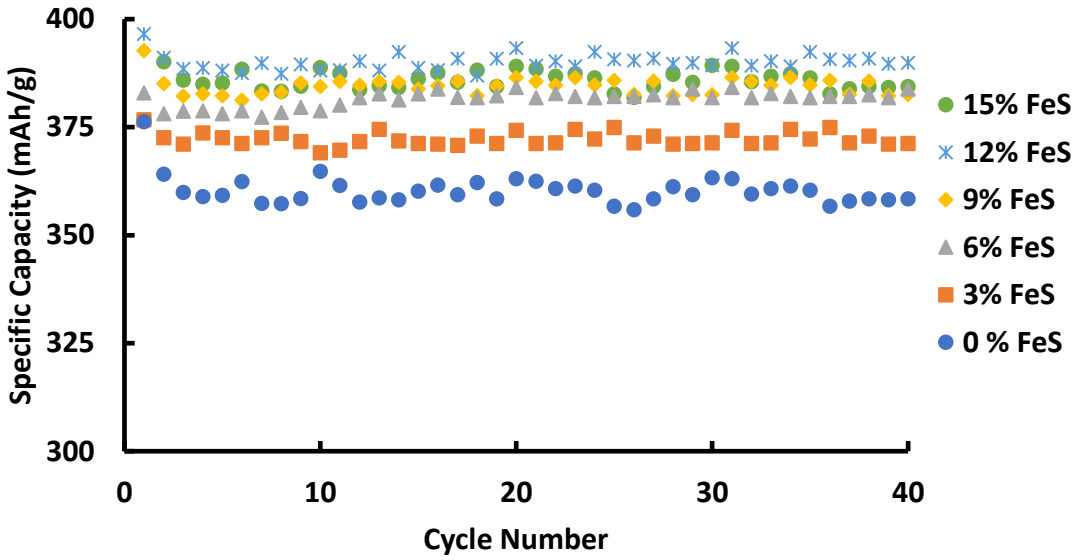

Figure 4-16: Specific capacity versus % FeS Content in $FeCu_{0.25}$ electrode material: The cells were charged at 100mA/g to 1.75 V, and then discharged at 100 mA/g C to 0.8 V

In Figure 4-17, the specific capacities (recorded at the 10^{th} cycle) of the $FeCu_{0.25}$ electrode materials containing different amounts of FeS were depicted.

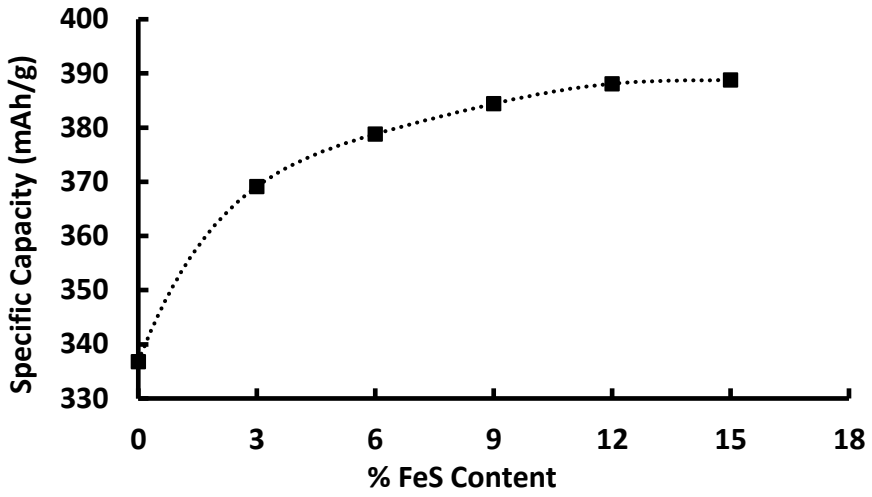

Figure 4-17: 10th cycle specific capacity versus % FeS Content in $FeCu_{0.25}$ electrode material : The cells were charged at 100mA/g to 1.75 V, and then discharged at 100 mA/g C to 0.8 V

The discharge capacities composite electrodes increase gradually with FeS content up until it stagnates at 12% FeS. The highest (optimal) specific capacity of around 390 mAh g^{-1} was attained when 15% FeS was incorporated into the $FeCu_{0.25}$ electrode composite material. As % FeS content increases, the specific capacity increases up until capacity stabilization at FeS composition greater than 12%. The linear correlation between % FeS content and specific capacity is attributed to the ability of FeS to partake in the electrochemical reaction and its ability to distort the $Fe(OH)_2$ structure which leads to an increase in defect concentration in the passivation film consequently increasing its ionic conductivity (Caldas *et al.*, 1998; Hang *et al.*, 2006; Posada & Hall, 2016). The capacity stagnates at FeS content greater than 12%. Posada *et al*. (2017) asserted that at higher concentrations (>20%) the capacity drastically drops, nevertheless, the effect is not completely understood. Figure 4-18 displays the Coulombic efficiency of the charge/discharge process for electrodes containing various amounts of FeS.

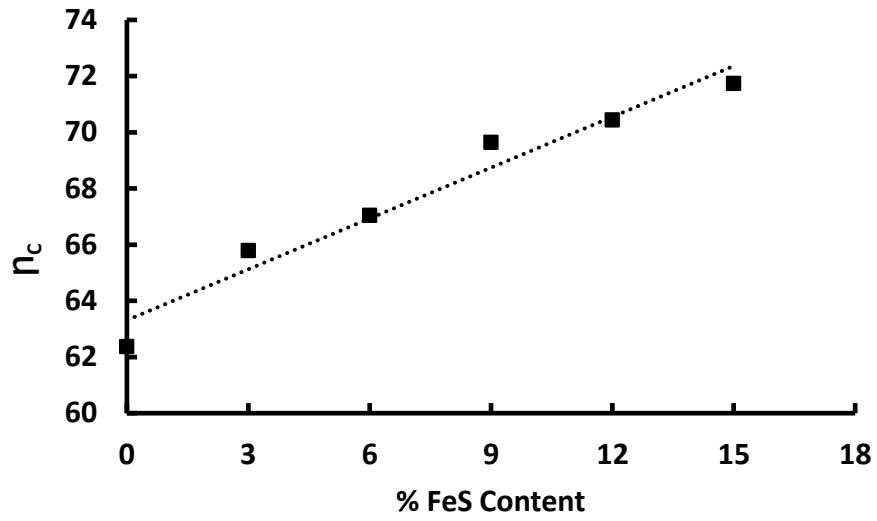

Figure 4-18: Coulombic efficiency versus % FeS content in $FeCu_{0.25}$ electrode material: The cells were charged at 100mA/g to 1.75 V, and then discharged at 100 mA/g C to 0.8 V

As % FeS content increases, the coulombic efficiency increases, this is attributed to the ability of FeS to increase the overvoltage of the hydrogen evolution reaction. Efficiency of 71% was attained when the electrode formulation of 15% FeS in $FeCu_{0.25}$ electrode material was employed; however, it has been reported that higher FeS (>15%) tend to shorten the life of the battery thus in our work our cut off value was 15% (Caldas *et al*.,1998; Hang *et al*., 2006; Abdalla *et al*., 2016; Wang & Wang, 2016). The high charge and coulombic efficiency induced by FeS through amplified reversibility and curbing hydrogen evolution reaction are due to the adsorption of the highly polarizing S^{2-} ion on Fe-$Fe(OH)_2$ particles (Hang *et al*., 2006). Carta *et al*. (1988) claimed that the hydrogen molecular recombination reaction (Equation 1-1) was inhibited by S^{2-} ion chemisorption. Hang *et al*. (2006) highlighted that another influential factor is the change of surface species prompting the overpotential of the hydrogen evolution reaction.

4.4 $FeCu_x$/FeS/AC Electrode Materials: The Effects of Ammonium Carbonate

4.4.1 Electrochemical Characterisation

4.4.1.1 Galvanostatic Cycling

In Figure 4-19, the capacities of the $FeCu_{0.25}$/15%FeS electrode materials constituting different amounts $(NH_4)_2CO_3$ were shown up to 40 cycles. The battery was cycled between 1.75 V and 0.8 V at a current density of 100 mA g^{-1}.

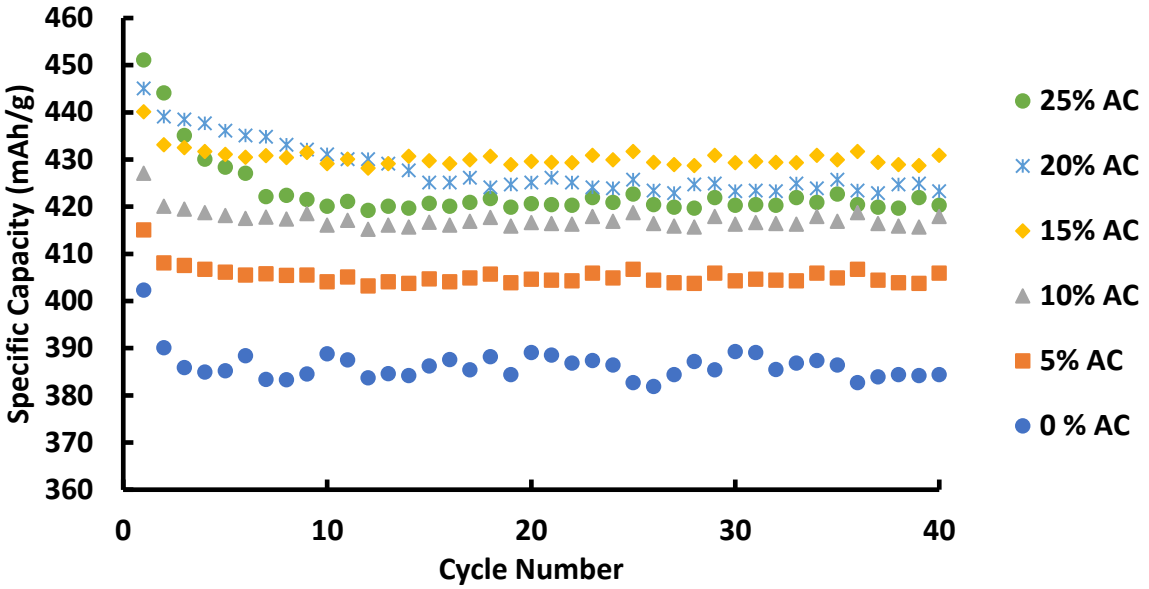

Figure 4-19: Cycling stability of $FeCu_{0.25}$/15%FeS composite electrodes with different amounts of AC: the cells were charged at 100mA/g to 1.75 V, and then discharged at 100 mA/g C to 0.8 V

From the graph, the linearity between specific capacity and $(NH_4)_2CO_3$ is evident. However, at concentrations higher than 15%, the capacity starts decreasing likely caused by the observed electrode material deterioration (material falling off from electrode). This deterioration is attributed to the highly porous structure which compromises the mechanical integrity of the electrode. The highest (optimal) specific capacity of approximately 430 mAh g^{-1} was attained when the 15% $(NH_4)_2CO_3$ was integrated into the $FeCu_{0.2}$/15%FeS material. In order to increase the electrode active area (void spaces) in contact with the electrolyte solution, $(NH_4)_2CO_3$ was incorporated into the active mass before hot-pressing. When the temperature reaches ~70 ^{O}C the $(NH_4)_2CO_3$ decomposes into NH_3, CO_2 and H_2O according to the equation:

$$(NH_4)_2CO_3 \rightarrow CO_3 + 2NH_3 + H_2O \qquad [4\text{-}2]$$

The evolution of the NH_3 and CO_2 gases unlocks porous channels and consequently, both porosity and surface area of the active material in contact with the electrolyte increases. The effect of $(NH_4)_2CO_3$ concentration on the electrode's porosity is depicted in Figure 4-20.

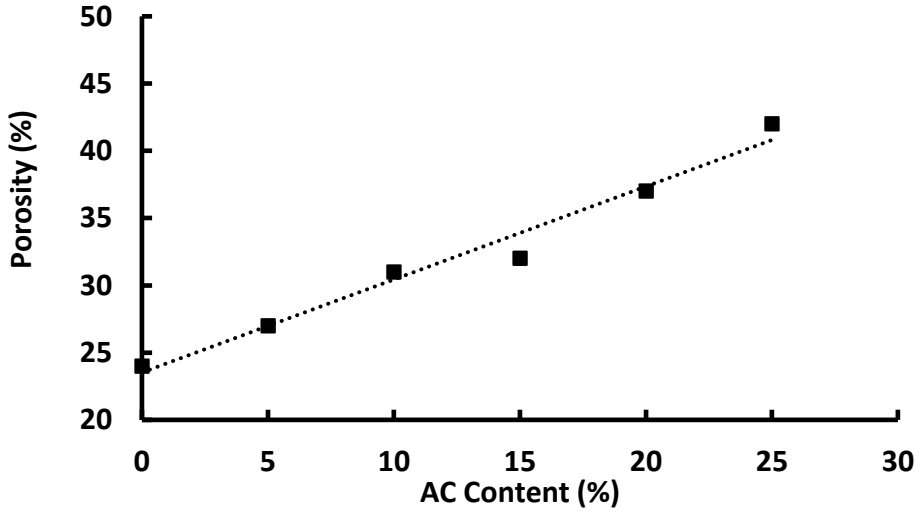

Figure 4-20: Influence of $(NH_4)_2CO_3$ on the electrode porosity

4.5 Bipolar Ni-Fe Prototype

A polypropylene casing with the design depicted in Figure 4-21 was employed to construct the test cell. The test cell was only employed to quantify requisite parameters necessary to obtain an unmitigated characterisation of the electrodes. The production of a single bipolar Ni-Fe battery was studied in this section using the optimum formulation $FeCu_{0.25}$/15%FeS/15%AC for the negative electrode material synthesis. Commercial NiOH electrode material was utilised as the positive electrode. The electrolyte concentration was 6M KOH and 1M LiOH. The bipolar Ni-Fe battery was produced as a prototype for commercialisation purposes.

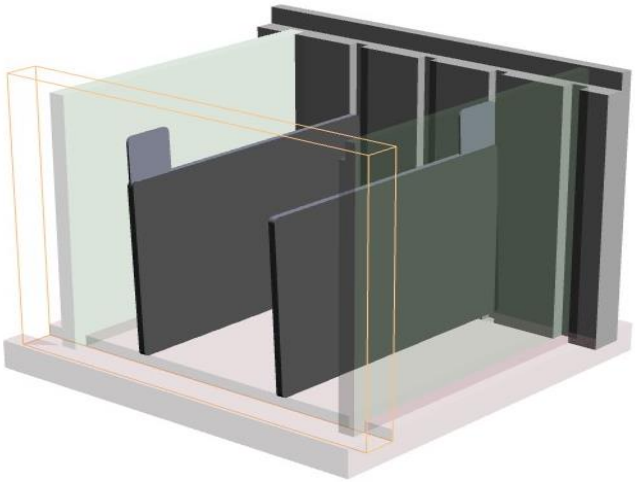

Figure 4-21: 3D conception of the test cell with two electrodes

The bipolar Ni-Fe design exploits an innovative combination of optimised battery components and design in conjunction with the application of novel mass-production techniques (Fraunhofer UMSICHT, 2019). Fraunhofer UMSICHT (2019) highlighted that by employing the bipolar battery design, it is possible to save over 75% of conventional battery materials such as electrolyte, insulating material, cables. The replacement of Ni-mesh using corrosion-free electro-conductive polymer film (bipolar plate) bipolar plate offers a more cost-effective alternative solution.

In the project, in cooperation with Fraunhofer UMSICHT and Volterion GmbH technology partners, the development and optimisation of the individual components and the production of individual battery cells were addressed, and this knowledge acquired was utilised to assemble a bipolar Ni-Fe prototype. The 25 Wh (5.25 Ah/4.8 V) prototype in the bipolar design was constructed and examined. The successful construction of the bipolar battery demonstration should pioneer a new generation of powerful and cost-effective storage batteries. The In-house produced 25Wh bipolar Ni-Fe battery prototype is depicted in Figure 4-22. However, information on the bipolar Ni-Fe battery cannot be disclosed due to disclosure limitations as agreed with the involved parties.

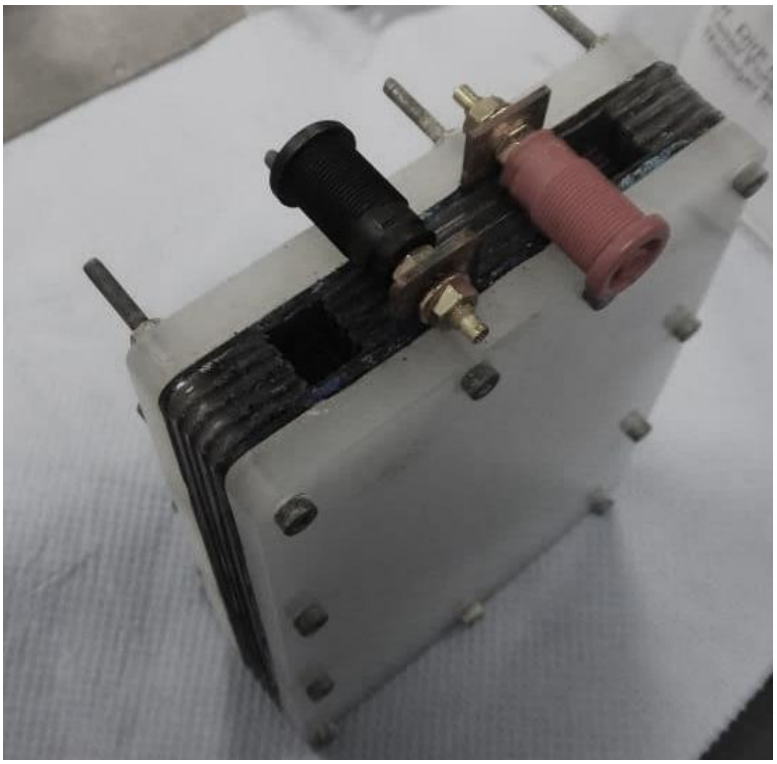

Figure 4-22: Laboratory prototype of a 25 Wh bipolar Ni-Fe battery in DIN A6 format

4.6 Material and Energy Balance

4.6.1 Material Balance

The effect of different parameters and components involved in the synthesis of electrode material was demonstrated and the findings revealed that the utilization of a specific composite electrode formulation in order to improve battery performance depends on the application of the battery in the energy storage industry. Thus, certain constraints imposed by physics need to be considered when developing a new process like the one executed in this study. The material balance is a prerequisite to account for the input raw material and final products. In other words, material balance is the application of the law of conservation of mass which states that mass in an isolated system can neither be created nor destroyed. Figure 4-23 outlines the boundary of the overall material balance of a single bipolar Ni-Fe battery production. All the calculations were done at steady state meaning mass entering the system equals mass leaving the system.

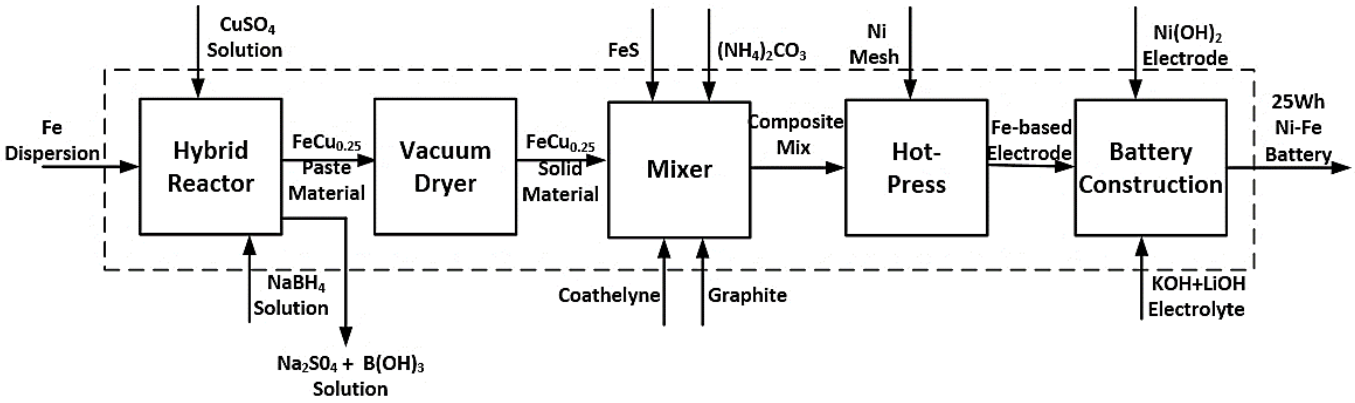

Figure 4-23: Material flowsheet adopted during bipolar Ni-Fe battery production

The evaluation of material balance was done based on $FeCu_{0.25}$ composite electrode material synthesized using 60g of Fe. The paste material was dried using a vacuum dryer. The dried composite material was mixed with 15% FeS, 15% AC,5% CA and 5% Graphite. The composite material was hot-pressed on a bipolar plate and coupled with $Ni(OH)_2$ electrode and KOH/LiOH electrolyte together with other minor requisite components to produce a bipolar Ni-Fe battery.

Figure 4-24 shows the input and output components involved in the synthesis of bipolar Ni-Fe batteries.

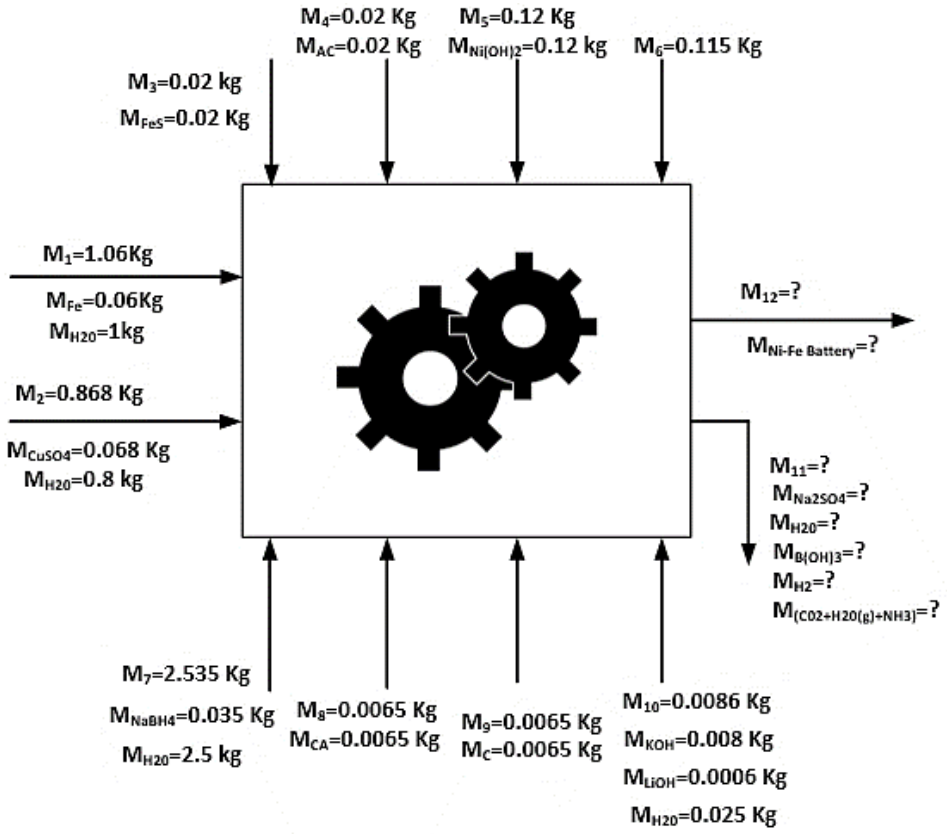

Figure 4-24: Overall mass balance around the bipolar Ni-Fe battery production process

Where:

M = the total mass of components.

The general material balance equation:

Accumulation = input– output + generation - consumption

The **assumptions** made in the calculations were:

The system is at steady state, accumulation = 0

Input + generation = Output + Consumption

$$M_1+M_2+M_3+M_4+M_5+M_6+M_7+M_8+M_9+M_{10}=M_{11}+M_{12}$$

Since Fe was in excess, conversion, X_{CuS04} = 0.99

Since the generation of components in M_{11}, the determination of M_{11} is limited only to the hybrid reactor.

Thus; for M_{11}

$$Fe+[6H_2O+CuSO_4+2NaBH_4 \rightarrow Na_2SO_4+2B(OH)_3+4H_2+Cu] \quad [4\text{-}3]$$

Since 0.044 Kg (0.272 moles) of $CuSO_4$ is the limiting reagent, thus;

$$M_{11(Na_2SO_4)}=\nu_{Na_2SO_4} X_{CuSO_4} N_{CuSO_4} Mr_{(Na_2SO_4)}$$
$$=1\times 0.99\times 0.27\times 142$$
$$=38g\ (0.038\ kg)$$

$$M_{11(B(OH)_3)}=\nu_{B(OH)_3} X_{CuSO_4} N_{CuSO_4} Mr_{(B(OH)_3)}$$
$$=2\times 0.99\times 0.27\times 61.83$$
$$=33g\ (0.033\ kg)$$

$$M_{11(H_2)}=\nu_{H_2} X_{CuSO_4} N_{CuSO_4} Mr_{(H_2)}$$
$$=4\times 0.99\times 0.27\times 2$$
$$=2.2\ g\ (0.0022\ kg)$$

$$M_{11(H_2O)}=M_{1(H_2O)}+M_{2(H_2O)}+M_{7(H_2O)}+M_{10(H_2O)}-\nu_{H_2O} X_{CuSO_4} N_{CuSO_4} Mr_{(H_2)}$$
$$=4325\text{-}(6\times 0.99\times 0.27\times 18)$$
$$=4296g\ (4.296\ kg)$$

$$M_{11(CO_2+NH_3+H_20(g))}=M_{4(AC)}$$
$$=0.02\ kg$$

$$M_{11}=M_{11(H_2O)}+M_{11(H_2)}+M_{11(Na_2SO_4)}+M_{11(B(OH)_3)}+M_{11(CO_2+NH_3+H_20(g))}$$
$$=4296+2.2+38+33+20$$
$$=4489\ g\ (4.489\ kg)$$

Therefore;

$$M_{12}=M_1+M_2+M_3+M_4+M_5+M_6+M_7+M_8+M_9+M_{10}-M_{11}$$
$$=1.06+0.855+0.02+0.02+0.12+0.115+2.515+0.004+0.0086\text{-}4.489$$
$$=0.563\ kg$$

The overall material balance of the Bipolar Ni-Fe battery was shown in Figure 4-24. The actual total mass of the bipolar Ni-Fe battery of 0.545 kg which corresponds to M_{11}. The theoretical and actual total mass of bipolar Ni-Fe is 0.563 and 0.545 kg, respectively. The difference observed here was due to the mass loss throughout the synthesis, the lost weight percentage was calculated as follows:

$$\text{Total Mass lost } \% = \frac{M_{theoretical} - M_{actual}}{M_{theoretical}} \times 100$$
$$= \frac{0.563 - 0.545}{0.563} \times 100$$
$$= 3.2\ \%$$

The 3.2% weight was lost mostly during the mixing and moulding stages throughout the production process, where the starting materials changed states from slurry to a paste, this means that the loss in weight could be attributed to some material that remained attached to the mixing or oven unit wall. Therefore, the material balance demonstrated that the production of bipolar Ni-Fe bipolar battery recovered 96.8% weight of the starting material. Therefore, it could be said that this process was performed successfully, and no waste was generated. The law of conservation of mass was observed, this is evident as the amount of the final product weighed was approximately equal to the amount of the feed.

4.6.2 Energy Balance

The formulations and conditions developed in this work were made possible due to the utilisation of equipment such as the mixer, hydraulic press and oven. The energy balance is a prerequisite to account for the utilised during the production process. Energy balance is the application of the law of conservation of energy which states that energy in an isolated system can neither be created nor destroyed. The equipment employed was operating on electrical power. Therefore, the quantification of energy utilised as a prerequisite is essential in order to effectively run the bipolar Ni-Fe battery production process. The energy consumed by the mixing unit, hydraulic press and vacuum oven was determined using real-time measurements of the current and voltage during operation.

Thus, the results obtained in the following sub-section are based on the actual readings observed as described above.

The boundaries around which the energy was determined is depicted in Figure 4-25

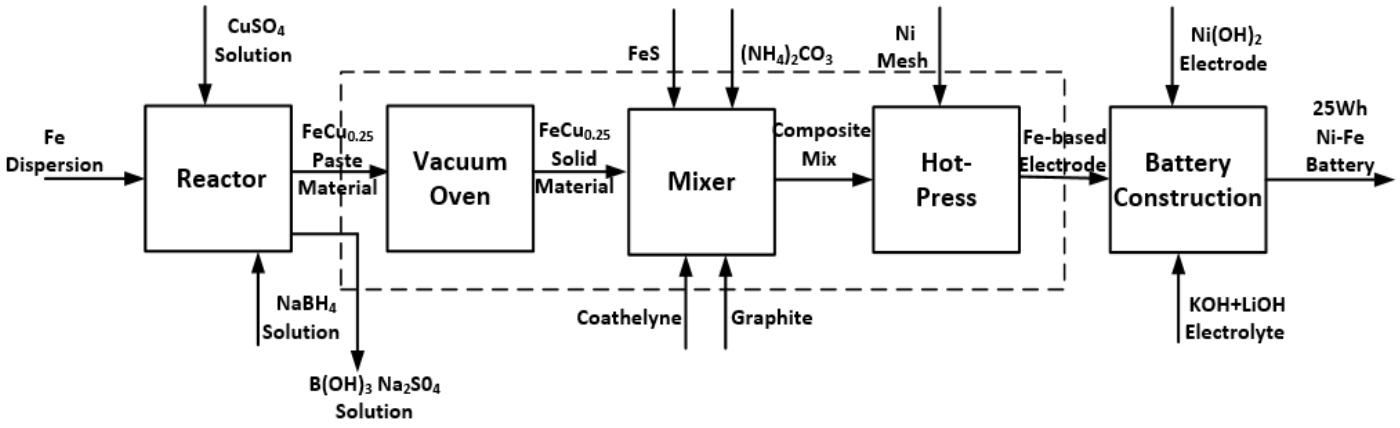

Figure 4-25: Energy balance around the mixer, hot-press and oven for the bipolar Ni-Fe battery production

Energy Consumed by the Mixing Unit

The type of mixer used in this study was a laboratory-scale anchor agitator with a motor with the details provided in Table 4.8. The energy consumed by the mixer was determined during the mixing 0.078 Kg of $FeCu_{0.25}$ with 0.02 Kg of FeS, 0.02 Kg of AC, 0.0065 Kg of CA, and 0.0065 kg of Graphite for a total time of 15 minutes.

Table 4-1: Mixer specifications

Variable	Unit	Value
Dimensions (W*L*H)	mm	120/150/205
Drum Diameter	mm	110
Anchor Diameter	mm	60.5
Electric motor (230/50Hz)	kW	0.3
Paddle Speed	rpm	100
Running Current	A	1
Drum Capacity	L	2
Mixing Performance	L	48

The power required was calculated using the Equation 4-3 below.

$$P = VI \quad [4\text{-}4]$$

$$\begin{aligned} P &= V \times I \\ &= 120 \times 1.5 \\ &= 150 \text{ W} \end{aligned}$$

The motor efficiency (η) was assumed to be 75%.

$$P_e = P\eta \quad [4\text{-}5]$$

$$P = \frac{Pe}{n}$$

$$P = \frac{150}{0.75} = 200W = 0.2kW$$

Therefore, the power required was used to determine the electrical consumption.

The mixing unit was used for a total time of 15 minutes which is equivalent to 900 seconds (s), the energy consumed by the motor was calculated as follows:

$$Q = P_e t \quad [4\text{-}6]$$

$$\begin{aligned} Q &= P_e \times t \\ &= 0.2 \times 900 \\ &= 180 \text{ kJ} \end{aligned}$$

The motor energy used was found to be 180 kJ for 95 g of the starting materials and after 15 minutes of mixing. The speed of the mixer (100 rpm) was adequate to produce homogeneous composite material.

Energy Consumed by the Oven

The power used by the oven during drying was determined using the average real-time voltage and current of 220.5 V and 3.2 A, respectively. These readings were recorded during the drying of $FeCu_{0.25}$ wet material. The material was vacuum dried for 60 hours at 30 degrees Celsius. Therefore, the power used by the oven was determined as follows:

$P = V \times I$

$= 220.5 \times 3.2$

$= 0.705$ kW

72 hours drying =259 200s

Energy used for drying

$Q = 259200 \times 0.705 = 182\ 736$ kJ

The oven consumed a lot of energy compared to the mixing unit and hydraulic press, this observation was due to the difference in current that these two units of equipment used.

Energy Consumed by the Battery Management System

The power used by the BMR during battery testing was determined using the real-time voltage and current of 5 V and 1 A, respectively. These readings were recorded during the testing of batteries. The equipment was operated for 24 hours at 25 degrees Celsius. Therefore, the power used by the BMS was determined as follows:

$P = V \times I$

$= 50 \times 200$

$= 10$ kW

10 hours drying =36 000s

Energy used for testing

$Q = 36\ 000 \times 10 = 360\ 000$ kJ

The BMR consumed a lot of energy compared to the other units, this observation was due to the difference in current that these two units of equipment used.

Energy Consumed by the Hot-Press

The power used by the hot-press during curing was determined using the real-time voltage and current of 150.5 V and 3.5 A, respectively. These readings were recorded during the pressing of composite material on the bipolar sheet. The material was hot-pressed for 50 minutes at 105 °C. Therefore, the power used by the hydraulic press was determined as follows:

$$P = V \times I$$
$$= 150.5 \times 3.2$$
$$= 0.526 \text{ kW}$$

50 minutes of hot pressing =3000s

Energy used for curing

$Q = 3000 \times 0.526 = 158$ kJ

The total amount of energy consumed in the production process was estimated to be the sum of the energy consumed by the oven, hydraulic press and that of the mixing unit. This was determined as follows:

$$Q = Q_{mixer} + Q_{hydraulicpress} + Q_{dryer} + Q_{BMS}$$
$$= 180 + 182736 + 150 + 360000$$
$$= 543 \text{ MJ}$$

The process used total energy of 543 MJ to make a single bipolar Ni-Fe battery.

4.7 Cost Evaluation

4.7.1 Overview

In this section, the cost involved in the bipolar Ni-Fe battery constructed using electrode formulation $FeCu_{0.25}$/15%/FeS/15%AC was investigated. The calculations embodied included the cost of raw materials, utilities, labour costs, the cost of Ni-Fe batteries per watthour (Wh) and cash flow statement for a plant with a capacity of 2600 batteries/year.

4.7.2 Energy Production Cost of a Plant Capacity of 2600 Batteries/Year

In this section, the production cost of a plant capacity of 2600 Ni-Fe batteries/year is determined. The calculations included the cost of raw materials, energy consumption (by the oven, hydraulic press and oven), operating labour and the cost of Ni-Fe batteries per kilowatt-hour during the battery production process.

In Table 4-2 the cost of raw materials utilised to construct a 25 Wh Ni-Fe battery is tabulated.

Table 4-2: Raw materials cost estimation of a single bipolar Ni-Fe battery

Raw Materials	Amount [Kg]	Cost [R/Kg]	Actual Cost [R]
NiOH	0.1200	550	66.00
Fe	0.0600	62	3.72
FeS	0.0200	75	1.50
NH_4CO_3	0.0200	15	0.30
Graphite	0.0065	10	0.07
Coathelyne	0.0065	22	0.14
Minor Components	0.1150	50	5.75
KOH	0.0080	390	3.12
LiOH	0.0006	310	0.19
DI H_2O	4.3250	1.25	5.41
$NaBH_4$	0.0350	282	9.87
$CuSO_4$	0.0680	50	2.75
Total Mass[Kg]	4.7166	**Total Cost [R]**	99.46

The mass of the bipolar Ni-Fe battery was 563 g (determined in Section 4.6.1), 10 batteries could be produced per batch or day) which was the rate of production of Ni-Fe batteries in this study. In addition, all the calculations involved in this section (cost of production of Ni-Fe batteries) were determined using formulas and procedures reported by Apostolakou *et al*. (2009). Thus, the calculated cost of production of 10 Ni-Fe batteries per year or 5.36 kg per day (where 12 months are equivalent to 260 working days) was investigated in this section. This implied that 2600 batteries/year was the plant capacity of the Ni-Fe batteries production.

It was relevant to determine how much money was spent per year using the production rate of 10 Ni-Fe batteries/day. Thus, the cost estimation was carried out as shown next. The cost estimation was initiated by determining the fixed capital investment at the plant capacity of 2600 batteries/year. Fixed capital investment is a vital parameter in computing the production cost, as it estimates the cost of acquisition and maintenance of long-term major equipment utilised in the bipolar Ni-Fe battery production process. Table 4-3 presents the sum of installed equipment cost (SIEC), total installed equipment cost (TIEC) and fixed capital investment (FCI).

Table 4-3: Cost of major equipment utilised in the production of Ni-Fe batteries (2600 batteries/year)

Equipment & Size	**Price [R]**	**Supplier**
Hydraulic Press (Pressing Plate 30cm X 30 cm)	76 000	Hyjack, Cape Town
Vacuum Oven (400L)	24 000	Labotec
Battery Management System (50 Channels)	44 000	NEWARE
Mould (9 cm x 6 cm)	500	WAKE Enginnering
Overheard Mixer (40cm)	16 000	Labotec
Sum of installed equipment	160 500	
Total installed equipment cost	192 600	
Fixed Capital Investment	385 200	

The calculations were carried out as follows:

$$\text{TIEC} = 1.2 \times \text{SIEC} = 1.2 \times 160\,500 = \text{R}192\,600$$

$$\text{FCI} = 2 \times \text{SIEC} = 2 \times 192\,600 = \text{R}385\,200$$

The fixed capital investment of R385 200 was used to determine the production cost of Ni-Fe batteries. The cost of raw materials/cell was estimated in Table 4-2. The cost of Raw materials per year was calculated as R258 596 (R99.46/battery × 2600 batteries).

Then, the cost of utilities was estimated as shown below:

In the present study, the cost of utilities consisted of the cost of electricity. The energy consumed during the electrode production process was estimated from the equipment's specifications (mixer, hydraulic press, BMS and vacuum dryer). The mixer consumed 0.2 kW, it was used for 1 hour, and the rate of power was 0.2 kWh per day. The BMS consumed 10kW, it was used for 10 hours, and the rate of power was 100 kWh per day. The oven consumed 0.705 kW, it was used for 24 hours, and the rate of power was 16.9 kWh per day. The hydraulic press consumed 0.526 kW, it was used for 4 hours, and the rate of power was 2.1 kWh per day. The rate of electricity in South Africa is 89.13c per kWh (R0.89).

(Source:http://www.capetown.gov.za/Family%20and%20home/residential-utility-services/residentialelectricity-services/the-cost-of-residential-electricity, Accessed on the 20th April 2019).

Table 4-4 presents the estimation cost of utilities per year.

Table 4-4: Estimation cost of the plant utilities per year (plant with capacity 2600 batteries/year)

Equipment & Size	**KWh/day**	**KWh/Year**	**Rand/Year**
Hydraulic Press	2.1	546	485
Vacuum Dryer	16.9	4 400	3 916
Overheard Mixer	0.2	52	47
Battery Management System	100	26 000	23 140
		Total	27 588

Thereafter, the operating labour cost was estimated as shown below.

Two operators were running the battery production process. During this process, the operator was working for 5 hours per day which was equivalent to 1300 hours per year. Each operator was earning R43.05 per hour which was the PayScale for a production operator in South Africa.

(Source: https://www.payscale.com/research/ZA/Skill=Machine_Operation/Hourly_Rate, Accessed on the 20th October 2019).

Thus, Table 4-5 shows the operating labour cost.

Table 4-5: Operating labour cost for 1300 hours per year using a plant capacity for Ni-Fe batteries at a rate of 2600 batteries/year

Cost Item	**R/hr**	**R/Year**
Operator 1	43.05	55 900
Operator 2	43.05	55 900
	Total cost	111 800

Table 4-5 showed that a production operator working on the manufacturing of Ni-Fe batteries received R55 926 per year. Since two operators were working at the pilot plant; therefore, R 111 852 was the operating labour cost. Thus, the total production cost of Ni-Fe batteries was estimated in the next section (Table 4-6).

Table 4-6: Manufacturing cost estimation for production of Ni-Fe batteries (2600 batteries/year)

Cost Item	**Calculations**	**Rand (ZA)**	**%**
1. Raw Materials	From Material Balance	258 596	41.0
2. Miscellaneous Material	1% of FCI	3 852	0.6
3. Utilities	From Energy Balance	27 588	4.4

(A) Variable Costs	*(1)+(2)+(3)*	290 036	46.0
4. Maintenance	10% of FCI	38 520	6.1
5. Operation labour	Manning Estimates	111 800	17.7
6. Lab Costs	20% of (5)	22 360	3.5
7. Supervision	20% of (5)	22 360	3.5
8. Plant Overheads	50% of (5)	55 900	8.9
9. Capital Charges	15% of FCI	57 780	9.2
10. Insurance, Local Taxes and Royalties	4% of FCI	15 408	2.4
(B)Fixed Costs	*(4)+(5)+(6)+….+(10)*	324 128	51.4
Direct Production Costs	(A)+(B)	614 164	97.4
(C) General Overheads + R&D	*5% of FCI of the direct production cost*	19 260	3.1
Annual Production Cost	Subtotal (A)+(B)+ (C)	633 424	
Energy Production cost	[R/Wh]	8	

Table 4-6 indicated that R 8 was the cost estimated for a kilowatt-hour in a Ni-Fe system. In addition, R633 424 annual production cost and fixed costs of R324 128 were reported in Table 4-6. This indicated that a significant amount of money was spent on raw materials and equipment. The production cost of a bipolar Ni-Fe battery was computed to 8R/Wh, which is an enormous decrease from the 12R/Wh reported for prismatic Ni-Fe batteries by Iron Edison Co. (2019). The levelized cost of energy of a bipolar Ni-Fe battery is expected to be drastically low (enormous decrease from the production cost) due to the long cycle life and low to no maintenance requirements. The Ni-Fe battery production was performed at lab-scale, the production capacity of Ni-Fe batteries per day estimated during the material balance was 10 batteries; this rate of production was projected to a capacity of 2600 batteries/year. The cost of production was inordinate because the process was performed on a small scale. The factors that influenced the process to be costly at a small scale were the operating labour cost, raw materials cost and utilities cost which constituted of the energy (per year) consumed by a mixer, hydraulic press, BMS and vacuum dryer. These factors do not depend much on the rate of production and are often constant no matter the size of the plant. When a bigger plant is modelled the cost of purchasing the equipment (per unit of capacity) remains steady concurrently with a decrease in the cost of raw materials per kg. Thus, it is relevant to scale up the production capacity in order to reduce the cost of battery production. Based on the production cost of Ni-Fe batteries obtained at the plant capacity of 2600 batteries/year, a scale-up is recommended up to a plant capacity of 26000 batteries/year.

4.7.3 Cash Flow of a Plant Capacity of 2600 Batteries/Year

Figure 4-26 illustrates the cumulative cash flow diagram of a plant with capacity 2600 batteries/year.

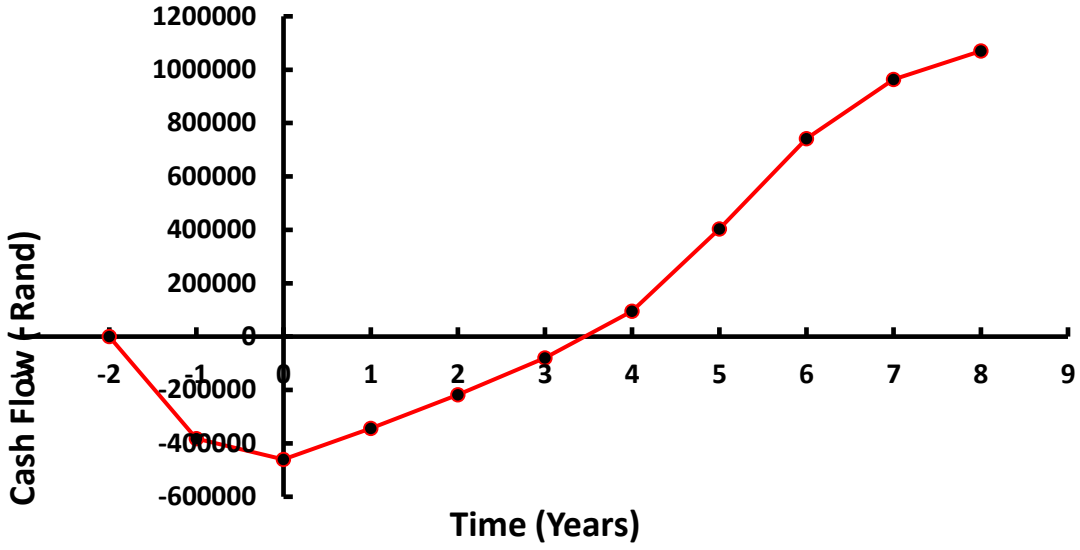

Figure 4-26: Cash flow of a plant with capacity 2600 batteries/year

$$\text{Total NPW of project} = \sum_{n=1}^{n=t} \frac{NFW}{(1+r)^n} = \text{R350 294}$$

List of assumptions

- The process is run at steady-state conditions
- The plant operates for 260 days in a year
- The sales increase by 10% in the first 2 years after the project has been running for a year, by 30 and 40% in the 3rd and 4th year, 10 % in the 5th year and drop by 5% in the last 2 years of the project
- The operating expenses increased by 10% in the first 2 years after the project has been running for a year, 30% in the 3rd and 4th year and by 5% until the end of the project life
- The salvage value of the project is negligible
- The cost associated with land is negligible

Different methods are used to analyse the profitability of projects and process. From the given data the amount that needs to be invested to build the plant and start it up is R460 200. The revenue is attained from sales of 25 Wh Ni-Fe batteries at R300 /battery unit. The trend of both

the sales and operating costs throughout the project life were predicted based on sound judgement keeping in mind that in the early years of the project both operating costs and sales increase and towards the end of the project operating costs continue to increase due to wear and tear of equipment while sales decrease since project completion will be looming.

The payback profitability analysis shows that it takes 3.5 years (Figure 4-26) from the inaugural year of the project to recover the money invested and break even. Profit is only made for the last 4.5 years of the project. Payback analysis does not take the time value of money into account. A better method for profitability analysis is the net present value (NPV) which represents the present value of money of future cash flows. For the company's required interest rate of return of 15%, the NPV is found to be R350 293. A negative NPV indicates that the anticipated expenditure costs in present rand surpass the projected earnings generated by a project or investment, also in present rand. In general, a negative NPV means that the project will subtract value from the plant's present value, it has to be rejected. A positive NPV indicates that the projected earnings generated by a project or investment in present rand exceed the anticipated costs, also in present rand. In general, a positive NPV is profitable. In order to make the project more profitable, it is suggested that the company drops its required IRR. Calculations done for an assumed IRR of 10%, for example, yields an NPV of R525 606. A lower rate of return means recovering money at a lower rate but the probability of making a profit is higher. The cash flow statement with values and methodology utilised in computing NPV and payback period is embodied in Appendix B-Cash Flow Statement.

Chapter 5: Conclusion and Recommendations

5.1 Conclusion

This research work proposes the potential application of Ni-Fe batteries in large-scale energy storage systems. With the aim of developing an efficient high energy-density bipolar Ni-Fe battery, modified composite Fe-based electrodes containing multiple additives were investigated. The drawbacks decelerating the commercialization of Ni-Fe battery, which includes low coulombic efficiency, low energy density and cyclic instability, have been addressed meticulously. Traditionally, there have been several approaches to mitigate the limitations, which includes the integration of additives and dopants (for electrode and electrolyte), modifying cells/battery design, and using nano-sized and nanostructured materials. Mitigating the parasitic hydrogen evolution reaction, increasing high energy and power density and modifying reaction mechanisms and kinetics through the utilisation of additives is the effective way popularly advertised. The promising electrochemical performance of the cell-tested in-house synthesized electrode was attributed to increased bulk electronic conductivity, optimum electrode porosity and decreased hydrogen evolution.

In summary, the experimental research study was centred on multi-additive composite electrode materials hot-pressed on an electro-conductive mesh. The electrochemical effects of additives on Ni-Fe rechargeable batteries have been investigated. The modification of hot-pressed composite negative electrode materials was the primary topic of focus. The outcomes gathered from this study are eligible for consideration for a wide range of electrode types and battery designs. The results garnered from this study are by no means limited to the originally investigated systems and can have a significant impact when utilised on different systems. The galvanostatic cycling and CV techniques were mainly employed for the electrochemical properties quantification and evaluation of the battery and to investigate the electrochemical reaction kinetics of the in-house synthesized electrodes. The in-house synthesized electrode samples were thoroughly characterised by a variety of physical techniques which includes XRD, SEM, TEM and porosimetry.

The research study led to the following conclusions;

- The addition of both the FeS and $CuSO_4$ additives to Fe electrodes resulted in an improvement in chargeability over cycling.
- The addition of Cu in the form of Fe core Cu Shell inhibits particle agglomeration which effectuates prolonged cycling at a higher capacity.
- The addition of FeS enhances the performance of the anode by working as a de-passivation agent during the discharging process.
- The addition of $(NH_4)_2CO_3$ increases the electrodes specific capacity by inducing porosity.
- The results revealed that $FeCu_{0.25}$/15%FeS/5%C/15%AC composite electrode significantly improve the electrochemical performance of the battery with a specific capacity of 410 mAh g^{-1} coulombic efficiency coupled with an average of ≈70% coulombic efficiency.
- The bipolar design reduces the production cost by 33% (from R12/Wh to R8/Wh).

The results indicate that the matrix combination of FeS, Cu, C and $(NH_4)_2CO_3$ additives have a significant impact on improving the overall electrochemical performance of the battery. This outcome thus opens up the possibility of Ni-Fe application in renewable energy battery systems.

5.2 The Novelty of the Study

The novelty findings of this study include:

- The developed electrode formulations
- The design of the battery

5.3 Recommendations

Based on the observations and deductions made throughout the process of achieving the aim and objectives of this study, several recommendations can be made that would necessitate further study in order to improve the findings of the present study.

Thus, the recommendations made for future studies are listed below:

- Modifying synthesis methods of the electrode materials to nanostructure particles.
- Modification of the Fe composite electrode by integrating mixed sulphides, metal sulphides, titanium dioxide etc.
- Modification of the battery/cell design.

- Exploring the particle shape and size effect on the electrochemical performance of the battery using different commercial forms of Fe (produced using wet and thermal routes).

References

1. Abadalla, A. H., Oseghalw, C. I., Posada, J. O. G. & Hall, P. J. 2016. Rechargeable nickel-iron batteries for large-scale energy storage. *The Institute of Engineering and Technology,* 10(10):1529-1534.

2. Ada, I. 2018. *All About Batteries*. Adafruit Industries.

3. Alotto, P., Guarnieri, M. & Moro, F. 2014. Redox flow batteries for the storage of renewable energy: A review. *Renewable and Sustainable Energy Reviews*, 29: 325-335.

4. Amaro, N., Pina, J.M., Martins, J. & Ceballos, J.M. 2012. SUPERCONDUCTING MAGNETIC ENERGY STORAGE - A Technological Contribute to Smart Grid Concept Implementation. *Proceedings of the 1st International Conference on Smart Grids and Green IT Systems*: 113-120.

5. Amiryar, M. & Pullen, K. 2017. A Review of flywheel energy storage system technologies and their applications. *Applied Sciences*, 7(12): 286.

6. Anderson, B. & Oejefors, L. 1976. Slow potentiodynamic studies of porous alkaline iron electrodes. *Chemischer Informationsdienst*, 7(39): 824-828.

7. Apostolakou, A.A., Kookos, I.K., Marazioti, C. and Angelopoulos, K.C. (2009). Techno-economic analysis of a biodiesel production process from vegetable oils. *Fuel Processing Technology*, 90(7-8), pp.1023-1031.

8. Armstrong, R.D. & Baurhoo, I. 1972. Solution soluble species in the operation of the iron electrode in alkaline solution. *Journal of Electroanalytical Chemistry and Interfacial Electrochemistry*, 34(1): 41-46.

9. Bai, F., Wang, Y., Wang, Z., Sun, Y. & Beath, A. 2015. Economic Evaluation of Shell-and-tube Latent Heat Thermal Energy Storage for Concentrating Solar Power Applications. *Energy Procedia*, 69: 737-747.

10. Bak, S., Kim, D. & Lee, H. 2016. Graphene quantum dots and their possible energy applications: A review. *Current Applied Physics*, 16(9): 1192-1201.

11. Balasubramanian, T.S. Vijayamohanan, K. & Shukla, A.K.1993. Mechanisms of the discharge of porous-iron electrodes in alkaline medium. *Journal of Applied Electrochemistry*, 23(9): 947-950.

12. Barbier. 2010. *A Global Green New Deal: Rethinking the Economic Recovery*. New York: Cambridge University Press.

13. Bermann, C. 2007. Impasses and controversies of hydroelectricity. *Hydroelectric Energy*, 21(59): 139-153.

14. Bernard, P. & Lippert, M. 2015. Nickel–Cadmium and Nickel–Metal Hydride Battery Energy Storage. *Electrochemical Energy Storage for Renewable Sources and Grid Balancing*: 223-251.

15. Bode, H., Dehmelt, K. & Witte, J. 1969. To the knowledge of nickel hydroxide electrode. II. On the oxidation products of nickel(II). *Journal of Inorganic and General Chemistry*, 366(1-2): 1-21.

16. Brown, T.J., Feduska, W., Hardman, C. & Pollack, W, Westinghouse Electric Corporation. 1974. *High Energy Density Nickel-iron Battery*. US3853624.

17. Buckles, W. & Hassenzahl, W.V. 2000. Superconducting magnetic energy storage. *IEEE Power Engineering Review*, 20(5): 16-20.

18. Burke, L.D. & Nugent, P.F. 1998. The electrochemistry of gold: II the electrocatalytic behaviour of the metal in aqueous media. *Gold Bulletin*, 31(2): 39-50.

19. Caldas, C.A., Lopes, M.C. & Carlos, I.A. 1998. The role of FeS and $(NH_4)_2CO_3$ additives on the pressed type Fe electrode. *Journal of Power Sources*, 74(1): 108-112.

20. Chakkaravarthy, C., Periasamy, P., Jegannathan, S. & Vasu, K.I. 1991. The nickel/iron battery. *Journal of Power Sources*, 35(1): 21-35.

21. Chen, D., Cheng, J., Wen, Y., Pan, J., Yang, Y. & Cao, G. 2013. Study of Nickel-Plated Monolithic Porous Carbon as a Substrate for Nickel Hydroxide Electrode. *Int. J. Electrochem. Sci*, 8: 6467 - 6477.

22. Comisso, N. & Mengoli, G. 2007. Electrochemical investigations on composite iron electrodes. *Journal of Applied Electrochemistry*, 37(8): 949-959.

23. Constantin, D.M., Rus, E.M., Oniciu, L. & Ghergari, L. 1998. The influence of some additives on the electrochemical behaviour of sintered nickel electrodes in alkaline electrolyte. *Journal of Power Sources*, 74(2): 188-197.

24. Conway, B.E. 2009. *Electrochemical supercapacitors: Scientific Fundamentals and Technological Applications*. New York: Kluwer Acad.

25. Copping, P. & Wood, J. 2011. Ultrabattery storage technology and advanced algorithms at the MW Scale.

26. Cornell, R. & Schwertmann, U. 2003. *The iron oxides*. Weinheim: Wiley-VCH.

27. Dang, T., Le, T., Fribourg-Blanc, E. & Dang, M. 2011. Synthesis and optical properties of copper nanoparticles prepared by a chemical reduction method. *Advances in Natural Sciences: Nanoscience and Nanotechnology*, 2(1): 015009.

28. Davies, T.J., Banks, C.E. & Compton, R.G. 2005. Voltammetry at spatially heterogeneous electrodes. *Journal of Solid State Electrochemistry*, 9(12): 797-808.

29. Desmond, K. 2016. *Innovators in battery technology*. McFarland & Co.

30. Dibrov, A., Chervyak-Voronich, S.M., Grigoreva, T.V., & Kozlova. G.M. UNABLE TO RETRIEVE. Electrochemicaacta, 16(786), 1980.

31. Domingo, C., Rodríguez-Clemente, R. & Blesa, M.A. 1993. Kinetics of oxidative precipitation of iron oxide particles. Colloids and Surfaces A: *Physicochemical and Engineering Aspects*, 79(2-3): 177-189.

32. Dubonosov, A.D, Bren, V.A. & Chernoivanov, V.A. 2003. Norbornadiene-quadricyclane as an abiotic system for the storage of solar energy. *ChemInform*, 34(18).

33. Durgun, E. & Grossman, J.C. 2013. Photoswitchable molecular rings for solar-thermal energy storage. *The Journal of Physical Chemistry Letters*, 4(6): 854-860.

34. Edison Storage Battery Company. 1924. *The Edison alkaline storage battery*.

35. Edward, S.B., Westinghouse Electric Corporation. 1977. *Method of Producing Self-Supporting Fully Activated Iron Electrodes by Thermal Reduction-Sintering*. US4132547.

36. Electric Power Research Institute. 2012. *Pumped-Storage for Energy Storage Applications*. Electric Power Research Institute.

37. Electric Power Research Institute-Department of Energy (US). 2003. *EPRI-DOE Handbook of Energy Storage for Transmission & Distribution Applications*. CA: EPRI PEAC Corporation.

38. Energy Storage Power Corporation (ESPC). 2019. Small CAES with Pipe Storage. *Espcinc.com*. http://www.espcinc.com/mobile/index.php?option=com_k2&view=item&id=11:small-caes-with-pipe-storage&Itemid=3 9 December 2019.

39. Euler, K.J. 1973. Spatial current distribution in non-isotropic conductors (with implication for porous electrodes). *Electrochimica Acta*, 18(5): 385-387.

40. European Parliament. 2018. MEPs ban cadmium from power tool batteries and mercury from button cells | News | European Parliament. *Europarl.europa.eu*. http://www.europarl.europa.eu/news/en/press-room/20131004IPR21519/meps-ban-cadmium-from-power-tool-batteries-and-mercury-from-button-cells 10 July 2018.

41. Exide Industrial Marketing Divisions of ESB, Inc. 1966. *Nickel Iron Industrial Storage Batteries*. Exide Industrial Marketing Divisions of ESB, Inc.

42. Eyer, J. & Corey, G. 2018. *Energy Storage for the Electricity Grid: Benefits and Market Potential Assessment Guide*. Livermore: Sandia National Laboratories.

43. Falk, S.U., Salkind, A.J. & Fleischer, A. 1970. Alkaline storage batteries. *Journal of The Electrochemical Society*, 117(8): 274C.

44. Ferrando, W., Lee, W.W. & Sutula, R.A. 1984. A lightweight nickel composite electrode I: Concept and feasibility. *Journal of Power Sources*, 12(3-4): 249-265.

45. Fournier, E. 2016. As nuclear power plants close, states need to bet big on energy storage. *Skepticalscience.com*. https://www.skepticalscience.com/as-nuclear-plants-close-states-need-energy-storage.html 27 May 2018.

46. Fraunhofer Umsicht. 2019. BiNiFe – Development of a Low-Cost Bipolar Ni-Fe Battery for Energy Storage | CLIENT II. *Bmbf-client.de*. https://www.bmbf-client.de/en/projects/binife 4 November 2019.

47. Fuchs, G., Leuthold, D., Lunz, B. & Sauer, D.U. 2012. *Technology Overview on Electricity Storage*. Institute for Power Electronics and Electrical Drive-Smart Energy for Europe Platform GmbH (SEFEP).

48. Gardner, J. & Haynes, T. 2003. *Overview of Compressed Air Energy Storage*. Boise: Boise State University.

49. Geronov, Y., Tomov, T. & Georgiev, S. 1975. Mossbauer spectroscopy investigation of the iron electrode during cycling in alkaline solution. *Journal of Applied Electrochemistry*, 5(4): 351-358.

50. Götz, M., Lefebvre, J., Mörs, F., McDaniel Koch, A., Graf, F., Bajohr, S., Reimert, R. & Kolb, T. 2016. Renewable Power-to-Gas: A technological and economic review. *Renewable Energy*, 85: 1371-1390.

51. Götz, M., Lefebvre, J., Mörs, F., McDaniel Koch, A., Graf, F., Bajohr, S., Reimert, R. & Kolb, T. 2016. Renewable Power-to-Gas: A technological and economic review. *Renewable Energy*, 85: 1371-1390.

52. Guinier, A. 2013. *X-Ray Diffraction*. Dover Publications.

53. Hagihara, H., Shibata, S., Akasaka, Y. & Furukawa, J. 2016. Development and commodification of "UltraBattery" using the ion exchange action of the activated carbon. *Journal of Ion Exchange*, 27(3): 47-52.

54. Halpert, G. 1984. Past developments and the future of nickel electrode cell technology. *Journal of Power Sources*, 12(3-4): 177-192.

55. Hampson, N.A., Latham, R.J., Marshall, A. & Giles, R.D. 1974. Some aspects of the electrochemical behaviour of the iron electrode in alkaline solutions. *Electrochimica Acta*, 19(7): 397-401.

56. Hang, B.T., Watanabe, T., Egashira, M., Watanabe, I., Okada, S. & Yamaki, J.I. 2006. The effect of additives on the electrochemical properties of Fe/C composite for Fe/air battery anode. *Journal of Power Sources*, 155(2): 461-469.

57. Hardman, C. 1972. Method of impregnating flexible metallic battery plaques.

58. Hariprakash, B., Martha, S.K., Hegde, M.S. & Shukla, A.K. 2005. A sealed, starved-electrolyte nickel-iron battery. *Journal of Applied Electrochemistry*, 35(1): 27-32.

59. Hasnain, S.M. 1998. Review on sustainable thermal energy storage technologies, Part I: heat storage materials and techniques. *Energy Conversion and Management*, 39(11): 1127-1138.

60. Helwig, A. & Ahfock, T. 2013. Long-life Nickel Iron Battery Functionality / Cost Comparison for Peak Demand SWER Network Voltage Support Application. In *Australasian Universities Power Engineering Conference*. Hobart, Australia: AUPEC,1-6.

61. Huang, K. & Chou, K. 2007. Microstructure changes to iron nanoparticles during discharge/charge cycles. *Electrochemistry Communications*, 9(8): 1907-1912.

62. Huang, L., Yang, J., Zhu, D. & Chen, Y. 2018. Copper/Iron Composite Anode prepared by in situ co-precipitation with Excellent High-rate and Low-temperature Performance for Rechargeable Nickel-Iron Battery. *International Journal of Electrochemical Science*, 13: 7045-7056.

63. Huggins, R. 2010. *Energy storage*. New York: Springer.

64. Ibrahim, H., Ilinca, A. & Perron, J. 2008. Energy storage systems—characteristics and comparisons. *Renewable and Sustainable Energy Reviews*, 12(5): 1221-1250.

65. International Electrotechnical Commission (IEC). 2010. *Electrical Energy Storage*. Geneva: International Electrotechnical Commission.

66. International Renewable Energy Agency (IREA). 2017. *Electricity storage and renewables: Costs and markets to 2030*. Abu Dhabi: International Renewable Energy Agency.

67. International Renewable Energy Agency (IREA). 2018. *Global Energy Transformation: A Roadmap to 2050*. Abu Dhabi: International Renewable Energy Agency.

68. Inkson, B. 2016. Scanning electron microscopy (SEM) and transmission electron microscopy (TEM) for materials characterization. *Materials Characterization Using Nondestructive Evaluation (NDE) Methods*: 17-43.

69. Iron Edison Co. 2019. Buy Nickel Iron Batteries Online| Best NiFe Edison Battery. Ironedison.com. https://ironedison.com/nickel-iron-ni-fe-battery 6 December 2019.

70. Jaenhig, D., Hausner, R., Wagner, W. & Isaksson, C. 2006. Thermo-Chemical Storage for Solar Space Heating in a Single-Family House. In *10th International Conference on Thermal Energy Storage: Ecostock 2006*. Gleisdorf, Austria: AAE-Institute for Sustainable Technologies.

71. Jayalakshm, M. & Muralidharan, V.S. 1991. Electrochemical characterisation of porous iron electrodes. *Journal of Chemical Sciences*, 103(6): 753-761.

72. Jensen, W.B. 2013. *Oesper Collections: The Edison Nickel-Iron Alkaline Storage Cell*. Cincinnati: University of Cincinnati.

73. Jentsch, M., Trost, T. & Sterner, M. 2014. Optimal use of power-to-gas energy storage systems in an 85% renewable energy scenario. *Energy Procedia*, 46: 254-261.

74. Jiang, W., Liang, F., Wang, J., Su, L., Wu, Y. & Wang, L. 2014. Enhanced electrochemical performances of FeOx–graphene nanocomposites as anode materials for alkaline nickel-iron batteries. *Royal Society of Chemistry Adv.*, 4(30): 15394-15399.

75. Kao, C. & Chou, K. 2010. Iron/carbon-black composite nanoparticles as an iron electrode material in a paste type rechargeable alkaline battery. *Journal of Power Sources*, 195(8): 2399-2404.

76. Kao, C., Tsai, Y. & Chou, K. 2011. Synthesis and characterization of the iron/copper composite as an electrode material for the rechargeable alkaline battery. *Journal of Power Sources*, 196(13): 5746-5750.

77. Komarnicki, P., Lombardi, P. & Styczynski, Z. 2017. *Electric Energy Storage Systems: Smart Options for Smart Grids*. Springer.

78. Komarnicki, P., Lombardi, P. & Styczynski, Z. 2017. *Electric Energy Storage Systems: Smart Options for Smart Grids*. Springer.

79. Kononenko, V.E., Tamazina, V.N. & Ozerova, A.I. 1978. *Method of Manufacturing an Iron Electrode for Alkaline Accumulators*. US4123568.

80. Kötz, R. & Carlen, M. 2000. Principles and applications of electrochemical capacitors. *Electrochimica Acta*, 45(15-16): 2483-2498.

81. Lam, L.T. & Louey, R. 2006.4 Development of ultra-battery for hybrid-electric vehicle applications. *Journal of Power Sources*, 158(2): 1140-1148.

82. Latimer, W.M. & Latimer, M. 1938. *The oxidation states of the elements and their potentials in aqueous solutions*. New York: Prentice-Hall.

83. Lee, D., Lei, D. & Yushin, G. 2018. Morphology and phase changes in iron anodes affecting their capacity and stability in rechargeable alkaline batteries. *ACS Energy Letters*, 3(4): 794-801.

84. Lee, K.J., Elgrishi, N., Kandemir, B. & Dempsey, J.L. 2017. Electrochemical and spectroscopic methods for evaluating molecular electrocatalysts. *Nature Reviews Chemistry*, 1(5).

85. Lennartson, A., Roffey, A. & Moth-Poulsen, K. 2015. Designing photoswitches for molecular solar thermal energy storage. *Tetrahedron Letters*, 56(12): 1457-1465.

86. Lennartson, A., Roffey, A. & Moth-Poulsen, K. 2015. Designing photoswitches for molecular solar thermal energy storage. *Tetrahedron Letters*, 56(12): 1457-1465.

87. Levine, J. 2003. *Pumped hydroelectric energy storage and spatial diversity of wind resources as methods of improving utilization of renewable energy sources*. Msc. Michigan Technological University.

88. Li, J., Guo, L., Shangguan, E., Yue, M., Xu, M., Wang, D., Chang, Z. & Li, Q. 2017. Synthesis of novel spherical Fe3O4@Ni3S2 composite as improved anode material for rechargeable nickel-iron batteries. *Electrochimica Acta*, 240: 456-465.

89. Linden, D. & Reddy, T.B. 2002. *Handbook of batteries and fuel cells*. 3rd ed. New York: McGraw-Hill.

90. Linden, D. & Reddy, T.B. 2010. *Handbook of batteries and fuel cells*. 4th ed. New York: McGraw-Hill.

91. Linden, D. 1984. *Handbook of batteries and fuel cells*. New York: McGraw-Hill.

92. Liu, J.L., Chen, M.H., Zhang, L.L., Jiang, J., Yan, J.X., Huang, Y.Z., Lin, J.Y., Fan, H. & Shen, Z.X. 2014. A flexible alkaline rechargeable Ni/Fe battery based on graphene foam/carbon nanotubes hybrid film. *Nano Letters*, 14(12): 7180-7187.

93. Liu, K., Li, K., Peng, Q. & Zhang, C. 2018. A brief review on key technologies in the battery management system of electric vehicles. *Frontiers of Mechanical Engineering*, 14(1): 47-64.

94. Longsheng, Z., Qianwei., D., Yunpeng, H., Huahoa, Gu., Yue-E, M. & Tianxi, L. 2015. Flexible hybrid membranes with $Ni(OH)_2$ nanoplatelets vertically grown on electrospun carbon

nanofibers for high-performance supercapacitors. *American Chemical Society,* 7(40):22669-22677.

95. Luo, H., Wang, B., Li, Y., Liu, T., You, W. & Wang, D. 2017. Core-shell structured Fe 3 O 4 @NiS nanocomposite as high-performance anode material for alkaline nickel-iron rechargeable batteries. *Electrochimica Acta*, 231: 479-486.

96. Luo, X., Wang, J., Dooner, M. & Clarke, J. 2015. Overview of current development in electrical energy storage technologies and the application potential in power system operation. *Applied Energy*, 137: 511-536.

97. Macdonald, D.D. & Owen, D. 1973. The Electrochemistry of iron in IM lithium hydroxide solution at 22° and 200°C. *Journal of The Electrochemical Society*, 120(3): 317.

98. MacKenzie, J.M.J., Salkind, A.J. 1968. Gas depressor additives for iron electrodes.

99. Malkhandi, S., Yang, B., Manohar, A.K., Prakash, G.K.S. & Narayanan, S.R. 2012. Self-assembled monolayers of n-alkanethiols suppress hydrogen evolution and increase the efficiency of rechargeable iron battery electrodes. *Journal of the American Chemical Society*, 135(1): 347-353.

100. Manohar, A.K., Malkhandi, S., Yang, B., Yang, C., Surya Prakash, G.K. & Narayanan, S.R. 2012. A high-performance rechargeable Iron electrode for large-scale battery-based energy storage. *Journal of the Electrochemical Society*, 159(8): A1209-A1214.

101. Manohar, A.K., Yang, C., Malkhandi, S., Prakash, G.K.S. & Narayanan, S.R. 2013. Enhancing the performance of the rechargeable iron electrode in alkaline batteries with bismuth oxide and iron sulphide additives. *Journal of the Electrochemical Society*, 160(11): A2078-A2084.

102. Mao, Z., Visintin, A., Srinivasan, S., Appleby, A. & Lim, H. 1992. Microcalorimetric study of the self-discharge of the NiOOH/$Ni(OH)_2$ electrode in a hydrogen environment. *Journal of Applied Electrochemistry*, 22(5): 409-414.

103. Medway, S.L., Lucas, C.A., Kowal, A., Nichols, R.J. & Johnson, D. 2006. In situ studies of the oxidation of nickel electrodes in alkaline solution. *Journal of Electroanalytical Chemistry*, 587(1): 172-181.

104. Mrha, J., Krejčí, I., Zábranský, Z., Koudelka, V. & Malík, J. 1979. Plastic bonded electrodes for nickel-cadmium accumulators II. Basic electrochemical parameters of the nickel oxide electrode. *Journal of Power Sources*, 4(3): 239-250.

105. Muñoz-Torrero, D., Palma, J., Marcilla, R. & Ventosa, E. 2019. A critical perspective on rechargeable Al-ion battery technology. *Dalton Transactions*, 48(27): 9906-9911.

106. Nakajima, H., Honma, T., Midorikawa, K., Akasaka, Y., Shibata, S., Yoshida, H., Hashimoto, K., Ogino, Y., Tezuka, W., Miura, M., Furukawa, J., Lam, T. & Sugata, S. 2012. Development of Ultra-battery. *Furukawa Review*, 43: 1-8.

107. Nakhamkin, M. 2007. *Novel Compressed Air Energy Storage Concepts Developed by ESPC*, EESAT, May 2007.

108. Narayan, S.R., Manohar, A.K., Yang, C., Prakash, G.K.S. & Aniszdeld, R. 2015. *High Efficiency Nickel-Iron Battery*. US20150086884.

109. Nitta, N., Wu, F., Lee, J. & Yushin, G. 2015. Li-ion battery materials: present and future. *Materials Today*, 18(5): 252-264.

110. Novakovskii, A.M., Grushkina, S.A. & Kozlova, R.L. 1973. Influence of electrical conductivity of the active material on the behavior of the iron plate in an alkaline storage cell. *Journal of Applied Chemistry USSR*, 46(9): 2150-2183.

111. Öjefors, L. & Carlsson, L. 1978. An iron—air vehicle battery. *Journal of Power Sources*, 2(3): 287-296.

112. Öjefors, L. 1976. Self-discharge of the alkaline iron electrode. *Electrochimica Acta*, 21(4): 263-266.

113. Pan, F. & Wang, Q. 2015. Redox species of redox flow batteries: A review. *Molecules*, 20(12): 20499-20517.

114. Paulraj, A., Kiros, Y., Skårman, B. and Vidarsson, H. (2017). Core/Shell Structure Nano-Iron/Iron Carbide Electrodes for Rechargeable Alkaline Iron Batteries. *Journal of The Electrochemical Society*, 164(7), pp.A1665-A1672.

115. Periasamy, P., Ramesh Babu, B. & Venkatakrishna Iyer, S. 1996. Performance characterization of sintered iron electrodes in nickel/iron alkaline batteries. *Journal of Power Sources*, 62(1): 9-14.

116. Posada, J. O. G. & Hall, P. J. 2016. Towards the development of safe and commercially viable nickel-iron batteries: improvements to Coulombic efficiency at high iron sulphide electrode formulations. *Journal of Applied Electrochemistry,* 46(4):451-458.

117. Posada, J. O. G., Abdalla, A. H., Oseghalw, C. I. & Hall, P. J. 2016. Multiple regression analysis in the development of Ni-Fe cells as energy storage solutions for intermittent power sources such as wind or solar. *International Journal of Hydrogen Energy,* 41(37): 16330-16337.

118. Posada, J.O.G., Rennie, A., Villar, S., Martins, V., Marinaccio, J., Barnes, A., Glover, C., Worsley, D. & Hall, P. 2017. Aqueous batteries as grid-scale energy storage solutions. *Renewable and Sustainable Energy Reviews*, 68: 1174-1182.

119. Poullikkas, A. 2013. A comparative overview of large-scale battery systems for electricity storage. *Renewable and Sustainable Energy Reviews*, 27: 778-788.

120. Pourbaix, M., Deltombe, E. & Van Leugenhaghe, C. 1966. *Atlas of electrochemical equilibria in aqueous solutions*. Oxford [etc.]: Pergamon Press.

121. Pyun, S.I., Shin, H.C., Lee, J.W. & Go, J.Y. 2012. *Electrochemistry of insertion materials for hydrogen and lithium*. Springer.

122. Ravikumar, M.K., Balasubramanian, T.S. & Shukla, A.K. 1995. A nickel-iron battery with roll-compacted iron electrodes. Journal of Power Sources, 56(2): 209-212.

123. Reddy, T. & Linden, D. 2010. *Linden's Handbook of Batteries (4th Edition)*. 4th ed. New York, USA: McGraw-Hill Professional Publishing.

124. Reimer, L. 2013. *Transmission Electron Microscopy*. Berlin, Heidelberg: Springer Berlin / Heidelberg.

125. Renewable Energy Network for the 21st Century. 2015. *Renewables 2015-Global Status Report*. Paris: REN21.

126. Renewable Energy Network for the 21st Century. 2016. Renewables 2016-Global Status Report. Paris: REN21.

127. Salkind, A.J., Venuto, C.J. & Falk, S.U. 1964. The reaction at the iron alkaline electrode. *Journal of The Electrochemical Society*, 111(5): 493.

128. Sarkar, D., Shukla, A. & Sarma, D.D. 2016. Substrate integrated nickel-iron ultra-battery with extraordinarily enhanced performances. *ACS Energy Letters*, 1(1): 82-88.

129. Sasanian, S. & Newson, T.A. 2013. Use of mercury intrusion porosimetry for microstructural investigation of reconstituted clays at high water contents. *Engineering Geology*, 158: 15-22.

130. Schossig, P. 2008. Thermal Energy Storage. In *3rd International Renewable Energy Storage Conference*. Berlin, Germany.

131. Shah, Y.T. 2016. *Energy and Fuel Systems Integration*. Boca Raton: CRC Press.

132. Shah, Y.T. 2018. *Thermal Energy: Sources, Recovery, and Applications*. Boca Raton: CRC Press.

133. Shangguan, E., Fu, S., Wu, C., Cai, X., Li, J., Chang, Z., Wang, Z. & Li, Q. 2019. Sublimed sulfur powders as novel effective anode additives to enhance the high-rate capabilities of iron anodes for advanced iron-based secondary batteries. *Electrochimica Acta*, 301: 162-173.

134. Shruthi, B., Bheema Raju, V. & Madhu, B.J. 2015. Synthesis, spectroscopic and electrochemical performance of pasted β-nickel hydroxide electrode in alkaline electrolyte. *Spectrochimica Acta Part A: Molecular and Biomolecular Spectroscopy*, 135: 683-689.

135. Shukla, A.K., Ravikumar, M.K. & Balasubramanian, T.S. 1994. Nickel/iron batteries. *Journal of Power Sources*, 51(1-2): 29-36.

136. Sichuan Changhong Battery Co., Ltd. 2008. *Nickel-Iron batteries for solar PV application*. Mianyang Sichuan: Sichuan Changhong Battery Co., Ltd.

137. Simon, P. & Gogotsi, Y. 2009. Materials for electrochemical capacitors. *Nanoscience and Technology*: 320-329.

138. Simon, P. & Gogotsi, Y. 2009. Materials for electrochemical capacitors. *Nanoscience and Technology*: 320-329.

139. Stagi, L., De Toro, J.A., Ardu, A., Cannas, C., Casu, A., Lee, S. & Ricci, P.C. 2014. Surface effects under visible irradiation and heat treatment on the phase stability of γ-Fe_2O_3 nanoparticles and γ-Fe_2O_3 −SiO_2 core-shell nanostructures. *The Journal of Physical Chemistry*, 118(5): 2857-2866.

140. Stead, J. & Stead, W. 2009. *Management for a small planet*. 3rd ed. Armonk: M. E. Sharpe.

141. Stokes, D. 2008. *Principles and practice of variable pressure/environmental scanning electron microscopy (VP-ESEM)*. Chichester, U.K: Wiley.

142. Sturkenboom, L. 2016. *The Ni-FeS Battery: Technology and Performance Analysis*. MSc. Utrecht University.

143. Sundar Rajan, A., Ravikumar, M.K., Priolkar, K.R., Sampath, S. & Shukla, A.K. 2015. Carbonyl-Iron Electrodes for Rechargeable-Iron Batteries. *Electrochemical Energy Technology*, 1(1).

144. Suryanarayana, C. 2016. Microstructure: An Introduction. *Aerospace Materials and Material Technologies*: 105-123.

145. Tarascon, J.M. & Armand, M. 2010. Issues and challenges facing rechargeable lithium batteries. *Materials for Sustainable Energy*: 171-179.

146. Tiedemann, W. & Newman, J. 1975. Maximum effective capacity in an ohmically limited porous electrode. *Journal of The Electrochemical Society*, 122(11): 1482.

147. Tilman, D., Hill, J. & Lehman, C. 2006. Carbon-negative biofuels from low-input high-diversity grassland biomass. *Science*, 314(5805): 1598-1600.

148. Ultrabattery. 2018. UltraBattery Technology. *Ultrabattery.com*. http://ultrabattery.com/technology/ultrabattery-technology/ 27 May 2018.

149. Van der Ven, A., Morgan, D., Meng, Y.S. & Ceder, G. 2006. Phase Stability of Nickel Hydroxides and Oxyhydroxides. *Journal of The Electrochemical Society*, 153(2): A210.

150. Van Dijk, T. 2012. *A New Nickel Iron-Sulphide Battery*. Ph.D. Delft University of Technology.

151. Vassie, P.R. & Tseung, A.C.C. 1976. High performance, rechargeable sintered iron electrodes: The effect of preparative methods and additives on the structure and performance of sintered iron electrodes. *Electrochimica Acta*, 21(4): 299-302.

152. Vijayamohanan, K., Balasubramanian, T.S. & Shukla, A.K. 1991. Rechargeable alkaline iron electrodes. *Journal of Power Sources*, 34(3): 269-285.

153. Vijayamohanan, K., Shukla, A.K. & Sathyanarayana, S. 1990. Kinetics of electrode reactions occurring on porous iron electrodes in alkaline media. *Journal of Electroanalytical Chemistry and Interfacial Electrochemistry*, 295(1-2): 59-70.

154. Vmack Co. 2018. Iron Cell Diagram - Product Wiring Diagrams. *product wiring diagrams*. http://vmack.co/iron-cell-diagram.html 27 September 2018.

155. Vu, V., Datta, A., Fontaine, L.C. & Parth, A.J. 2018. Nickel iron battery. US9941548B2.

156. Wabner, D.W., Kandler, L. & Krienke, W. 1985. *Positive electrodes of Nickel-Cadmium batteries*. NASA-Center for Aerospace Information (CASI).

157. Wang, H., Liang, Y., Gong, M., Li, Y., Chang, W., Mefford, T., Zhou, J., Wang, J., Regier, T., Wei, F. & Dai, H. 2012. An ultrafast nickel–iron battery from strongly coupled inorganic nanoparticle/nanocarbon hybrid materials. Nature Communications, 3(1): 1-8.

158. Wang, Q. & Wang, Y. 2016. Overcoming the limiting step of Fe_2O_3 reduction via in situ sulphide modification. *ACS Applied Materials & Interfaces*, 8(16): 10334-10342.

159. Wang, Y., He, P. & Zhou, H. 2012. Li-redox flow batteries based on hybrid electrolytes: at the crossroad between Li-ion and redox flow batteries. *Advanced Energy Materials*, 2(7): 770-779.

160. Weber, A.Z., Mench, M.M., Meyers, J.P., Ross, P.N., Gostick, J.T. & Liu, Q. 2011. Redox flow batteries: a review. *Journal of Applied Electrochemistry*, 41(10): 1137-1164.

161. Weber, A.Z., Mench, M.M., Meyers, J.P., Ross, P.N., Gostick, J.T. & Liu, Q. 2011. Redox flow batteries: a review. *Journal of Applied Electrochemistry*, 41(10): 1137-1164.

162. Weinrich, H., Come, J., Tempel, H., Kungl, H., Eichel, R. & Balke, N. 2017. Understanding the nanoscale redox-behaviour of iron-anodes for rechargeable iron-air batteries. *Nano Energy*, 41: 706-716.

163. Wells, A. 1970. *Models in structural inorganic chemistry*. New York: Oxford University Press.

164. Whittingham, M. 2008. Materials challenges facing electrical energy storage. *MRS Bulletin*, 33(04): 411-419.

165. Winter, M. & Brodd, R.J. 2004. What Are Batteries, Fuel Cells, and Supercapacitors?. *Chemical Reviews*, 104(10): 4245-4270.

166. World Energy Council (WEC). 2019. *World Energy Scenarios 2019*. London: World Energy Council (WEC).

167. World Energy Council (WEC). 2016. World Energy Resources-2016. World Energy Council (WEC). http://large.stanford.edu/courses/2016/ph240/thornton2/docs/ises-2005.pdf 3 October 2018.

168. Yang, C., Manohar, A. and Narayanan, S. (2017). A High-Performance Sintered Iron Electrode for Rechargeable Alkaline Batteries to Enable Large-Scale Energy Storage. *Journal of The Electrochemical Society*, 164(2), pp.A418-A429.

169. Xie, K., Li, J., Lai, Y., Lu, W., Zhang, Z., Liu, Y., Zhou, L. & Huang, H. 2011. Highly ordered iron oxide nanotube arrays as electrodes for electrochemical energy storage. *Electrochemistry Communications*, 13(6): 657-660.

170. Xusheng, D., Hong-Yuan, L. & Yiu-Wing, M. 2016. Ultrafast synthesis of multifunctional n-doped graphene foam in an ethanol flame. *American Chemical Society,* 10(1):453-462.

171. Zalba, B., Marín, J., Cabeza, L.F. & Mehling, H. 2003. Review on thermal energy storage with phase change: materials, heat transfer analysis and applications. *Applied Thermal Engineering*, 23(3): 251-283.

172. Zhang, H. 1994. Rotating Ring-Disk Electrode and Spectroelectrochemical Studies on the Oxidation of Iron in Alkaline Solutions. *Journal of The Electrochemical Society*, 141(3): 718.

173. Zhao, H., Wu, Q., Hu, S., Xu, H. & Rasmussen, C.N. 2015. Review of energy storage system for wind power integration support. *Applied Energy*, 137: 545-553.

174. Zhao, J., Baibuz, E., Vernieres, J., Grammatikopoulos, P., Jansson, V., Nagel, M., Steinhauer, S., Sowwan, M., Kuronen, A., Nordlund, K. and Djurabekova, F. (2016). Formation Mechanism of Fe Nanocubes by Magnetron Sputtering Inert Gas Condensation. *ACS Nano*, 10(4), pp.4684-4694.

175. Zito, R. 2010. *Energy storage: A New Approach*. Hoboken, NJ: John Wiley & Sons.

176. Zohuri, B. 2017. *Hybrid Energy Systems*. New York: Springer.

Appendix A-Cycling Data

Table A-1: Discharge capacity data: the cells were charged at 100mA/g to 1.6 v, and then discharged at 100 mA/g C to 0.8 V

	C-Dchg																
Cycle	**PE1**	**PE2**	**PE3**	**PE4**	**PE5**	**PE6**	**PE7**	**PE8**	**PE9**	**PE10**	**PE11**	**PE12**	**PE13**	**PE14**	**PE15**	**PE16**	**PE17**
1	136.6	167.6	236.4	329.6	369.5	376.3	376.3	376.7	382.9	392.7	396.6	402.3	415.1	427.1	440.1	445.1	451.1
2	120.7	145.7	226.8	309.7	354.8	364.1	352.2	372.6	378.1	385.1	391.1	390.1	408.1	420.1	433.1	439.1	444.1
3	123.5	138.5	215.5	309.5	344.5	359.9	339.2	371.1	378.7	382.2	388.5	385.9	407.5	419.5	432.5	438.5	435.1
4	117.2	137.2	216.8	298.8	340	358.9	338.7	373.7	378.8	382.7	388.7	384.9	406.7	418.7	431.7	437.7	430.1
5	112.2	131.2	218.8	304.8	336	359.2	331.1	372.6	378.1	382.3	388.1	385.2	406.1	418.1	431.1	436.1	428.4
6	109.8	131.8	214.6	303.6	343.9	362.4	321.6	371.2	378.8	381.2	387.5	388.4	405.5	417.5	430.5	435.1	427.1
7	104.7	129.7	216.7	303.7	347.4	357.4	318.9	372.6	377.3	382.7	389.8	383.4	405.8	417.8	430.8	434.8	422.1
8	102.9	129.9	214.9	297.3	340.3	357.3	312.8	373.6	378.4	383.1	387.4	383.3	405.4	417.4	430.4	433.1	422.4
9	101.9	125.9	216.6	295.6	344.4	358.5	308.7	371.7	379.6	385.2	389.5	384.5	405.5	418.5	431.5	432.1	421.5
10	99.2	131.2	219.9	299.5	336.8	364.8	301.2	369.1	378.8	384.4	388.1	388.8	404.1	416.1	429.1	431.1	420.1
11	101.7	137.7	214.4	299.6	339.5	361.5	300.2	369.7	380.1	385.6	388.2	387.5	405.1	417.1	430.1	430.1	421.1
12	97.3	127.7	213.5	298.7	343.8	357.7	297.1	371.7	381.8	384.7	390.3	383.7	403.2	415.2	428.2	430.1	419.2
13	96.3	125.5	213.5	299.5	345.5	358.6	296.1	374.5	382.7	385.5	388.1	384.6	404.1	416.1	429.1	429.1	420.1
14	94.7	120.8	215.8	301.4	343.9	358.2	295.7	371.8	381.3	385.4	392.4	384.2	403.7	415.7	430.7	427.7	419.7
15	97.1	117.2	212.1	297.8	342.2	360.2	292.1	371.2	382.7	383.8	388.7	386.2	404.7	416.7	429.7	425.1	420.7
16	97.1	115.1	214.6	298.6	339.7	361.6	290.1	371.1	383.8	384.6	388.2	387.6	404.1	416.1	429.1	425.1	420.1
17	88.7	116.9	211.5	302.7	344.4	359.4	286.5	370.8	381.9	385.7	390.9	385.4	404.9	416.9	429.9	426.1	420.9
18	93.9	118.9	211.9	295.3	338.4	362.2	285.1	372.9	381.8	382.3	386.9	388.2	405.7	417.7	430.7	424.1	421.7
19	90.1	121.9	214.6	298.6	342.4	358.4	281.4	371.2	382.3	384.6	390.9	384.4	403.9	415.9	428.9	424.7	419.9
20	91.2	125.2	209.9	302.5	344.8	363.1	280.3	374.3	384.2	386.5	393.3	389.1	404.6	416.6	429.6	425.1	420.6
21	91.4	122.6	205.7	299.6	340.5	362.5	275.2	371.2	381.8	385.6	389.2	388.5	404.4	416.4	429.4	426.1	420.4
22	90.7	117.7	204.1	298.7	344.8	360.8	272.1	371.4	382.8	384.7	390.3	386.8	404.3	416.3	429.3	425.1	420.3
23	87.5	113.5	203.1	297.5	345.5	361.4	271.1	374.5	382.1	386.5	389.1	387.4	405.9	417.9	430.9	424.1	421.9

24	86.8	116.8	209.1	296.1	343.9	360.4	271.2	372.3	381.8	384.8	392.4	386.4	404.9	416.9	429.9	423.9	420.9
25	86.2	115.2	199.1	299.3	342.2	356.7	269.4	374.9	382.1	385.8	390.7	382.7	406.7	418.7	431.7	425.7	422.7
26	80.8	117.8	196.6	294.1	344.9	355.9	267.7	371.4	382.1	382.6	390.4	381.9	404.4	416.4	429.4	423.4	420.4
27	76.7	112.7	195.7	293.2	347.4	358.4	267.1	372.9	382.5	385.7	390.9	384.4	403.9	415.9	428.9	422.9	419.9
28	72.9	104.9	194.9	291.1	351.2	361.2	260.5	371.1	381.8	382.3	389.7	387.2	403.7	415.7	428.7	424.7	419.7
29	69.9	99.7	193.6	296.7	348.4	359.4	262.3	371.2	383.8	382.6	389.9	385.4	405.9	417.9	430.9	424.9	421.9
30	65.2	99.2	193.9	289.7	343.8	363.3	260.1	371.4	381.8	382.5	389.3	389.3	404.3	416.3	429.3	423.3	420.3
31	64.7	105.2	188.9	289.4	344.8	363.1	258.1	374.3	384.2	386.5	393.3	389.1	404.6	416.6	429.6	423.4	420.4
32	67.4	102.6	190.4	292.5	340.5	359.5	255.1	371.2	381.8	385.6	389.2	385.5	404.4	416.4	429.4	423.3	420.3
33	63.7	97.7	190.7	292	344.8	360.8	255.2	371.4	382.8	384.7	390.3	386.8	404.3	416.3	429.3	424.9	421.9
34	60.5	93.5	189.5	291.2	345.5	361.4	257.4	374.5	382.1	386.5	389.1	387.4	405.9	417.9	430.9	423.9	420.9
35	59.8	96.8	194.8	288.1	343.9	360.4	258.5	372.3	381.8	384.8	392.4	386.4	404.9	416.9	429.9	425.7	422.7
36	62.2	95.2	195.1	287.1	342.2	356.7	253.1	374.9	382.1	385.8	390.7	382.7	406.7	418.7	431.7	423.4	420.4
37	60.8	97.8	196.6	287.9	344.9	357.9	254.1	371.4	382.1	382.6	390.4	383.9	404.4	416.4	429.4	422.9	419.9
38	59.7	93.7	195.7	292.1	347.4	358.4	253.1	372.9	382.5	385.7	390.9	384.4	403.9	415.9	428.9	424.7	419.7
39	59.9	92.9	194.9	287.6	339.2	358.2	252.1	371.1	381.8	382.3	389.7	384.2	403.7	415.7	428.7	424.9	421.9
40	58.9	93.7	193.6	288.1	341.4	358.4	251.7	371.2	383.8	382.6	389.9	384.4	405.9	417.9	430.9	423.3	420.3

The coulombic efficiency, denoted by η_c, was calculated by Q_d / Q_c * 100% using discharge capacity (Q_c) at 10th cycle for each electrode. The charge capacities of each electrode at the 10^{th} cycle is presented below.

Table A-2: Charge capacity at the 10th cycle: the cells were charged at 100mA/g to 1.75 V

Electrode	Charge Capacity at 10^{th} Cycle
PE1	255
PE2	305
PE3	470
PE4	500
PE5	540
PE6	555
PE7	559
PE8	561
PE9	565
PE10	552
PE11	551
PE12	550
PE13	554
PE14	567
PE15	579
PE16	577
PE17	551

Where:

Table A-3: Electrode composition

PE1	Fe
PE2	$FeCu_{0.05}$
PE3	$FeCu_{0.10}$
PE4	$FeCu_{0.15}$
PE5	$FeCu_{0.20}$
PE6	$FeCu_{0.25}$
PE7	$FeCu_{0.30}$
PE8	$FeCu_{0.25}$/3%FeS
PE9	$FeCu_{0.25}$/6%FeS
PE10	$FeCu_{0.25}$/9%FeS
PE11	$FeCu_{0.25}$/12%FeS
PE12	$FeCu_{0.25}$/15%FeS
PE13	$FeCu_{0.25}$/15%FeS/5%AC
PE14	$FeCu_{0.25}$/15%FeS/10%AC
PE15	$FeCu_{0.25}$/15%FeS/15%AC
PE16	$FeCu_{0.25}$/15%FeS/20%AC
PE17	$FeCu_{0.25}$/15%FeS/25%AC

Appendix B-Cash Flow Statement

Table B-1: Cash flow statement (in Rands)

		Total operating costs	634 424		**IRR**	15%					
		Total Operating cost	633 424		**Taxation Rate**	30%					
Year	-2	-1	0	1	2	3	4	5	6	7	8
Fixed Capital Investment		382 200									
Working Capital			-78 000								
Total Capital Investment		-382 200									
Profit - Loss Statement											
Revenue				780 000.0	858 000.0	943 800.0	1 226 940.0	1 717 716.0	1 889 487.6	1 795 013.2	1 705 262.6
Cash Operating Expenses				633 424.0	696 623.4	766 285.7	996 171.5	1 295 022.9	1 424 525.2	1 495 751.5	1 570 539.0
Depreciation				47 775.0	47 775.0	47 775.0	47 775.0	47 775.0	47 775.0	47 775.0	47 775.0
Total Operating Expenses				681 069.0	744 398.4	814 060.7	1043 946.5	1 342 797.9	1 472 300.2	1 543 526.5	1 618 314.0
Operating Income				146 706.0	161 376.6	177 514.3	230 768.5	422 693.1	464 962.4	299 261.8	134 723.5
Net Income Before Taxes				98 931.0	113 601.6	129 739.3	182 993.5	374 918.1	417 187.4	251 486.8	86 948.5
Federal Income Taxes				29 679.3	34 080.5	38 921.8	54 898.1	112 475.4	125 156.2	75 446.0	26 084.6
Net Income After Taxes				69 251.7	79 521.1	90 817.5	128 095.5	262 442.7	292 031.2	176 040.7	60 864.0
After Tax Cash Flow			-460 200	117 026.7	127 296.1	138 592.5	175 870.5	310 217.7	339 806.2	223 815.7	108 639.0
Capital Recovery											
Cumulative Cash Flow	0	-382 200	-460 200	-343 173.3	-215 877.2	-772 84.7	98 585.8	408 803.4	748 609.6	972 425.4	1 081 064.3
PV			-460 200	101 762.3	96 254.2	91 126.8	100 554.5	154 233.0	146 907.6	84 140.6	35 514.3
NPV			350 293.3								